Solid catalysts for methanol and ammonia synthesis investigated by in-situ neutron diffraction

vorgelegt von
Diplom-Ingenieur (FH)
Timur Kandemir,
Master of Science
aus Wiesbaden

Von der Fakultät II – Mathematik und Naturwissenschaften
der Technischen Universität Berlin
zur Erlangung des akademischen Grades
Doktor der Ingenieurwissenschaften
- Dr.-Ing. -

genehmigte Dissertation

Promotionsausschuss:
Vorsitzender: Prof. Dr. Reinhard Schomäcker
Berichter/Gutachter: Prof. Dr. Robert Schlögl
Berichter/Gutachter: Prof. Dr. Thorsten Ressler
Berichter/Gutachter: Prof. Dr. Thomas Risse

Tag der wissenschaftlichen Aussprache: 02.09.2013

Berlin 2013
D 83

Solid catalysts for methanol and ammonia synthesis investigated by in-situ neutron diffraction

Timur Kandemir

Berlin 2013

Solid catalysts for methanol and ammonia synthesis investigated by in-situ neutron diffraction

Timur Kandemir

Dissertation
at the Faculty of Chemistry
Technical University
Berlin

Submitted by
Timur Kandemir
born in Wiesbaden

Berlin, 21.06.2013

First referee: Prof. Dr. Robert Schlögl
Second referee: Prof. Dr. Thorsten Ressler
Third referee: Prof. Dr. Thomas Risse
Date of oral examination: 02.09.2013

Contents

Zusammenfassung **vii**

Abstract **x**

1 Introduction **1**

1.1 Methanol synthesis . . . 2
1.2 Ammonia synthesis . . . 4
1.3 The pressure and material gap . . . 6
1.4 Neutrons - a probe for catalysis . . . 6
1.5 Thesis aim . . . 7
1.6 Outline of the thesis . . . 7

2 Summary of results and future perspectives **11**

3 Methodology **15**

3.1 Neutron diffraction [1] . . . 15
  3.1.1 Neutron interaction with matter . . . 15
  3.1.2 Neutron scattering length and cross-section . . . 16
  3.1.3 Influence of deuterium and nitrogen on the structure factor . . . 17
  3.1.4 Thermal displacement and Debye-Waller-factor . . . 19
  3.1.5 Structural imperfections and scattered intensities . . . 20
3.2 Electron Microscopy . . . 20
  3.2.1 Electron-Matter-Interactions . . . 21
  3.2.2 Transmission Electron Microscopy . . . 21
  3.2.3 Energy dispersive X-ray analysis . . . 22
3.3 Effluent gas analytic . . . 22
  3.3.1 Mass Spectrometry . . . 22
  3.3.2 Gas Chromatography . . . 22
  3.3.3 Titration . . . 23

---

[1] The following paragraphs are adapted from [1] and [2]

4 Continuous flow cell for catalytic reactions in the neutron beam [2] 25
4.1 Introduction . . . 25
4.2 Apparatus design . . . 26
4.2.1 Flow cell and reactor body . . . 28
4.2.2 Gas supply . . . 29
4.2.3 Effluent gas analytics . . . 29
4.3 Application example: Methanol synthesis . . . 31
4.3.1 Catalyst activation in high-flux diffraction . . . 31
4.3.2 Working catalyst in high-resolution diffraction . . . 32
4.4 Results . . . 32
4.5 Discussion . . . 33

5 Ammonia synthesis - proof of principle [3] 37
5.1 Introduction . . . 37
5.2 Experimental . . . 38
5.3 Application example: Ammonia synthesis . . . 39
5.4 Results . . . 39
5.5 Conclusions . . . 41

6 Microstructural and defect analysis of functional catalysts by diffraction and electron microscopy 43
6.1 Introduction . . . 43
6.2 Materials and Methods . . . 45
6.2.1 Sample preparation . . . 46
6.2.2 Neutron Diffraction . . . 46
6.2.3 X-ray Diffraction (XRD) . . . 47
6.2.4 Diffraction data analysis . . . 47
6.2.5 Transmission electron microscopy . . . 49
6.3 Results and Discussion . . . 49
6.3.1 Transmission electron microscopy . . . 49
6.3.2 Phase identification and Rietveld refinement of the neutron diffraction data . . . 52
6.3.3 Pattern decomposition methods . . . 56
6.3.4 Anisotropy due to defects . . . 62
6.3.5 Whole Powder Pattern Modelling (WPPM) including structural imperfections . . . 66
6.4 Conclusion . . . 71

7 The in-situ structure of a methanol synthesis catalyst [4] 73

---

[2] Adapted from [3]
[3] Adapted from [4]
[4] Adapted from [5]

8 Structure and phase composition of an operational ammonia catalyst 83

A Mathematical appendix for data evaluation 93
A.1 Analytical determination of instrumental broadening (IRF) 93
A.2 Deconvolution of instrumental contribution [5] 94
A.3 Fourier coefficients and Fourier-synthesis 97

B Used program codes 99
B.1 Instrument resolution determination by Origin 99
B.2 Stacking fault simulation using DIFFAX 100
B.3 Fourier-synthesis using PM2K 101

C Reactor construction 103
C.1 Fatigue crack analysis and materials database 103
C.2 Construction drafts for ammonia reactor 104

D Supplementary information to Chapter 8 109
D.1 Further experimental details 109
D.2 Line profile analysis by Williamson-Hall method 111

Bibliography 138

Acknowledgement 138

List of publications 139

List of conference talks as presenter or co-author 142

List of posters as presenter 144

---

[5] The following paragraphs are adapted from [6] and [7]

Zusammenfassung

Sowohl die katalytische Methanol- als auch Ammoniaksynthese spielen in der chemischen Industrie eine große Rolle. Beide Chemikalien werden als Plattformmolekül in Größenordnungen von mehreren Millionen Tonnen jährlich hergestellt. Beide Moleküle werden zurzeit aufgrund ihres vorteilhaften C zu H Verhältnisses sowie einfachen Handhabbarkeit im flüssigen Zustand als alternative Wasserstoffträger diskutiert. Die heterogen katalysierten Synthesen von Methanol und Ammoniak werden als struktursensitiv bezeichnet, da sie nicht auf jeder Form elementaren Kupfers oder Eisens ablaufen, sondern nur auf mikrostrukturell komplexen, Cu- und Fe-basierten Katalysatoren mit hohen Reaktionsraten.

In der Vergangenheit wurden große Anstrengungen unternommen, um Erkenntnisse über aktive Zentren und Reaktionsmechanismen beider Reaktionen zu gewinnen, welche eine erkenntnisbasierte Katalysatoroptimerung ermöglichen sollte. Dabei wurde postuliert, dass Erkenntnisse bzgl. des Zustandes des aktivierten Katalysators unter Umgebungsbedingungen nicht direkt auf Reaktionsbedingungen unter hohen Betriebstemperaturen und mehreren Atmosphären Gasdruck extrapoliert werden können. Bezugnehmend auf das fundamentale Interesse, katalytische Systeme unter nah-industriellen Synthesebedingungen in-situ zu untersuchen, wurde eine Durchflusszelle entwickelt, welche geeignet ist, unter 60-80 bar und 250-425°C Methanol sowie Ammoniak herzustellen und dabei Neutronendiffraktion und online-Gasanalytik durchzuführen. Basierend auf der Erkenntnis, dass die Aktivität eines Cu-basierten Methanolkatalysators mit der Defektivität der Cu-Nanopartikel korreliert [8, 9], wurde eine ex-situ Neutronendiffraktionsstudie an Referenzkupfer sowie nanokristallinen Katalysatoren mit zunehmender chemischer und struktureller Komplexität durchgeführt. Zur sorgfältigen Analyse der Streulinienprofile wurde ein Strukturanpassungsmodell verwendet [10], welches Linienversetzungen, planare Defekte, Domänengrößen, Kristallmorphologie sowie Modalität einschließt und so die Zuordnung der gemessenen Streuintensitäten zu einem speziellen mikrostrukturellen Ursprung ermöglicht. Die Übertragung der Erkenntnisse über die Mikrostruktur aus ex-situ Studien auf in-situ Studien zeigt die Stabilität der planaren Defekte im Cu/ZnO/Al_2O_3 Methanolkatalysator. Durch diese Ergebnisse, könnte eine Weiterentwicklung des angewandten "Whole-Powder-Pattern" Modellierungsalgorithmus unter Einbindung der thermischen Auslenkung der Atome sowie Vielfachstreuung –verursacht durch die reaktive Gasatmosphäre– eine noch präzisere Strukturauklärung des Katalysators unter Reaktionsbedingungen ermöglichen.

Die Rietveld-Verfeinerungen der in-situ Diffraktogramme des mehrfach-promotierten α-Fe-basierten Ammoniakkatalysators unter 75 bar und 425°C offenbaren die Anwesenheit von Verspannungen im Katalysator über die gesamte Synthesedauer hindurch. Dieses Ergebnis spricht für die Katalysatorpromotierung und -aktivierung als Ursache der Gitterverzerrungen im Kristallgitter des Fe (evtl. durch den Einbau von Fremdatomen).
Diese Beobachtungen zeigen, dass die mikrostrukturellen Eigenheiten der untersuchten Katalysatoren, die aus der komplexen und hoch-optimierten Präparationsgeschichte herrühren und für die Aktivität maßgeblich sind, unter harschen Reaktionsbedingungen erhalten bleiben.
Die Ergebnisse dieser Arbeit demonstrieren die Leistungsfähigkeit der in-situ Neutronendiffraktion und geben neue Impulse für die Untersuchung der Mikrostruktur arbeitender Katalysatoren unter anspruchsvollen Synthesebedingungen durch die Verknüpfung von Strukutur- und Aktivitätsinformationen.

Abstract

The two catalytic methanol- and ammonia synthesis reactions play a major role in chemical industry, both chemicals are produced as platform molecules in millions of metric tons. Both molecules are recently discussed as an alternative hydrogen carrier due to their advantageous C or N to H ratio and feasible handling in their liquid state. Both heterogeneous catalytic processes of methanol and ammonia synthesis are thought to be structure-sensitive reactions, as they don't proceed on every form of elemental Cu or Fe. High rates require special complex Cu and Fe-based catalysts.

A large effort was made to distinguish active centres and reaction mechanisms on the used catalyst with the goal of a knowledge-based catalyst optimisation for more efficient synthesis. It has been postulated, that the perceptions of the activated catalyst structure under ambient conditions can't simply be extrapolated to operation conditions at elevated temperatures and pressures. To study the catalytic systems in-situ under near-industrial working conditions, continuous flow cells were constructed, suitable for temperatures from 250 °C to 425 °C and 60 bar to 80 bar pressure which allow the collection of neutron diffraction data and simultaneous on-line gas analysis during catalytic synthesis of methanol and ammonia at industrial conditions.

Based on the key finding that the activity of the Cu-based methanol catalyst scales with a certain defectiveness of the nanoparticles [8, 9], an ex-situ neutron diffraction study on macrocrystalline Cu-powder and nanocrystalline catalyst with increasing chemical and structural complexity was conducted. By careful analysis of the diffraction line profiles a structural fit-model was elaborated, which takes line dislocations, planar defects and domains sizes, crystallite morphology and modality into account, enabling to assign the diffracted intensities in the patterns to a particular microstructural feature of the sample. Projecting the knowledge of the peculiar microstructure from ex-situ studies to in-situ studies under 250 °C and 60 bar reveals the stability of the planar defects in the Cu/ZnO/Al_2O_3 methanol catalyst. Based on this encouraging proof-of-principle results, further development of the applied convolutional whole-powder-pattern modelling algorithm [10] might allow a more precise structure simulation of operational catalysts in the future, taking thermal displacement of the atoms and multiple or incoherent scattering from the reactive gas phase into account.

Rietveld-refinement of the in-situ diffraction data at 425 °C and 75 bar of the operational multiple-promoted α-Fe based ammonia catalyst reveal the presence of strain in varying amounts over entire timer on stream, which is indicating that the proposed lattice distor-

tion has formed already as a result of catalyst activation, probably with other atoms in the interstitials of the iron lattice.
These findings confirm that the microstructural features of the used catalysts, which are a result of their complex and highly optimized preparation history and are claimed to be relevant for their activity, prevail under harsh near-industrial reaction conditions. The results presented in this thesis demonstrate the capability of in-situ neutron diffraction and give new impulses for the investigation of the microstructure of operational catalysts under demanding reaction conditions by linking structure and performance data.

Chapter 1

Introduction

Catalytic processes are most important in the modern chemical industry. Almost all chemical products (or their precursors) undergo catalytic reactions during their genesis. In contrast to the manifold of chemicals offered by chemical industry to the customer, methanol and ammonia are “basic” chemicals. With annual world production rates (2011) of more than 50 million metric tons methanol [11] and 136 million metric tons ammonia [12] these chemicals are the starting point for the synthesis of a large variety of polymers, speciality chemicals and fertilizers. From all catalytic reactions, the ammonia and methanol synthesis stated to be the prototype reactions of inorganic (ammonia) and organic (methanol) chemistry. Despite the difference in their (in)organic nature, both substances have some aspects in common. They are produced from syngas: either mixtures of CO_x and hydrogen or nitrogen and hydrogen. The reactants CO_x and H_2 can be derived from steam reforming of methane [13]. The steam-reforming route to ammonia is performed with a secondary reformer which introduces N_2 to the process gas [14]. Also, both catalytic reactions work best on a special form of catalyst, their rates are known to depend strongly on particle size, specific crystallographic orientation of the exposed catalyst surface or other (micro-)structural features, therefore they are classified as “structure-sensitive” reactions [15, 14]. Since the development of the fused iron-oxide catalyst, doped with K_2O as electronic promoter and CaO, Al_2O_3 and SiO_2 as structural promoters, for ammonia-synthesis by A. Mittasch in 1911, the reaction is successfully performed in the Haber-Bosch-process at BASF since 1913 for a century. The parallel development of high-pressure equipment and high performance alloys allow the application of harsh reaction conditions of 500 °C and 200 bar. In 1923, the chemist M. Pier developed the methanol production at BASF over a ZnO/Cr_2O_3 catalyst. Profiting from the experience in high-pressure operation made during the development of the ammonia-synthesis, reaction conditions of 400 °C and 300 bar could be applied in the so called BASF-process for methanol-synthesis. As the original BASF ammonia-catalyst with additional promoters is still in use today [16], with the availability of sulfur-free syngas, ICI presented the so-called low-pressure methanol (LPM)-synthesis catalyst, based on Cu/ZnO in the late 1960’s [17, 18], which is currently applied as state-of-the-art system in industrial synthesis.

Beside the industrial application as platform molecule for further synthesis and value chains, methanol and ammonia were brought back again to the focal point of research interest in the context of independence from fossil fuels and new, more sustainable energy-carriers [19]. One aspect is the ability to store "green" hydrogen (derived by water splitting from excess energy of regenerative sources) in a transportable form, or the use of anthropogenic carbon sources for methanol synthesis. Both molecules, methanol and ammonia, contain in their liquid form more hydrogen than liquid hydrogen for a given volume. The liquid state of both molecules make them very attractive to store and distribute them via present infrastructure e.g. pipelines, tankers and gas stations. Methanol could be directly used as a combustions fuel, or hydrogen could be released by steam reforming; in an endothermic reaction ammonia molecules can be decomposed by shifting the formation reaction back to its elements. Both molecules could also be used in fuel cells, either in a direct methanol fuel cell or in a combination of an ammonia reformer and an alkaline fuel cell to generate electricity [20].

1.1 Methanol synthesis

In the modern industrial LPM process, methanol is produced from synthesis gas (H_2, CO and CO_2) in the presence of ternary Cu/ZnO/Al_2O_3 catalytic systems, temperatures of 250 - 350°C and pressures up to 100 bar. Methanol synthesis from synthesis gas is exothermic ($\Delta H_R^{523\ K} = -122.8 kJmol^{-1}$) accompanied by decreasing entropy and therefore favoured to proceed at low reaction temperatures and high reaction pressures. The methanol synthesis is a proceeds according to the following reactions [21]:

$$CO + 2H_2 \rightleftharpoons CH_3OH \qquad \Delta H_R^{523\ K} = -61.4 kJmol^{-1} \tag{1.1}$$

$$CO_2 + 3H_2 \rightleftharpoons CH_3OH + H_2O \qquad \Delta H_R^{523\ K} = -20.9 kJmol^{-1} \tag{1.2}$$

$$CO + H_2O \rightleftharpoons CO_2 + H_2 \qquad \Delta H_R^{523\ K} = -40.5 kJmol^{-1} \tag{1.3}$$

The exact mechanism of industrial methanol synthesis is still under debate today [22]. Industrially applied ternary Cu/ZnO/Al_2O_3 catalysts for methanol synthesis consist of Cu nanoparticles dispersed by refractory metal oxides. It is accepted that mainly Cu works as the methanol synthesis catalyst in CO_2 hydrogenation [23, 24] wherein the catalytic activity is governed by the gas-accessible Cu surface area, so most active catalysts possess a large surface area [8]. In contrast to pure Cu, the activity of so called "methanol-copper" increases significantly for ZnO supported catalyst systems [9]. Because ZnO's own activity is nearly negligible, it has been suggested that there is a synergy between copper and zinc oxide [25]. One aspect for the performance of the operational catalyst was found to be the peculiar microstructure of the catalyst [8, 22, 9]. The catalyst preparation route, which affects and determines the microstructure of the final catalyst, was described as "chemical memory" by Ressler and Kurr [26, 27]. This chemical memory is expressed in particular in the Cu:Zn ratio, which is liable for a ligand field effect in the co-precipitated zincian malachite phase as the precursor state of the final catalyst. By gradual substitution of the

Cu^{+2} by the Zn^{+2} ion the Jahn-Teller distortion of the MO_6 octahedra in the malachite crystal structure is lowered due to different coordination requirements [22, 28]. In addition to that, a maximal incorporation of Zn into the zincian malachite precursor phase must be favoured by setting the ideal Cu:Zn ratio to 70:30. This highly Zn-substituted form of zincian malachite was identified as the relevant precursor phase playing the crucial role for the preparation of higher Cu-surface areas in the reduced catalyst [29, 22, 28, 30]. The role of ZnO and its observed synergies in the Cu/ZnO system have been broadly discussed in literature and are still not fully understood. Beyond the role of acting as a structural promoter by preventing the catalyst from sintering [31] or sulfur poisoning [32], it is as well discussed to act as a reaction promoter by providing a reservoir of atomic hydrogen and promoting hydrogen spillover [33] or affecting the active sites by strong-metal-support interactions (SMSI) [34]. Conclusively, these SMSIs are described for idealized model systems as support-induced strain by large differences in lattice constants [35] giving rise to a modified electronic structure [36, 37, 38, 26], changes in the particle shape due to wetting/nonwetting phenomena induced by changes of the reduction potential of the gas phase [39, 40] or brass/alloy-formation due to Zn^0-species diffusional transport onto the Cu-surface [41] and subsequent diffusion into the Cu-bulk [42]. Taking all proposed interactions for various model systems into account, ambient pressure x-ray photoemission spectroscopy bridged for the first time the so called "pressure and material gaps" (see detailed definition in the section below) by revealing a partial coverage of the surface of the reduced Cu nanoparticles with with ZnO_x in the high performance methanol catalyst [9]. The importance of these in-situ formed bimetallic stepped surface sites as possible active centres for methanol synthesis by means of increasing the adsorption strength for several intermediates (HCO, H_2CO and H_3CO) was supported by DFT calculations [9].

Although the beneficial role of Al_2O_3 in the industrial catalyst system as structural promoter was demonstrated, $Cu/ZnO/Al_2O_3$-catalysts are susceptible to irreversible deactivation by slow sintering and the resulting annealing of the defective Cu-structure [43] or poisoning due to sulfur or chlorine species in the feed gas [32] during the operational period.

Sintering is certainly affected by the environment e.g. the support-interaction, the particle size, the gaseous atmosphere and the temperature [44]. The sintering mechanism, where larger particles with lower surface energies will grow at the expense of smaller particles with higher surface energy [45] can be accelerated by an oxidising atmosphere [46] and increasing reaction temperature (e.g. hot-spots in the catalyst bed). The *Hüttig* temperature, which is estimated at one third of the melting point [31], defines the temperature, where atoms at defects on the shell of the particle start to become mobile. By reaching the *Tammann* temperature, approximately at the half of the melting point, also atoms from the bulk become mobile [31]. It is noted that the melting point of Cu ($T_m = 1358\ K$ [47]) is decreased by the nanocrystalline nature of the catalytically active particles. The *Hüttig* temperature of Cu, which is not far from operation temperature of methanol synthesis in commercial plants (e.g. between 480-580 K), induces atomic transport by a hopping mechanism or surface diffusion [48]. The driving force of the sintering process is the reduction of the total surface energy of the system which is associated with a reduction of surface

area including the annealing of defects that might be present at the particle surface. A stable shape of a particle is obtained, when the total free surface energy is minimized. This so called “unique equilibrium shape” for a faceted particle [37] can be described by the so called “Wulff construction”.
Several previous studies revealed a correlation between the intrinsic activity of the ternary Cu-catalysts and the deviation from the ideal Wulff shape of the Cu crystallites. These imperfections can be detected as different amounts of edge- and screw dislocations as well as planar defects like stacking faults and twin boundaries [49, 8, 50].

1.2 Ammonia synthesis

Due to the exothermic behaviour of the ammonia-synthesis, the volume fraction of ammonia is decreasing with increasing reaction temperature; but to achieve a reasonable reaction rate the reaction has to run at elevated temperatures. According to Le Chatelier's principle, the reaction is pushed towards the products by increasing the reaction pressure. Therefore, the modern Haber-Bosch process runs at temperatures around 300-500°C and pressures of 150-250 bar in the presence of α-Fe/Fe_3O_4/K_2O/CaO/Al_2O_3/SiO_2 according to the reaction

$$N_2 + 3H_2 \rightleftharpoons 2NH_3 \qquad \Delta H_R^{298\ K} = -92.22 KJmol^{-1}. \tag{1.4}$$

A detailed description of the mechanism of ammonia synthesis on iron surfaces was elaborated by Ertl [51, 52], who also stated the high structure sensitivity of the reaction [53, 54, 55]. In the industrial catalyst, the catalyst precursor consists mainly of Fe_3O_4 which has to be converted into the active form. The highly complex and orientated α-Fe, which was found to be crucial for the activity [56] can be generated from the precursor by reduction in feed gas, carefully carried out according to a strictly defined procedure [57]. The disordered structure of the ”ammonia-iron” includes evolution of metastable α-Fe platelets in (111)-orientation by topotactic reduction of magnetite precursor, as well as strained areas in predominant (100)-orientated areas [58]. Ertl reported, that the dissociative chemisorption of di-nitrogen on the iron surface is the rate limiting step in ammonia synthesis [54] and opens possibilities for sub-surface diffusion of the atomic nitrogen [55] including the formation of a surface nitride of the approximate composition Fe_2N and the presence of in-situ formed thermodynamically instable γ'-Fe_4N [59]. In analogy to the nitriding of steels by ammonia, it is proposed that high partial pressures (and therefore chemical potentials) of ammonia in the gas atmosphere allow the existence of (metastable) stoichometric γ- and ϵ-FeN and as well subnitrides of the type $Fe_{10-20}N$ [56, 57]. Despite the controversial discussion in literature, the actual structure of a technical ammonia-catalyst under industrially relevant ammonia yields remains currently unsolved due to the lack of experimental methods under these demanding conditions.

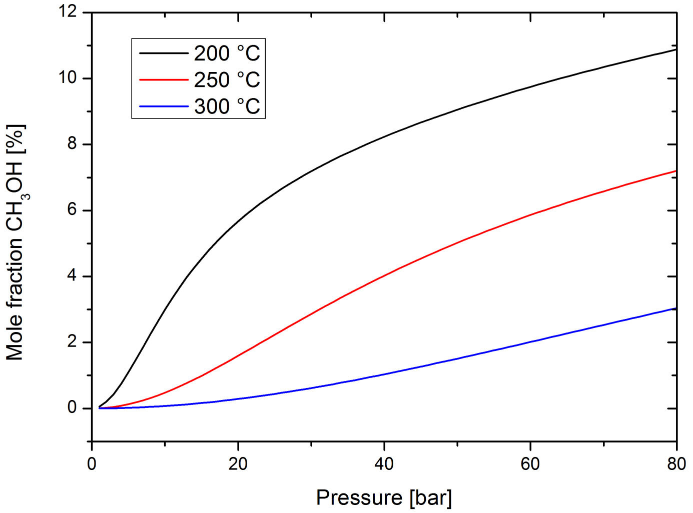

Figure 1.1: Thermodynamic equilibrium yield calculation for different temperatures as function of pressure for methanol synthesis from syngas containing 8 vol.% CO_2, 6 vol.% CO and H_2 in balance.

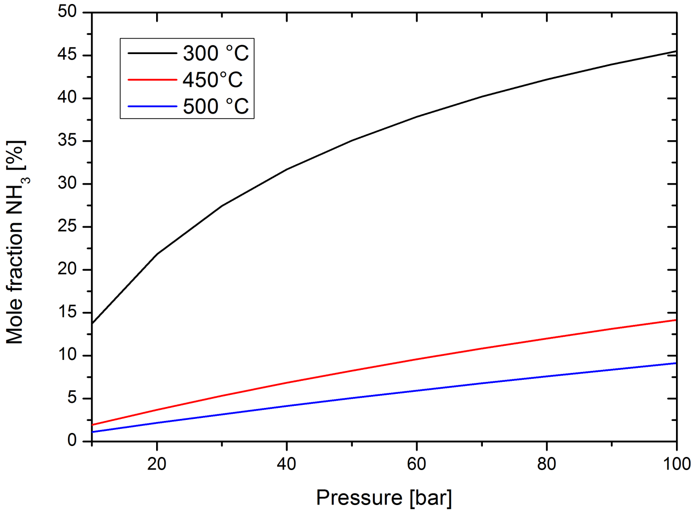

Figure 1.2: Thermodynamic equilibrium yield calculation for different temperatures as function of pressure for ammonia synthesis from a syngas composition of 1:3 N_2 to H_2.

1.3 The pressure and material gap

Although technically the synthesis of methanol and ammonia is already known for a long time, the catalysts have been studied extensively by many academic and industrial groups in a fundamental and applied manner to elucidate the reaction mechanisms and surface chemistry of commercial and alternative catalysts since several decades. The equilibrium calculations presented in Figs. 1.1 and 1.2 reveal the large dependency of the product yield on the temperature and pressure applied during the synthesis. It is obvious from these calculations, that a key problem in extrapolating surface-science based mechanistic studies under vacuum or ambient conditions to industrial reaction conditions is the neglect of the high chemical potential of reactants and products, the so called “pressure gap”. Particularly in the case of ammonia synthesis, where the concept of the “virtual” pressure [60, 61], which is much higher than the corresponding hydrostatic pressure due to its higher chemical potential of nitrogen atoms compared to its constituting molecules N_2 and H_2, expresses the high capability of the nitrogen in the ammonia to react with the catalyst. The absence of restructuring and texturing effects in e.g. single-crystal experiments under low-pressure conditions compared to a industrial catalysts with a highly complex structure under demanding reaction conditions is expressed as “material gap”. To bridge these gaps, the concept of conventional flow reactor studies have to be combined with suitable structural analysis methods, to clarify the nature of catalyst under working conditions. Early examples of in-situ testing by combining structural and chemical probes were reported on the Cu/ZnO-System by J. D. Grunwaldt et al. [41, 62] and on α-Fe system by B. Herzog et al. [56]. Both made great achievements regarding the proof of principle, to combine catalytic reactions and structural probes, but the materials gap was yet not closed, due to the reaction conditions which were still remote from industrial applied conditions and the investigated catalysts, which was not in all cases an industrial high-performance material. Further effort of bridging the gaps can give answers to the question, which active sites or phases are responsible for the synthesis. Therefore in-situ studies can be regarded as essential for the comprehensive understanding of a catalytic system.

1.4 Neutrons - a probe for catalysis

Neutron scattering techniques are powerful tools for detailed characterisation of materials of high degrees of dispersity and structural complexity. Specific advantages of neutrons result from their intrinsic property to interact with an atoms nucleus, enabling them to penetrate matter deeply, which makes them a bulk sensitive probe. Therefore complex geometries of sample environment or thick walls of metallic reactors can be easily penetrated. The strength of the interaction of the neutron with the atom depends on the relative orientation of the spin of the neutron and nucleus (cf. chapter 3) which is in particular useful to discriminate between nuclides or neighbouring atoms of similar electron configuration. Due to its magnetic moment it can be used in polarized form to investigate magnetic fields

[63]. By measuring its kinetic energy loss in inelastic scattering processes it can be used to investigate atomic motion (quasi-elastic scattering), molecular motion on surfaces as well as magnetic and crystal field excitations (inelastic scattering)[64]. The application of elastic scattering, particularly diffraction, to determine atomic and/or magnetic structure of a material can give answers to questions in solid catalyst research.

The first attempt to develop experimental equipment to study catalysts under demanding reaction conditions using neutron scattering techniques was made by J. Turner [65] and R. I. Walton et al. [66], by applying temperatures in the range of 4-1273 K and pressures from 10^{-6} mbar to 5 bar. The probably most prominent example of applying neutron scattering techniques to a catalytic research question was given by research groups of Albers, Lennon and Parker who applied inelastic neutron scattering to reveal catalyst deactivation and poisoning by active site blocking [67, 68, 69, 70, 71]. Although the great potential of neutron scattering was demonstrated by that work, so far the application of neutron diffraction to catalysis under industrial reaction conditions in in-situ studies is a novelty.

1.5 Thesis aim

The work presented in this thesis is focussed on the application of neutron diffraction to two prototype reactions in heterogeneous catalysis, namely methanol synthesis on ternary $Cu/ZnO/Al_2O_3$ as organic, and ammonia-synthesis on Fe-catalysts as inorganic reaction. By applying industrially relevant reaction conditions to the investigated catalytic system (i.e. 250 °C and 6 MPa for methanol-synthesis and 425 °C and 7.5 MPa for ammonia-synthesis) significant amounts of products, given by the thermodynamic equilibrium, can be achieved. The parallel acquisition of structure and activity parameters allows conclusions to be drawn regarding the effect of the catalyst bulk structure on the performance. A comparison of the observed in-situ structure with suitable reference systems of increasing chemical and structural complexity allows a direct comparison of the present structure with proposed formation and/or (re)-arrangement of reaction-enhancing active phases. The increased general understanding of the structure-activity relationship shall help to improve the knowledge-based development of more efficient and sustainable catalysts of the next generation.

1.6 Outline of the thesis

The thesis is divided into eight chapters, each dealing with one experimental aspect addressed along the study. In the beginning a short introduction to the topic of heterogeneous catalysis and methodology is given. Later, obtained results are summarized and discussed in the context of literature.

Chapter 2 summarizes the work presented in this thesis and links the experimental findings presented in chapters 4 to 8. Final conclusions are drawn and an outlook is given regarding further research in the field.

Chapter 3 briefly summarizes the physical background of neutron diffraction and the basics of the experimental methods applied in this study.

Chapter 4 adapts a paper describing the construction and successful application of a continuous flow cell for catalyst characterization on neutron diffractometers. The proof of principle is shown for the reduction of a ternary $Cu/ZnO/Al_2O_3$-catalyst. Also methanol synthesis was carried out at 250 °C and 6 MPa for 24 hours. Conceptual contributions to the development of the cell were made by Dirk Wallacher, Raoul Naumann d'Alnoncourt, Malte Behrens and Robert Schlögl. Technical support during the testing of the cell was provided by Thomas Hansen, Klaus-Dieter Liss, Michael Tovar, Alain Daramsy, Scott Olsen, Eugen Stotz, Edward Kunkes and Gregor Wowsnick. Rietveld refinement was carried out by Frank Girgsdies.

Chapter 5 adapts a paper describing the successful application of the flow cell for ammonia synthesis at 330 °C and 6 MPa. Rietveld-refinement presented in this chapter was carried out by Frank Girgsdies. TEM analysis was done by Igor Kasatkin. Technical support during the testing was supplied by Malte Behrens, Edward Kunkes, Klaus-Dieter Liss, Vanessa K. Peterson, Scott Olsen, Friedl Bartsch and Mai Anh Burke. Conceptual contributions were made by Malte Behrens, Robert Schlögl, Friedrich Karl Seitz and Frank Rosowski.

Chapter 6 is a manuscript describing the routines to analyse microstructural and defect parameters from scattered intensities. Values determined by TEM studies (Igor Kasatkin) and Rietveld-refinement (Frank Girgsdies) are compared to classical linear approaches (Williamson-Hall-plot, Scherrer-formula). Areal defects affecting the scattered intensities, depicted by a deconvolution algorithm developed in MathCAD (written by Igor Kasatkin), are compared to simulations of defective structures. The results of linear-combinating Rietveld-refinement are compared to the results of a convolutional fitting routine (developed by Matteo Leoni). The samples investigated in this study were kindly provided by Stefanie Kühl, and measured by Malte Behrens, Stefanie Kühl and Michael Tovar.

Chapter 7 adapts a paper describing the structure of a ternary methanol synthesis catalyst and shows neutron powder diffraction pattern of this catalyst under 250 °C and 6 MPa. Material properties like linear thermal expansion and alloying are discussed. Rietveld-refinement presented in this chapter was carried out by Frank Girgsdies. TEM analysis was done by Igor Kasatkin. Technical support during the testing was supplied by Thomas Hansen, Klaus-Diter Liss, Edward Kunkes and Gregor Wowsnick. Nikolas Jacobsen expressed his consent to publish the experimental results. Conceptual contributions were made by Malte Behrens and Robert Schlögl.

Chapter 8 is a manuscript describing the structure and phase composition of a Fe-based ammonia catalyst under near-industrial ammonia-yield. The persistency of the complex microstructure of the major α-Fe phase under synthesis conditions of 425 °C and 7.5 MPa syngas is reported and analysed. TEM analysis was carried out by Manfred E. Schuster. Technical support during the measurement was made by Anatoliy Senyshyn. Conceptual contributions were made by Malte Behrens and Robert Schlögl.

Chapter 2

Summary of results and future perspectives

The aim of this thesis was to investigate heterogeneous catalysts under reaction conditions with neutron diffraction as a bulk sensitive technique. The objective of this experimental approach was to contribute to a general understanding of a.) the structure of a commercial, operational Cu-based catalyst for methanol synthesis and b.) the verification of proposed bulk-nitriding of industrially applied Fe-based catalysts for ammonia synthesis.

The pivotal technical challenge was the construction of an appropriate flow cell, suitable to run catalytic reactions under pressures up to 80 bar and 475 °C and able to act as an in-situ cell for diffraction experiments at the same time. Under these reaction conditions, the achievable amount of reaction products –in the order of magnitude of industrial processes– provides a promising basis for the evaluation of structure and activity correlations. For the first time it was possible to apply industrial conditions regarding T and p corresponding to product yields of ∼6 vol.% methanol and ∼13 vol.% ammonia in a neutron beam. Previous experiments, carried out under less demanding reaction conditions, state a direct relationship between the catalyst's structural properties and the chemical potential of the surrounding atmosphere. Thus, due to the use of industrial reaction conditions and industrial catalyst materials, this study presents an example of in-situ experimentation, which does not suffer the famous "pressure and material gaps" that often hinder progress in applied catalyst research.

Particular issues of the methanol synthesis catalyst are the dynamics of the Cu/ZnO-based composite that have been proposed to lead to formation of the active site exclusively under reaction conditions and the strong influence of the ZnO on the structure of the Cu-phase [72, 73, 41, 62, 40].

Concerning methanol synthesis, it can be concluded that the investigated ternary Cu/ZnO/Al_2O_3-catalyst exhibits a high microstructural complexity, which differs tremendously from the supposed structure of an ideal fcc-crystal in the following manner:

During the reduction of the CuO precursor in pure D_2, metallic Cu appears in the diffraction pattern. The full reduction of the crystalline fraction of CuO exhibits an onset at 402 K and the fast appearance of Cu at 413 K suggest the presence of a undetected, diffraction-amorphous intermediate, which may be a form of, in agreement with literature studies, Cu_2O [36]. The relatively broad diffraction peaks of the readily reduced $Cu/ZnO/Al_2O_3$-catalyst imply a.)the crystallinity of the Cu-phase and b.)the presence of the high microstructural complexity right from the beginning of the synthesis. After 24 h time on stream, no major changes of the Cu-phase are observed. Additionally, no significant variation of the Cu-lattice parameter was observed. The first attempt to describe microstructural imperfections or defectiveness of the catalyst in terms of elastic deformation due to "strain" or "defects" by the deviation of the d_{111}/d_{200} value from 1.1547 for the "ideal" fcc-lattice, demonstrated that the presence of stacking faults causes a shift of the 111 and 200 peaks towards each other. This observation is in good agreement with the phenomena described by Warren [74, 75, 76], reporting that with an increasing number of stacking faults, d_{111}/d_{200} will become smaller than 1.1547. Concerning this approach, the evolution of d_{111}/d_{200} from the end of the reduction procedure over 24 h time on stream revealed that the Cu-phase in the active catalyst bears –in contrast to the annealed Cu-reference powder ($d_{111}/d_{200} \succeq 1.155$)– a significant amount of stacking faults and maintains its defect structure.

The signature of these stacking faults and twin boundaries –first observed locally in the Cu-particles in TEM-studies by Kasatkin et al. [8]– in the diffraction pattern is expressed by the above mentioned peak shift and an asymmetric broadening and tailing of the peaks. Systematic crystallographic defect modelling studies, carried out on a series of samples ranging from pure Cu-reference powder to ternary real catalyst systems with increasing chemical and structural complexity, revealed a dependency between stacking fault concentration and anisotropic broadening of the Cu Bragg-peaks, while no correlation of the observed peak anisotropy with the crystallinity of the Zn-by-phase was observed. As an alternative to simple pattern decomposition methods, the experimental diffraction patterns were fitted by Fourier-synthesis, the so called "Whole-powder pattern modelling [10]", which is therefore a more sophisticated fitting routine than the classical Rietveld-algorithm [77] and comfirmed the defectiveness of the catalyst.

It is evident that defective nanoparticles in a diameter range ≤10-15 nm show elastic properties, which differ from macrocrystalline bulk material. The deviation from ideal fcc-Cu is manifested in a lattice contraction by 0.1% at room temperature. As a consequence, the linear thermal expansion coefficient for the $Cu/ZnO/Al_2O_3$-catalyst is observed to be with a value of $\alpha = 35.1 \cdot 10^{-6}$ K^{-1} twice as large as for reference Cu ($\alpha = 17.8 \cdot 10^{-6}$ K^{-1}). Under isothermal synthesis conditions the discrepancy in the lattice parameter is converging towards the reference Cu. Upon further heating, the onset temperature for α-brass formation was determined to be around 603 K, which is in good agreement with the increase of the diffusion coefficient of Zn in Cu at the corresponding temperature by five orders of magnitude from $2.7 \cdot 10^{-22}$ cm^{2}s^{-1} at synthesis conditions (523 K) to $3.2 \cdot 10^{-17}$ cm^{2}s^{-1} at 623 K, reported in the literature by Spencer [42]. Thus, the formation of bulk-brass under reaction conditions can be directly excluded. Regarding the interactions between ZnO and Cu, these findings support the concept of a static, defective Cu-phase which maintains its defect structure and interacts rather in a form of more mobile ZnO_x than mobile Cu e.g. by migration of ZnO_x entities onto the surface of the Cu nanoparticles

by strong-metal-support-interaction (SMSI). However, no evidence for Cu mobility or Cu-particle morphology changes, which were proposed by Grunwaldt et al. [41], preceding the reversible surface decoration of the Cu particles with ZnO_x, could be obtained.
Conclusively, the proved high concentration of stacking faults prevail in the industrial Cu/ZnO/ Al_2O_3-catalyst under reaction conditions, while neither a bulk inclusion of reactive species from the gas phase nor the proposed bulk α-brass or Cu-hydride formation was observed under synthesis conditions in the industrial high performance catalyst.

In analogy to the Cu-catalyst, the drastic microstructural deviation of the activated ammonia-catalyst from "isotropic"-iron is attributed to its strong hierarchical structuring previously revealed by SEM-studies [78, 58] and described in literature [57, 79].
Regarding the phase composition of the reduced ammonia-catalyst in the pre-reaction state at 330 °C, in addition to a metallic α-Fe bulk phase ($a_{28^\circ C} = 2.86158\text{Å} \pm 0.00016\text{Å}$, $a_{330^\circ C} = 2.87840\text{Å} \pm 0.00013\text{Å}$, $a_{425^\circ C} = 2.88434\text{Å} \pm 0.00033\text{Å}$) a faint contribution from a magnetite-type (Fe_3O_4) spinel-phase is detected. This phase could be most probably attributed to a non-stoichiometric and defective $(FeO)_x \cdot (\gamma\text{-}Al_2O_3)_y$, which is a consequence of the kinetic difficulty in fully reducing the catalyst. Further heating in syngas up to 425 °C leads to a "strongly reduced" catalyst, which is after 26 h on stream analytically free of Fe_3O_4 or rather $(FeO)_x \cdot (\gamma\text{-}Al_2O_3)_y$ in the diffraction-accessible bulk. By comparison of the in-situ patterns with increasing ND_3 yields up to 12.6 vol.% within a period of 88 h time on stream (TOS) with a commercial, stoichimetric $Fe_{2-4}N$ powder, no formation of a stoichiometric nitride phase in the catalyst's bulk was observed.
Despite the absence of major phase transitions, subtle changes in the complex microstructure of the working catalyst are present. These minor changes in the shape of the diffraction peaks indicate that the majority of the microstructural deviations of "ammonia-iron" derived at ambient pressure prevail under technically harsh operation conditions. The major α-Fe phase has a linear thermal expansion coefficient in the range of RT to 330 °C ($\alpha = 11.8 \cdot 10^{-6}\ K^{-1}$) which is in good agreement with the literature value [47]. With respect to the linearity of the linear thermal expansion coefficient up to 550 °C [80], the measured lattice constant of the catalyst under reaction conditions at 425 °C is 0.1% larger than expected for this temperature. The most probable explanation for the variation in d-spacing, which is consistent with the literature view on the active catalyst is the presence of endotactic chemical impurities [57], expressed in a fashion of incorporation of individual "molecules" of hercynite into the lattice of the α-Fe host lattice, a phenomenon named "paracrystallinity" by Hosemann et al. [81]. In this context it remains unclear, if the observed variation in the peak breadth over TOS is really a consequence of increasing apparent domain size (as determined by Rietveld-method) or either a contribution from non-statistically distributed, anisotropic strained diffraction planes in the domain resulting due to hercynite incorporation [57]. Therefore, these diffraction results encourage further post-reaction high resolution TEM (HRTEM) studies of the near surface region in the future. Conclusively it is claimed, that the interpretation of the above results is consistent with the literature view on the active catalyst [82, 56, 83, 78]; The presence of strain in varying amounts over the entire TOS is indicating that the proposed lattice distortion has

formed already as a result of catalyst activation, probably with other atoms in the interstitials of the iron lattice.

The results presented in this work demonstrate the capability of in-situ neutron diffraction in catalysis research. Currently there is no other method available, which gives answers regarding the bulk-structure of a catalyst, its inclusion of reactive species from the surrounding gas- or liquid phase or its restructuring behaviour under certain chemical potentials of the surrounding atmosphere under demanding reaction conditions. Combining structural information gathered from in-situ neutron diffraction with sample characteristics determined with routine lab equipment e.g. BET, TG or microscopy allows bridging the “materials- and pressure-gaps” towards a realistic model of the structure of catalyst under reaction conditions by applying sophisticated methods like whole powder pattern modelling. Future work using this methodology will address the correlation of the evaluated structural properties with catalytic performance and include information about the evolution of the microstructure with deactivation of the catalyst over longer operational periods. Further improvement of the applied whole-powder-pattern modelling algorithm might allow a more precise structure simulation of the operational catalyst by taking thermal displacement of the atoms and multiple or incoherent scattering from the reactive gas phase into account. Particularly the revival of Fischer-Tropsch-synthesis in the context of “clean fuels for the future” might benefit from in-situ neutron diffraction regarding the identification of cubic and hexagonal cobalt phases in the reduced and operational catalyst.

Chapter 3

Methodology

3.1 Neutron diffraction [1]

3.1.1 Neutron interaction with matter

Low-energy thermal neutrons are an important tool for the investigation of static and dynamical properties of condensed matter due to their intrinsic properties. Similar to X-rays their ability to interact with matter is described in a general manner by absorption, transmission and scattering. As neutrons can be generated in several different ways by radioisotope-sources, an effective process and sufficient flux of free neutrons can be achieved by spallation or fission. While all experiments carried out along this study were done using research reactors, for sake of conciseness all energies and properties given in further text will concentrate on fission-neutrons. In a constant wavelength-source (nuclear reactor) fast fission neutrons are produced in an energy range of 10 keV to 20 MeV. By the application of the de Broglie-relation,

$$\lambda = \frac{h}{\sqrt{2m_nE}} \tag{3.1}$$

(h= Planck constant, m_n = neutron's mass, E = neutron energy) this energy range correspondents to a wavelength of 0.28 to 0.0064 pm. While the core of a reactor is placed in a moderator (often water or heavy water) a fast fission neutron undergoes several elastic collisions with the surrounding water molecules, in which it looses kinetic energy and becomes "moderated". The energy distribution of the moderated neutrons in equilibrium with the moderator temperature is described by the well known Maxwell-Boltzmann distribution. The neutrons extracted from the moderator tank by neutron guides have a kinetic energy below 100 meV and a corresponding wavelength larger than 90 pm, which classifies them as thermal neutrons. As the neutron –in contrast to X-rays– interacts with the nucleus, the character, strength and probability of interaction is a direct function of its energy. Most values and constants stated in literature refer to thermal neutrons at norm conditions at

---

[1] The following paragraphs are adapted from [1] and [2]

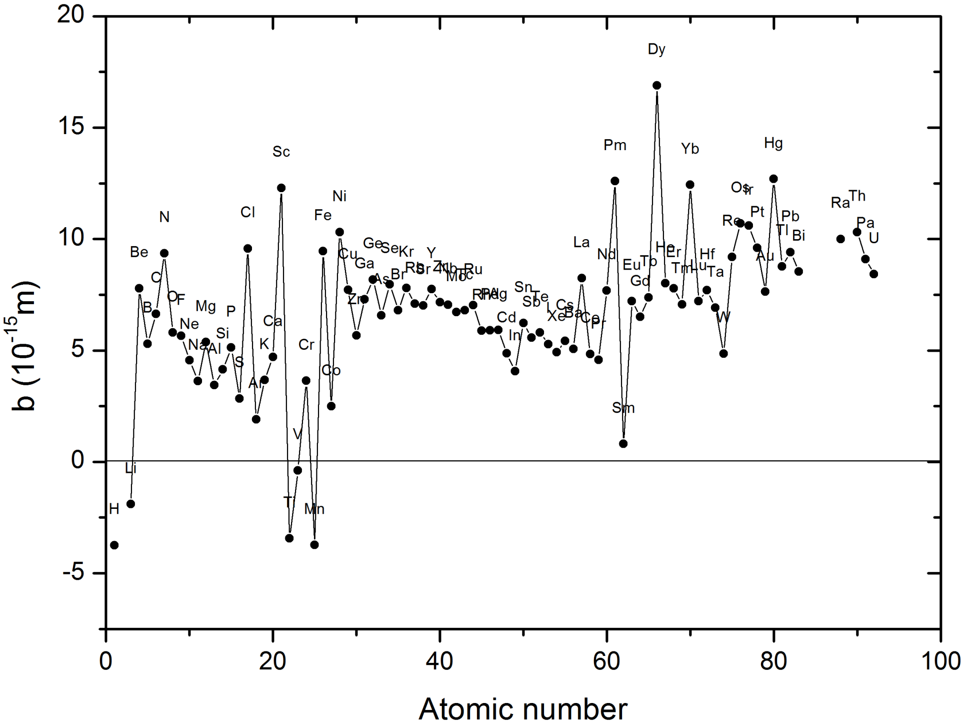

Figure 3.1: Scattering length b for thermal neutrons as function of the atomic number, numerical values taken from [84].

273.16 K which is equal to a kinetic energy of 35.31 meV and a corresponding wavelength of 152 pm.

3.1.2 Neutron scattering length and cross-section

While crystallographic information can be obtained from neutron and X-ray diffraction in a similar manner, a great advantage of neutron diffraction is the high selectivity for neighbouring elements, their isotopes and specific nuclides. Due to the X-ray interaction with the electron shell, the scattering probability of an atom is described by an atomic form factor F, which is monotonous increasing with atomic number. For the case of neutrons the scattering strength with individual nuclei is given by the basic quantity b, the scattering length. The values of the scattering lengths (Fig. 3.1) vary irregularly from one nucleus to another due to their strong dependence on the relative orientation between neutron spin and nuclear spin. Due to the statistical distribution of spin orientations and isotopes in a periodical lattice a fluctuation in the scattering potential is observed. These fluctuations, known as incoherent scattering, are isotropic (non-angle-dependent) and contribute to the background signal in acquired powder patterns. The scattering length of a neutron with spin $\vec{s}$ and a nucleus with spin $\mathbf{I}$ is given by

$$b = b_c + \frac{2b_i}{\sqrt{I(I+1)}}\vec{s}\cdot\mathbf{I} \tag{3.2}$$

wherein I is the nuclear-spin quantum-number, b_c the coherent and b_i the incoherent scattering length [85]. As the total scattering cross section is a linear combination of coherent and incoherent cross section according to

$$\sigma_t = \sigma_c + \sigma_i \tag{3.3}$$

with the related cross sections for

$$\sigma_c = 4\pi b_c^2 \tag{3.4}$$
$$\sigma_i = 4\pi b_i^2 \tag{3.5}$$

Eq. 3.3 can be written as

$$\sigma_t = 4\pi\langle|b^2|\rangle. \tag{3.6}$$

The element-specific coherent and incoherent cross sections as well as the resulting total cross section for thermal neutrons (acc. to Eq. 3.3) as function of the atomic mass of target atom are depicted in Fig. 3.2. As it can be seen from Fig. 3.2, the total scattering cross section for H_2 with 82.02 b is very high. While X-rays are practically insensitive to hydrogen, a high content of hydrogen would cause in the case of neutron diffraction a huge incoherent background. Therefore, the in-situ studies were carried out with deuterated syngas to significantly reduce incoherent scattering from the gas atmosphere. As Cu and Zn are isoelectronic, one takes advantage of the discrimination of neighbouring elements in the case of alloy formation due to sintering or ageing, in particular for the ternary $Cu/ZnO/Al_2O_3$-catalyst. Due to the fact, that the scattering for nitrogen is as large as for iron, this property is greatly appreciated for the in-situ study of ammonia-synthesis, where the formation of Fe-N alloys or intercalation are expected.

3.1.3 Influence of deuterium and nitrogen on the structure factor

With respect to the proposed intercalation of nitrogen into the Fe-lattice, or the influence of nitride or hydride formation, the structure-factor is going to be discussed. The amplitude of a scattered intensity of a present phase is a function of the structure factor, which is described as a Fourier component of the electron density of the unit cell, convoluted by the thermal motion amplitudes of the atoms [86], which is given by

$$|F(Q)|^2 = \left|\sum_{j=1}^{N} b_j T_j exp\{i(QR_j)\}\right|^2 \tag{3.7}$$

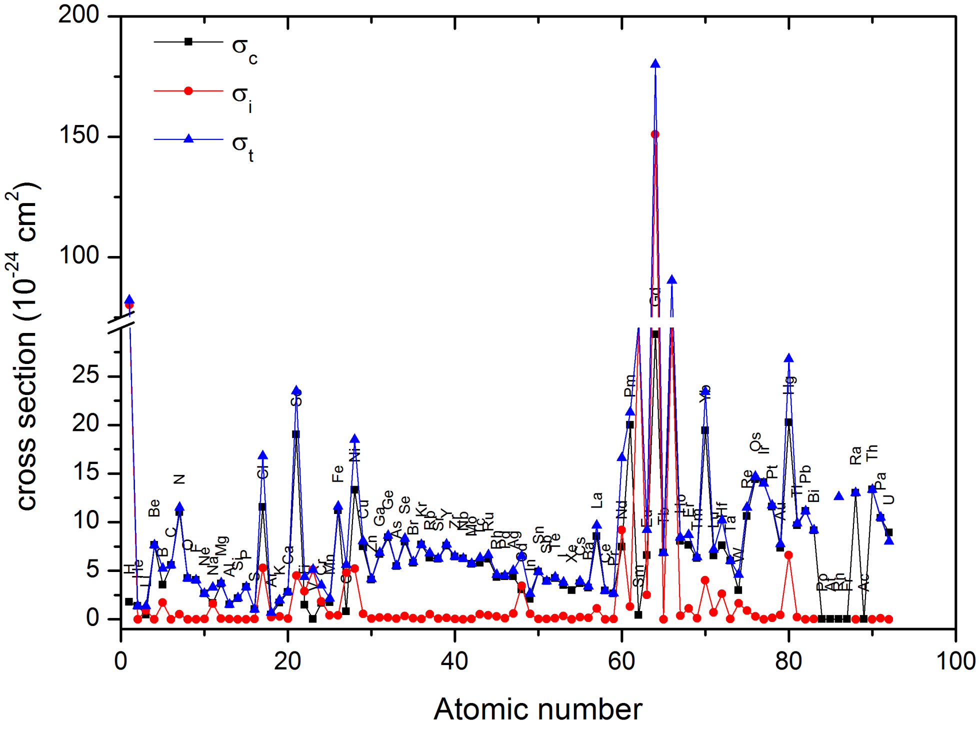

Figure 3.2: Coherent, incoherent and total scattering cross sections σ for thermal neutrons as function of the atomic number [84].

wherein R_j is the actual site occupancy divided by the site multiplicity. T_j is a measure for the thermal and random static displacement of the jth atom parallel to the diffraction vector Q. As follows from scattering theory, the scattering vector $\vec{Q}$ is the difference between incident $\vec{K_0}$ and scattered $\vec{K}$ beam, which results in a reciprocal unit. The simple relation between scattering angle and reciprocal diffraction vector is given trough the fulfilment of the Bragg-condition if the scattering vector Q is equal to a reciprocal lattice vector by

$$Q = \vec{K} - \vec{K_0} \tag{3.8}$$

$$Q = 2\pi M_j, \quad \text{with} \quad \mathrm{M_j} = \left(\begin{smallmatrix} h \\ k \\ l \end{smallmatrix}\right) \tag{3.9}$$

$$|Q| = 4\pi(sin\theta)/\lambda \ . \tag{3.10}$$

The structure factor then transforms into:

$$\left|F_{(hkl)}\right|^2 = \left|\sum_{j=1}^{N} b_j T_j exp\{2\pi i(hx_j + ky_j + lz_j)\}\right|^2 \tag{3.11}$$

where h, k and l are the Miller indices; x_j, y_j and z_j are the position parameters of the jth atom in the unit cell [87].

3.1.4 Thermal displacement and Debye-Waller-factor

As it was already discussed above, the structure factor is convoluted with the thermal motion amplitude of the atoms in a unit cell. As the neutron interacts with the nucleus of an atom, a significant displacement occurs during the diffraction experiments even at room temperature. The so called Debye-Waller factor describes the variation of the scattered intensity due to thermally induced lattice vibrations, depicted by

$$T_j = exp\{-W_j\} \tag{3.12}$$

where $W_j$is the product of row matrices with elements (hkl) and symmetrical matrices representing the anisotropic temperature parameters of an atom j on a certain position. Assuming the same Debye-Waller-factors for all atoms in an unit cell, the geometric structure factor becomes:

$$\left|F_{(hkl)}\right| = \left|\sum_{j=1}^{N} b_j exp(-W_j) exp\left[2\pi i(hx_j + ky_j + lz_j)\right]\right| \tag{3.13}$$

With an assumption of a harmonic vibration with an atomic displacement u_j the atomic Debye-Waller-factor follows as

$$T_j(Q) = exp\{-\frac{1}{2}\langle(Q\ u_j)^2\rangle\} \ . \tag{3.14}$$

By assuming an isotropic mean square thermal displacement with $\frac{1}{3}\langle u_j^2\rangle$ Eq.3.14 becomes:

$$T_j(Q) =\{-\frac{1}{6}Q^2\langle u_j^2\rangle\} \; . \tag{3.15}$$

Combining Eqs.3.12 and 3.14 gives

$$W_j =\frac{1}{6}Q^2\langle u_j^2\rangle \; . \tag{3.16}$$

The "atomic displacement parameter" which is used in the Rietveld-algorithm is therefore calculated by

$$B_{iso,j} =W_j\frac{\lambda}{sin^2\theta} = \frac{8\pi^2}{3}\langle u_j^2\rangle \; . \tag{3.17}$$

It is noted that the observed scattered intensity follows with respect to Eq.3.13

$$I_{(hkl)} \propto |F_{(hkl)}|^2 \; . \tag{3.18}$$

3.1.5 Structural imperfections and scattered intensities

Eqs. (3.10) implicates that diffraction phenomena can be used to investigate microstructural and defect analysis of a bulk sample. As the structural probing is carried out parallel to the diffraction vector $\vec{Q}$, it follows that the extension and dispersion of the reflecting planes perpendicular to the diffraction vector are probed. The dispersion of lattice planes perpendicular to the so called "column length" can be affected in multiple ways due to, e.g., residual strains, lattice imperfections by multi-order defects or crystal size and shape. Since the observed intensity in a powder pattern is a convolution of intrinsic effects of the sample and an instrumental contribution, the analysis of the micro-structure of a diffracting bulk sample volume is often not straightforward. A more detailed discussion about the methodologies of analysis of the observed intensity in a diffraction pattern and its physical origin is carried out in chapter 6.

3.2 Electron Microscopy

As a very useful complementary technique to neutron diffraction, electron microscopy can help to get a general understanding of local structuring, composition and morphology of a catalyst from microscopic to atomic scale. Each analysis carried out on an electron microscope is based on a certain scattering phenomenon. Electrons are charged particles and in analogy to neutrons, they are devoted to the particle-wave dualism, described by the de Broglie-relation (c.f. Eq. 3.1), while strong coulomb forces apply.

3.2.1 Electron-Matter-Interactions

Comparably to neutrons, electrons show different phenomena if they pass matter, but in contrast to neutrons, as they are charged particles, more secondary effects are observed. The most important interaction of electrons with matter is the coulomb interaction. Depending on the scattering geometry and transferred energy, backscattering and emission of secondary electrons and as well as Auger electrons, the emission of radiation in terms of characteristic X-rays, Bremsstrahlung and visible light can be the consequence of the interaction. If matter is entirely passed through, an attenuated direct beam as well as elastically and inelastically scattered electrons could be observed, while heat, electron-hole pairs and an amount of “adsorbed” electrons remain in the matter. As electron scattering is very crucial for the understanding of imaging with electrons, it has to be differentiated between backscattered electrons and secondary electrons which are of interest for Scanning Electron Microscopy (SEM) rather than for Transmission Electron Microscopy (TEM). As the abbreviation TEM states, the transmitted electrons are of particular interest, as they were directly attenuated by matter (direct beam) or underwent single or multiple scattering processes which were of elastic or inelastic nature.

3.2.2 Transmission Electron Microscopy

The basic principle of imaging with a TEM is based on the irradiation of a thin specimen with an coherent beam of electrons. For the sake of image quality, a homogeneous illumination of the area of interest with an electron beam of uniform energy density in an energy range of 30 keV-200 keV is a prerequisite. The amount of electrons transmitted through the specimen is a direct function of the differential scattering cross section –or more precisely– the mean free path (the resulting average distance that the electron travels between scattering events), the density and elemental composition of the specimen is a crucial factor for the right choice of incident electron energy, sample thickness and the desired resolution. As most of the investigated specimen are crystalline, the electron waves interfering in a periodic potential of a crystal lattice propagate as a wave-field with the same periodicity as the lattice. The achieved amplitude is known as ’diffraction contrast’ [88]. If the objective aperture below the specimen allows propagation of the direct beam and diffracted electrons with a scattering angle less than the acceptance angle of the aperture, whilst blocking the diffracted electrons with a scattering angle larger than the objective aperture, a bright field (bf) image is obtained, which contains information about crystalline domains, domain and phase boundaries, local imperfections as edge and screw dislocations as well as stacking faults and twin boundaries. In contrast to bf, in dark field (df) mode only diffracted electrons contribute to imaging. To achieve a df, the objective aperture is replaced from the optical axis, or, in terms of imaging conditions favorable, by tilting the illumination such that the diffracted beam runs along the optical axis (in this case, the objective aperture is left at the center). Tilting of the specimen allows to select a desired bragg condition of domains, which appear as bright areas on dark background. Df imaging is of particular interest for studying position and type of lattice imperfections as well as shape, size and distribution of coherently scattering domains of the crystalline specimen.

3.2.3 Energy dispersive X-ray analysis

A specimen irradiated with electrons causes the elements present to emit excess energy by dropping electrons from higher shells to electron holes in lower shells created by excited and ejected electrons as characteristic X-rays. These emitted x-rays can be collected by a semiconductor-detector e.g. Si(Li) placed placed between the upper and lower pole piece of the objective lens to make statements about the elemental composition of a sample. By setting different currents to the detector, background discrimination and signal amplification can be achieved. The energy resolution of the detector is given by the number and breadth of the counting channels. A typical acquisition range of EDX is 0-40 keV with a resolution (FWHM) of 130-150 eV, while the most Kα-emission lines (which are the strongest) are recorded in a range of 0-10 keV.

3.3 Effluent gas analytic

As one of the goals of this thesis is the link between the catalysts structure under reaction conditions and its performance, on-line effluent gas analytic was carried out to monitor gas phase composition and product quantity. For lab-performance studies a combination of mass spectrometry and gas chromatography was used during methanol synthesis; for ammonia synthesis a combination of mass spectrometry and titration was applied during diffraction experiments as well as laboratory studies.

3.3.1 Mass Spectrometry

For general on-line gas analysis, a quadrupole mass spectrometer (MS) is used in this study, to detect molecules and fragments by means of their mass to charge ratio m/z in continuous probing. As the number of incident ions is proportional to the concentration, the pressure has to be kept constant at any time, which could be achieved by e.g. pinholes and/or heated capillaries as inlet systems. The detected molecules show a certain degree of ionization and fragmentation which is characteristic and can be regarded as a 'fingerprint', references of this fragmentation patters are available in web resources eg. NIST chemistry WebBook [89]. As the degree of fragmentation is a strong function of the ionization source, the acceleration parameters have been kept constant along the study. For further information, the reader is referred to fundamental literature [90, 91].

3.3.2 Gas Chromatography

During methanol-synthesis a quantification of the products and unreacted educts in the effluent gas is mandatory for kinetic studies, mass balances and performance testing. For varying space velocities different side products can occur, gas chromatography (GC) is a valuable method to quantify them down to concentrations of ∼ 500 ppb [91]. The basic principle of GC is the separation of gas/liquid or liquid/liquid mixtures by the different boiling points or vapour pressures of the single components in the carrier gas He (mobile phase). By using very thin capillaries with a packing of different polarity (stationary phase) placed in a furnace, mobile and stationary phase can interact. Setting different flow rates of the carrier gas, allows components of a mixture to elute retarded. They can be distinguished by specific retention times, which can be detected by a thermal conductivity (TCD) and flame-ionization detector (FID). Because TCD is a non-destructive detector, it is operated in front of the FID. This combination allows the detection of H_2O, H_2, CO_2 and Ar at the TCD, while the FID is more sensitive to CO, CH_3OH, CH_4, CH_2O, C_2H_6O and further carbonaceous by-products [91] of the methanol-synthesis.

3.3.3 Titration

In the case of ammonia-synthesis the most accurate quantification routine is titration. Due to the very good solubility of ammonia in water (520 g/l ∼ 684 l/l at 20°C [92]), exhaust gas of a know volume was passed through an adsorber. Afterwards an aliquot was titrated with HCl in an automatic titrator. The dissolution of ammonia and HCl are described by the following equations:

$$NH_3 + H_2O \rightleftarrows NH_4^+ + OH^- \tag{3.19}$$

$$HCl + H_2O \rightleftarrows H_3O^+ + Cl^- \tag{3.20}$$

adding up both equations gives the titration reaction

$$NH_3 + HCl + 2H_2O \rightleftarrows NH_4^+ + OH^- + H_3O^+ + Cl^- \ . \tag{3.21}$$

While during the reaction water is in balance, one can reduce Eq.3.21 to

$$NH_3 + HCl \rightleftarrows NH_4^+ + Cl^- \ . \tag{3.22}$$

From the Henderson-Hasselbalch-Equation it follows that for NH_3 ($K_a = 9.25$ [92]) the pH is 5.28 at the equivalence point:

$$K_a = \frac{[H_3O^+][NH_3]}{[NH_4^+]} = 9.25 \tag{3.23}$$

$$pK_a = -\, lg K_a \tag{3.24}$$

$$pH = pK_a + lg\frac{c(NH_3)}{c(NH_4^+)} = 5.28 \tag{3.25}$$

Chapter 4

Continuous flow cell for catalytic reactions in the neutron beam [1]

Abstract In the present work the construction and application of a continuous flow cell is presented, from which neutron diffraction data could be obtained during catalytic reactions at high pressure. By coupling an online gas detection system, parallel structure and activity investigations of working catalysts under industrial relevant conditions are possible. The flow cell can be operated with different feed gases in a wide range from room temperature to 603 K. Pressures from ambient up to 6 MPa are applicable. An exchangeable sample positioning system makes the flow cell suitable for several different goniomter types on a variety of instrument beam lines. Complementary operational test measurements were carried out monitoring reduction of and methanol synthesis over a $Cu/ZnO/Al_2O_3$ catalyst at the high-flux powder diffraction beamline D1B at ILL and high-resolution diffraction beamline Echidna at ANSTO.

4.1 Introduction

Nowadays catalysts are considered as dynamic materials whose active centers can be formed or transformed due to the chemical potential of reactants or products under reaction conditions. If such changes are reversible, application of in situ methods is needed to study catalysts in their working state to gain a general understanding of structure-activity relationships. It is especially attractive to bridge the so called 'pressure gap' and to go to pressure ranges beyond Ultra-High-Vacuum to ambient pressure regimes. Unfortunately, not many in-situ techniques can be operated at high pressures above ca. 5 MPa and allow a direct observation of the working catalyst under realistic chemical potentials as are present in industrial reactors. It often remains questionable, if the properties of model catalysts studied at low pressure can be extrapolated to real catalysts under industrial reaction conditions. Due to their high penetration depth, neutrons allow application of complex sample environment as is needed to study commercial catalysts under industrial reaction conditions, e.g. elevated temperatures and high pressures (up to 6 MPa) under strongly reducing gaseous atmospheres like hydrogen/deuterium-rich synthesis gas. Furthermore neutron diffraction is a powerful tool to study structural and microstructural properties of a catalyst (phase identification, strain, particle size, alloy formation, phase transformations) in operation. A lot of technical effort was made by Turner et al. [65] and Walton et al. [66] to study catalysts or related materials under demanding reaction conditions; but still far away from typical industrial conditions. In this present contribution a reaction setup will be presented, which allows carrying out in situ neutron diffraction studies on various catalyst systems under industrial relevant synthesis conditions.

---

[1] Adapted from [3]

4.2 Apparatus design

Aim of the apparatus design was to build a safe reactor, which allows to collect structural data of a working catalyst under industrially relevant conditions with neutron diffraction and a parallel monitoring of the product gas stream by mass spectrometry to correlate structural and catalytic properties.

The apparatus consists of three basic components: The flow cell including the heated reactor body, the gas supply and the effluent gas analytics.

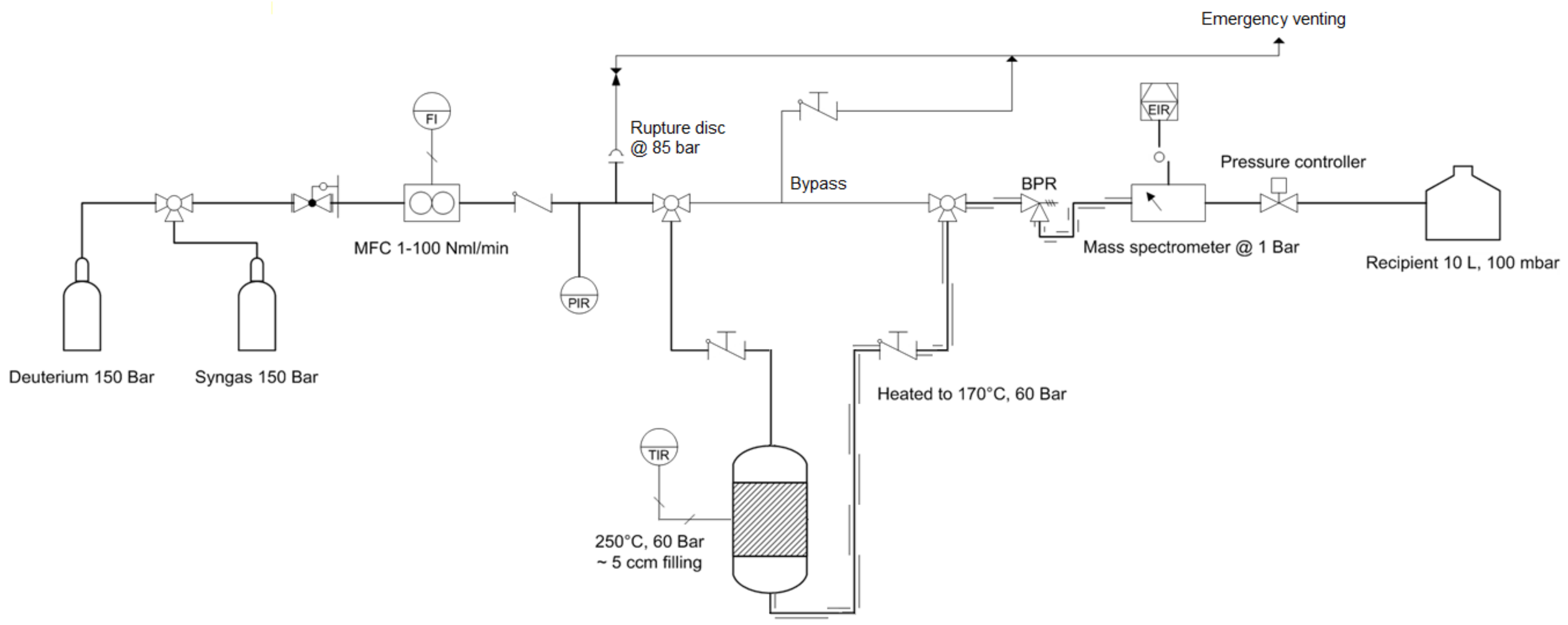
Emergency venting
FI
Rupture disc
@ 85 bar
Bypass
BPR
EIR
Pressure controller
MFC 1-100 Nml/min
PIR
Mass spectrometer @ 1 Bar
Recipient 10 L, 100 mbar
Deuterium 150 Bar
Syngas 150 Bar
Heated to 170°C, 60 Bar
TIR
250°C, 60 Bar
~ 5 ccm filling

Figure 4.1: Process flow chart of operating reactor including gas supply and effluent analytics. The system is kept under high pressure until the back pressure regulator (BPR). Gas analytics is carried out under ambient pressure.

4.2.1 Flow cell and reactor body

The operation of a flow cell under high pressure is devoted to strict safety regulations. According to these regulations, a bursting of the cell walls must be excluded at any time of the operation. The most critical point is the balance in between finding a material, which shows neutron transparency and a moderate coherent scattering behavior on the one hand and is resistant to high pressures of reactive gases like hydrogen, deuterium or carbon monoxide at elevated temperatures on the other hand. Most common materials used in the nuclear branch like vanadium and zirconium alloys show hydrogen embrittlement or intragranular corrosion [93], if they are operated under high pressures on a long term scale. Especially under alternating high pressure cycles, which occur under in-situ conditions a high tensile yield strength of the material must be guaranteed. We have decided to fabricate the cell from thick-walled aluminum-magnesium alloy EN AW-5754 (AlMg3) offering sufficient pressure and chemical resistance, low absorption and activation and still acceptable coherent scattering. The tubular flow cell was manufactured from a AlMg3 rod with a nominal outside diameter of 20 mm and a tensile yield strength of 283 N mm^{-2} at room temperature. Using a lathe, the outer diameter was reduced to 19.05 mm and a hole with a diameter of 10 mm was set through, which led to a effective wall thickness of 4.52 mm. Strain calculations by assuming a tensile yield strenght of 98 N mm^{-2} at 573 K [94] and a increased safety factor of 3.6 [95] have shown, that the tube is resistant up to the conditions of 140 MPa at 573 K. Static load tests of the setup have been successfully conducted at 9 MPa and 373 K for 2 h and the limits for flow operation has be set to 6 MPa at 603 K. The total length of the tubular reactor was 150 mm and the catalyst bed bathing in the neutron beam can have a length of up to 70 mm resulting in a volume of up to 5.5 cm^3. To achieve high intensity of the neutron diffraction patterns at short counting times, large sample sizes are required. The cell can be loaded with variable sample amounts from approximately 5 g to 20 g. The loaded catalyst bed is fixed by quartz wool plugs, which are inserted from both ends. A thermocouple which is inserted from the top allows to measure the bed temperature in the core of the catalyst bed during the reaction. Reactant feed is injected from the top, the product stream flows out at the bottom. Both ends of the tube are supported by crimped stainless steel adapting sleeves to assure a self-tightening seal. By inserting the end of the flow cell into Swagelok^{TM}stainless steel (SS 316) 3/4 to 1/4 inch reducing unions the cell material forms a tight seal in between the adapting sleeves and the inner mating tape of the reducing unions by its larger thermal expansion coefficient at 523 K.

The body of the reactor is also made of AlMg3, due to its good heat capacity and corrosion resistance. If the incident neutron beam is poorly collimated, the reactor body shows low activation behavior and shows a good radiation damage resistance [96]. Given that the body is made out of the same material as the flow cell itself, it is practically seamless in the diffraction pattern. Pedestras and sampling base plate are made out of SS316 and fixed with screws via threading. Six heating cartridges are inserted into holes in the reactor body with a total heating power of 600 W (2x 150 W, 4x 75 W), enabling heating rates of up to 5 K min^{-1}. Each heating element is equipped with a thermocouple to check its heating behavior for linearity and overheating. Loading of the filled flow cell is performed by removing the frontal heating covers and inserting the cell into the notch. The installed system with a total weight of 7.5 kg shows high temperature stability. An insulating cover and a convection-reducing thin Al-shield before the opening of the reactor body allows more efficient heating and more isothermal temperature profiles across the reactor. In case of potential power interruption the initial temperature loss is limited to 0.4 K min^{-1}. Safety precautions against over-heating are implemented by a bimetallic thermostat into the current circuit of the heating elements, which cuts of the power at a pre-defined temperature limit. The flow cell is equipped with a bypass to allow a proper purging of the lines at atmospheric pressure, which is important to avoid oxidation of the catalyst or local explosive atmospheres from residual air in the lines. The schematic process flow chart of the cell system is shown in Fig. 4.1, the detailed assembly of the reactor is shown in Fig. 4.2.

4.2.2 Gas supply

The lines of the feed gas supply are set under high pressure by a back pressure regulator (Tescom 44-1100) at the end of the product line. The pressurized gas lines are made of 1/8 and 1/4 inch stainless steel (SS316) tubing and connected with Swagelok couplings, fittings and reducing unions. The flow of the premixed syngas mixture (which had to be supplied at a pressure of ca. 7 MPa to achieve a stable outlet pressure of 6 MPa) was dosed using a mass flow controller (Brooks 5866) which was able to set a flow between 0 and 100 Nml min^{-1} in an operating pressure range from 0 to 10 MPa. The system pressure was electronically measured with an Endress + Hauser PMP 131 pressure transducer which was connected to a Schwille SPE 670 digital display and linked with a serial cable to a Labview application which allowed automated read-out and data-recording. For additional safety reasons a rupture disk with a specified relief pressure of 8.5 MPa and a check valve was installed between the outlet after the pressure transducer and the reactor inlet, which was able to shut down the gas supply in the case, the flow exceeded 500 Nml min^{-1} (e.g. in a case of a rupture). The pressurized product lines can be heated to 423 K–443 K to avoid condensation of products like steam.

4.2.3 Effluent gas analytics

Gas analytics is performed online at the heated product line beyond the back pressure regulator at atmospheric pressure. By switching the gas flow between bypass or reactor cell, the syngas composition or the effluent gas from the reactor can by analysed (e.g. for calibration). A gas chromatograph or a mass spectrometer can be coupled to the system. We have used the latter on site during the in situ experiments and the former in the laboratory to quantitatively study the system at the same conditions. During the neutron diffraction experiments a Pfeiffer Vacuum ThermoStar Mass spectrometer was used to check the progress of catalyst activation and whether the expected outlet gas composition

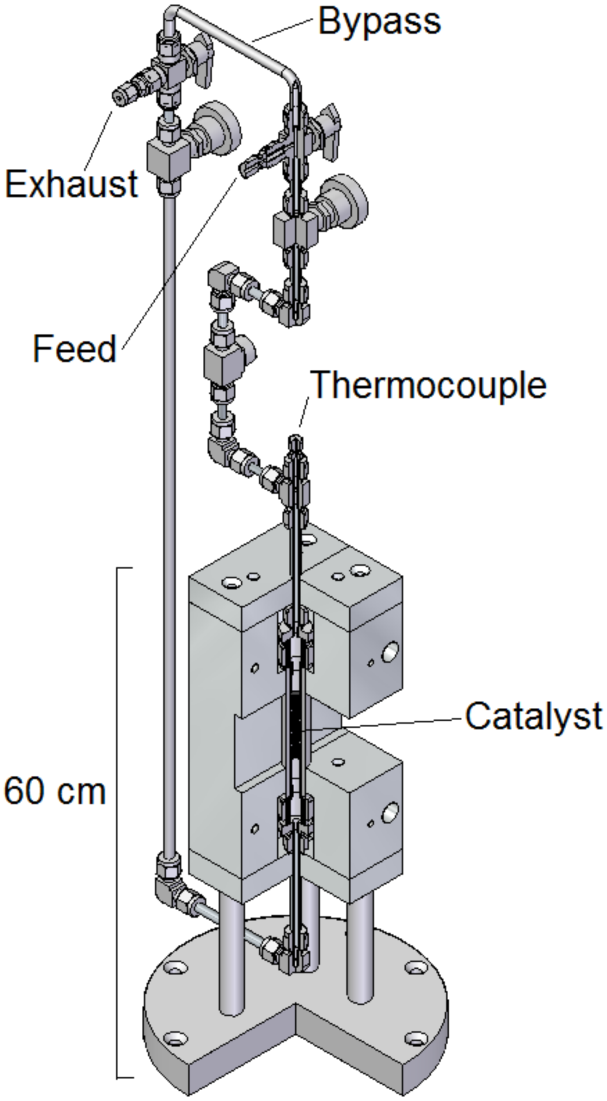
Bypass
Exhaust
Feed
Thermocouple
Catalyst
60 cm

Figure 4.2: Assembled flow cell inserted into the reactor body.

was reached. Effluent gases could be collected after online analysis in a condenser vessel or released into the venting system of the neutron facility.

4.3 Application example: Methanol synthesis

A prominent example for the importance of in-situ characterisation of structure-activity relationship in heterogeneous catalysis is the methanol synthesis over $Cu/ZnO/Al_2O_3$ catalysts. Even though these catalysts (in different compositions) have been used in commercial methanol synthesis for 45 years, the so-called synergy of Cu/ZnO is still under debate in literature. Several models have been introduced [31] which should give a first approach to properties of operating industrial catalyst systems. Some of the observations made on this system like brass formation, dynamical undergoing of morphological changes [40] have been directly obtained only on model catalysts under conditions, where no methanol has been produced. In the present work, the structural properties of the aforementioned industrial catalyst under realistic industrial synthesis conditions is studied using the flow cell reactor system described above. To minimize the effect of incoherent scattering, hydrogen was replaced by deuterium in the reaction gases.

4.3.1 Catalyst activation in high-flux diffraction

Due to their pyrophoric nature, nano-structured $Cu/ZnO/Al_2O_3$ catalysts are handled in their completely oxidized form, i.e. as $CuO/ZnO/Al_2O_3$, and the first step of a methanol synthesis experiment is the activation of the catalyst by reduction of the CuO component to metallic Cu:

$$CuO/ZnO/Al_2O_3 + D_2 \rightarrow Cu/ZnO/Al_2O_3 + D_2O \tag{4.1}$$

To study the phase evolution during reduction a commercial $Cu/ZnO/Al_2O_3$ catalyst the beamline D1B at ILL in Grenoble was used. While requesting the highest available neutron flux for a sufficient time resolution of the experiment, a focusing, highly oriented pyrolitic graphite monochromator was used to select a wavelenght of $\lambda = 2.52$ Å, which led to an effective flux of 6.5×10^6 n cm^{-2} s^{-1} at the sample [97]. By setting the $^3He/Xe$ position-sensitive detector to a take-off angle of 45° the angular range up to 125° 2θ (corresponding Q-range 1.91 $Å^{-1}$ to 4.42 $Å^{-1}$) was covered. The reduction of 6 g catalyst was carried out with a feed stream of 100 Nml min^{-1} pure D_2, while the bed temperature was ramped from 301 K at 1 K min^{-1} to 523 K at ambient pressure. Effluent gas composition was tracked by mass spectroscopy from m/z 0 to 50 in analog scan mode; the probing cycle was 11 s per spectrum. During the reduction procedure 250 patterns were acquired with an acquisition time of 5 min per pattern. The patterns were normalized to the monitor count rate. Afterwards the intensities of the CuO(11-1) at Q = 2.4925 $Å^{-1}$ and Cu(111) at Q = 3.0122 $Å^{-1}$ peaks were fitted using a pseudo-Voigt peak shape function. After normalizing them to the highest intensity they were plotted on an absolute timescale. The normalized integrated intensities of the Cu(111) and CuO(11-1) peaks are correlated to the catalyst bed temperature and the effluent gas composition in Fig. 4.3.

4.3.2 Working catalyst in high-resolution diffraction

High-resolution diffraction was performed on ECHIDNA at ANSTO by using a Ge(335) monochromator at an angle of 70°, delivering a highly collimated beam at a wavelength of $\lambda = 1.622$ Å. A large array of 128 position sensitive ^{3}He detectors cover an angular range of $4° < 2\theta < 164°$ which corresponds to a Q-range of 0.27 Å^{-1} to 7.7 Å^{-1} [98, 99]. The reduction of the catalyst was carried out on-site at the diffraction experiment under the same conditions as in the high-flux experiment. After reaching the temperature plateau at 523 K, the feed is switched to syngas consisting of D_2, CO_2, CO and Ar as internal standard and the flow cell is pressurized by the back pressure regulator with a rate of 78 kPa min^{-1}. The methanol synthesis reaction, formally according to

$$CO_2 + 3D_2 \rightarrow CD_3OD + D_2O \tag{4.2}$$

was conducted in thermodynamic equilibrium at 573 K and 6 MPa. After reaching stable operating conditions the effluent gas composition is monitored by mass spectrometry. At stable equilibrium composition of the effluent gas, diffraction patterns with 1 or 2 h acquisition time were recorded. The observed intensities in the monitor- and efficiency normalized patterns were evaluated by multiple peak-fitting to account for sample and cell-material contributions.

4.4 Results

With increasing temperature the reduction of the CuO-containing precursor phase is initiated around 388 K and finishes at 459 K. Metallic Cu appears in the diffraction pattern at 437 K. D_2 consumption starts around 373 K and ends in a regime, were CuO is completely reduced. Additionally to the moderate angular resolution of D1B, the poor crystallinity of all component in the nano-structured catalysts, in particular of ZnO and Al_2O_3 contributes to a relatively high background, which leads to a larger uncertainty of the low-intensity and broad peaks of CuO compared to the more crystalline metallic Cu. Complete conversion of D_2 was reached within the maximum of D_2O desorption in coincidence with metallic Cu evolution, which is in good accordance with literature [100]. No indication of intermediate formation of crystalline Cu_2O has been observed in the diffraction patterns. The asymmetric shape of the curves in Fig. 4.3 and their intersection at a normalized intensity < 0.5 suggest the presence of a undetected, probably amorphous intermediate, which may be a form of Cu(I)-oxide. Fig. 5.2 shows a diffraction pattern of a commercial $Cu/ZnO/Al_2O_3$ catalyst in operation under 523 K and 6 MPa pressure at equilibrium. The methanol concentration in the outlet stream corresponds to the calculated equilibrium value of 5 vol.%. Strong diffraction peaks from the cell material can be fitted by a pseudo-Voigt peak shape function (highlighted with green profiles). The peaks of the catalytically active Cu-phase of the catalyst (red profile) and ZnO (black profile) can be clearly distinguished, indexed and refined by Rietveld method. Such patterns can serve as a starting point to investigate the structural answer of a working catalyst to variation of the reaction conditions and to correlate such changes to catalytic performance. More detailed results of the methanol synthesis catalysts will be published elsewhere.

4.5 Discussion

A flow cell for in-situ neutron diffraction during continuous catalytic experiments under high pressure was designed and constructed. It was successfully tested for catalyst activation and methanol synthesis over $Cu/ZnO/Al_2O_3$ under equilibrium conditions at 523 K and 6 MPa while obtaining structural information of the catalyst. Online effluent gas analytics allows direct correlation of structural properties with catalytic activity. Earlier, comparable studies, which have been carried out with x-rays were done under conditions of 493 K and 3 MPa [72, 73, 41, 62]. Laboratory studies of the methanol synthesis in the constructed flow cell have proven the comparability with conventional catalytic test reactors. Thus it should be mentioned, that the major advantage of neutron diffraction - the angle-independent scattering intensity - allows the higher-order reflexes to be taken into account for a more accurate structure determination. Although there is a strong scattering signal from the flow cell wall material, the structural signature of the investigated catalytic system is strong enough to give detailed results concerning the crystal- and microstructure of a catalyst under industrially relevant reaction conditions.

Acknowledgements The authors would like to thank Michael Tovar, Alain Daramsy, Scott Olsen, Eugen Stotz, Edward Kunkes and Gregor Wowsnick for technical, DFG (German research foundation, BE 4767/1-1) and Süd-Chemie AG for financial support. Süd-Chemie AG is furthermore acknowledged for providing the catalyst and ILL and ANSTO for allocation of beamtime.

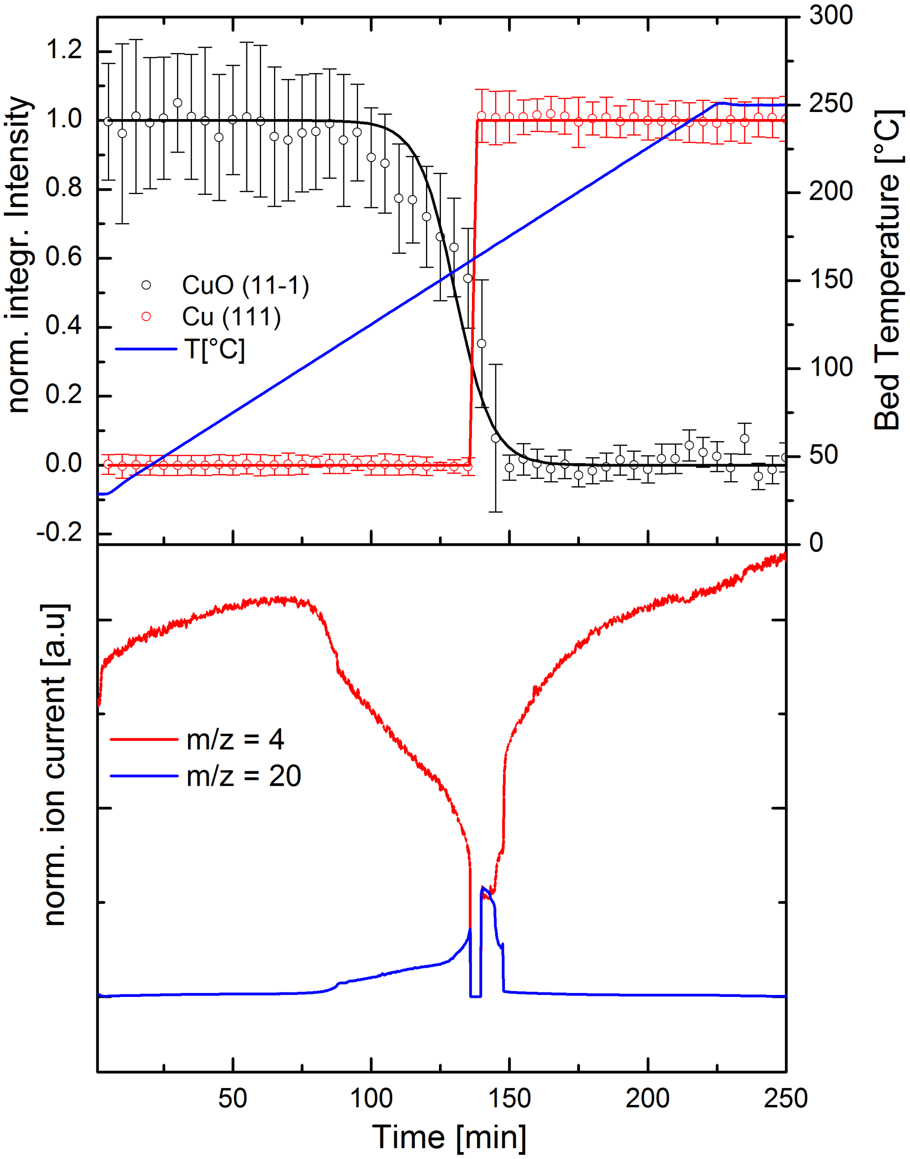

Figure 4.3: Reduction procedure of a commercial Cu/ZnO/Al_2O_3 catalyst. Normalized integrated intensities of the CuO(11-1) and Cu(111) peaks correlated with the catalyst bed temperatur (top) and effluent gas composition (bottom) during isobar reduction from 301 K to 523 K in D_2 feed. Missing ion-current between 130 min and 140 min is devoted to a artefact.

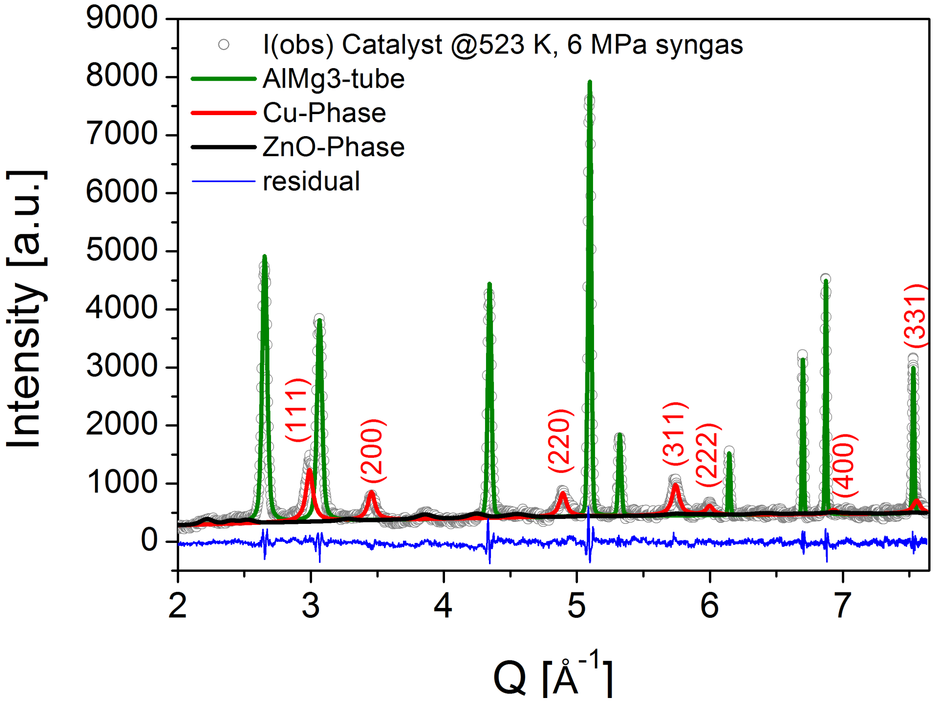

Figure 4.4: Rietveld refined neutron powder diffraction pattern of a working commercial $Cu/ZnO/Al_2O_3$ catalyst under syngas at 523 K and 6 MPa.

Chapter 5

Ammonia synthesis - proof of principle [1]

Abstract The present work describes the application of a tubular reactor that allows in-situ neutron diffraction on working catalysts at high pressures. The designed reactor enables the application to a sample of industrially-relevant reaction conditions, *i.e.*, in a temperature range up to *330°C* and *60 bar* pressure, coupled with online gas-analysis. Application of the cell is demonstrated by ammonia synthesis over a commercial catalyst with diffraction data obtained from the high-resolution powder diffractometer, Echidna, at the Australian Nuclear Science and Technology Organisation, ANSTO.

5.1 Introduction

Neutron diffraction is a unique tool to gain information on crystalline phases, the crystal structure, structural disorder, crystalline domain size and shape, lattice strain and defect structure, of materials including catalysts [86]. Nowadays, catalyst are considered as dynamic materials whose active centres are formed or transformed under reaction conditions. *In-situ* characterization methods are needed to obtain information about such structural dynamics, which are typically applied in the pressure range from ultra-high vacuum to ambient. The structural properties of the catalyst may change with the partial pressure of the reactants or products, and investigations of catalysts at high pressures and near industrially-relevant working conditions using *in-situ* neutron diffraction can provide valuable information on the nature of the catalytically active sites. Due to the high penetration depth of neutrons, they can scatter from samples deep within conventional metallic reactors without the use of specialized neutron-beam transparent windows, enabling the application of demanding sample environments that are not easily used with conventional X-ray diffraction. Additionally, the relatively large Q (=2π/d) coverage and non-decreasing scattering factors at high Q make neutron diffraction a suitable tool for *in-situ* studies of working catalysts, enabling crystallographic information at reasonable counting times to be obtained. This contribution presents the application of a custom-made high-pressure cell to the ammonia-synthesis reaction.

---

[1] Adapted from [4]

5.2 Experimental

For the purpose of *in-situ* neutron diffraction a high-pressure continuous flow reactor was designed. The flow cell, made out of an $AlMg_3$ alloy, is suitable for reaction temperatures from ambient to 330°C and a maximum pressure of 60 bar.[3]. Mass spectrometry was used during the *in-situ* neutron diffraction experiment for online gas analysis. Previous experiments in the laboratory have demonstrated the reactor functionality for the pretreatment of the catalysts, and continuously-running, stable catalytic conversions have been achieved. Relatively fast changes of the gas atmosphere are possible to introduce various probe gases (*e.g.*, N_2O reactive-frontal chromatography for copper-based catalysis [101]). The example described here was carried out on the high-resolution powder diffractometer, Echidna, at the OPAL reactor facility using a Ge 335 monochromator to provide a beam at a wavelength of λ=1.622Å. A large array of 128 position sensitive ^{3}He detectors enabled an angular range of 4°-164° in 2Θ to be covered, corresponding to a Q-range of 0.28Å^{-1} to 7.7Å^{-1} [99, 98].

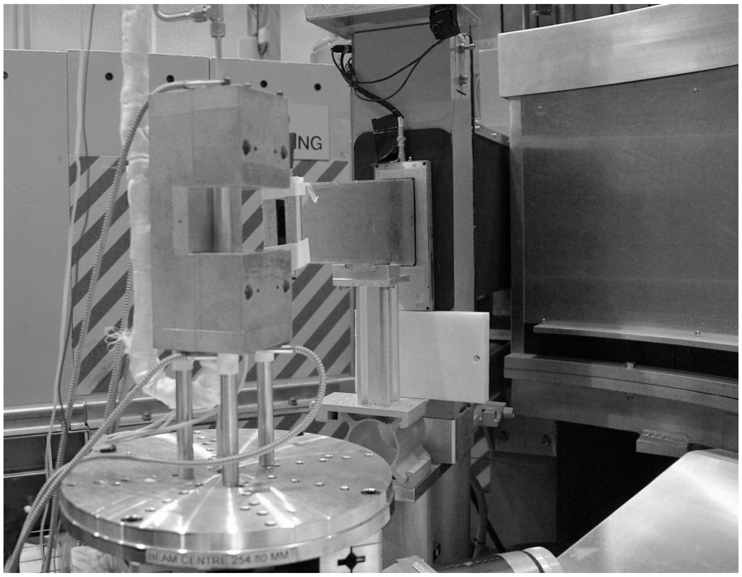

Figure 5.1: Flow reactor mounted on the Echidna instrument. The incident neutron-beam window is shown in the background.

5.3 Application example: Ammonia synthesis

Ammonia synthesis is not only one of the largest-volume synthetic chemical-processes applied in chemical industries, but also serves as a prototype reaction for heterogeneous catalysis research. Significant efforts to investigate the surface chemistry of model catalysts have been made in the last few decades using this reaction, as well as practical tests of high-performance catalysts [57].

Ammonia synthesis from nitrogen and hydrogen/deuterium (*see [102] for detailed mechanism*) is a structure-sensitive reaction, which does not occur on every form of metallic iron:

$$N_2 + 3D_2 \rightleftharpoons 2ND_3 \tag{5.1}$$

Commercial catalysts are so called "bulk-catalyst" with varying amounts of promoter species. The catalytically-inactive precursor material typically consists of fused iron oxides, e.g., approximately 80 vol.% magnetite, Fe_3O_4, and 20 vol.% wuestite, FeO. The specific BET-surface area of the catalyst is around 10 m^2g^{-1}, while the mean particle size of the wuestite/magnetite-precursor is roughly 10 μm. The catalytically-active form is called "ammonia iron" [103], which is produced from the fused iron-oxides by a complex thermal treatment in a reducing reactant gas-feed. Studies have shown [104] that the precursor material exhibits a disk-like internal microstructure, leading to long-term stable aggregates of α-iron-platelets separated by oxide spacers, which are favorable for the conversion of di-nitrogen. There is evidence that the active surface undergoes reversible reconstruction [105] under working conditions leading, for instance, to the formation of nitrides. In addition to pure iron [79], a metastable non-iron para-crystalline metal structure [106], a skin of Fe_4N or its under-stoichiometric variants [59] are discussed as catalytically-active phases.

The pre-activated α-iron catalyst was transferred under inert gas into the flow cell. After inserting the cell into the reactor the catalyst bed was carefully heated at 1 K min^{-1} under the reaction feed-gas to the reaction temperature of 330°C, a guard-reactor with the same catalyst was operated at 250°C. After reaching the reaction temperature, the cell was pressurized to 60 bar. When the detected ammonia concentration at the exhaust was stable, diffraction patterns with an exposure time of 2 h were acquired. For a stoichiometric gas feed of 100 Nml min^{-1}, a coversion of 3.63% was achieved while the productivity was 7.59 $mg_{ammonia}\ g_{catalyst}\ ^{-1}h^{-1}$. For accurate determination of the instrumental peak profile a LaB_6-standard was measured. Line broadening analysis using a pseudo-voigt-type peak-function with an axial-divergence term allowed to deconvolute angular dependencies on the integral breaths of the Lorentzian and Gaussian components.

5.4 Results

Fig. 5.2 shows the diffraction pattern of a commercial iron-catalyst in operation at 330 °C and 60 bar, wherein diffraction peaks arising from the cell were removed. Strong diffraction peaks of α-Fe (- - -) can be clearly distinguished and indexed. After deconvolution

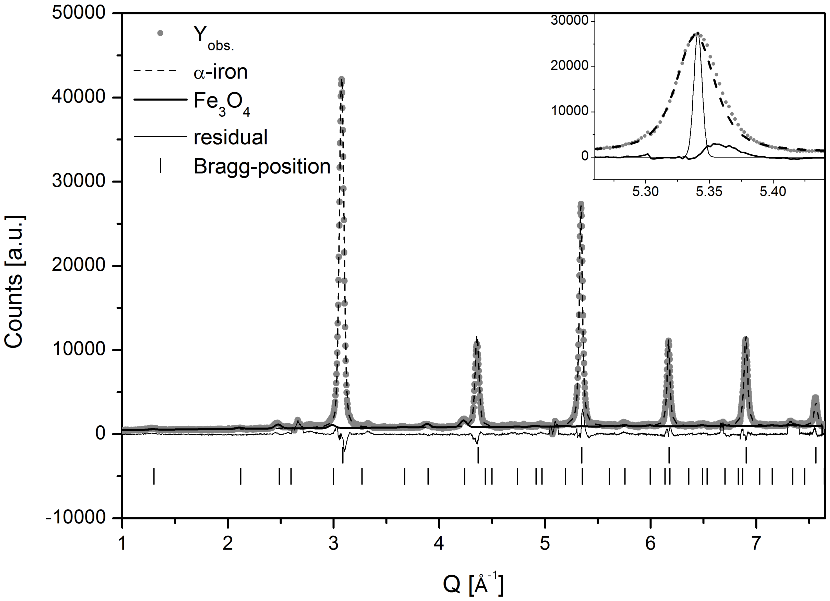

Figure 5.2: Neutron powder diffraction pattern of a working commercial ammonia catalyst at 330 °C and under 60 bar of syngas. A Rietveld-refinement based phase deconvolution was applied to the data. Bragg-positions of α-iron (top) and a spinel phase (structural model: Fe_3O_4, bottom) are marked, the difference between the model and the data is shown by the solid line above. The inset compares the asymmetric peak broadening of the 211 reflex of the α-iron-phase to the instrumental resolution function (narrow peak).

of the instrumental broadening from the diffracted intensities, the complex microstructure of the catalytically active α-Fe phase of the catalyst is indicated by the asymmetric peak broadening of the reflections as exemplified for the 211 profile shown in Fig. 5.2 (inset). In addition to metallic iron (a = 2.87840 (±0.00013) Å), there is also a noticeable contribution of a spinel phase (a = 8.38415 (±0.00022) Å), which can be refined using magnetite (Fe_3O_4) as a structural model (——). The refined lattice parameter is significantly shorter than expected for pure magnetite at 330 °C (8.4179 and 8.4245 Åat 300°C and 350°C, respectively [107]). On the other hand, it is much larger than expected for $FeAl_2O_4$ (Hercynite, 8.1695 Åat 400 °C [108]), which has been reported to form in ammonia-synthesis catalyst from FeO and the γ-Al_2O_3 promoter during reduction [109]. Our results suggest the presence of a non-stoichiometric and defective $(FeO)_x \cdot (\gamma\text{-}Al_2O_3)_y$ spinel-phase, in which the iron-cations are not reduced under *in-situ* conditions probably due to the interaction with Al in the spinel lattice. Transmission electron microscopy (TEM) studies (Fig. 5.3) revealed a complex composite microstructure of the catalyst with metallic iron particles and an embedding oxide matrix, wherein the promoter species (Ca, Al, K, Si, Ti, V) are enriched. This suggests that additional faint reflections arising in the level of background noise are attributable to small calcium ferrite crystallites. A careful correction

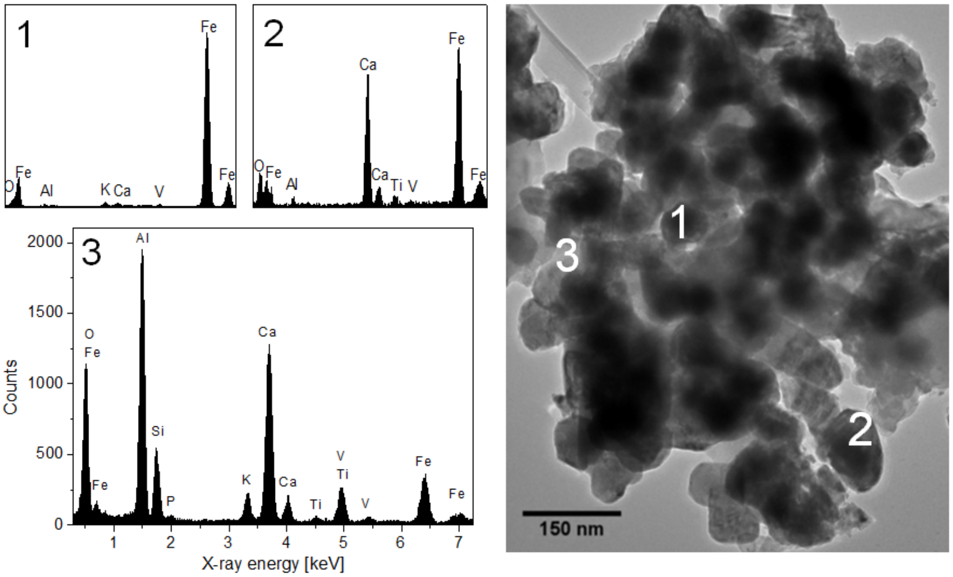

Figure 5.3: TEM micrograph and energy dispersive X-ray (EDX) spectra of the sample used during in-situ neutron diffraction. The point analysis spectra reveal that in addition to the α-iron particles (1) areas which are enriched in oxygen and in the promoter species are also present (2,3). These areas are found near the edges of the iron particles (2) and as an embedding matrix consisting of partially crystalline calcium ferrite/iron aluminum spinel (3).

for background artefacts will be mandatory for further evaluation.

In-situ neutron diffraction experiments as shown here are useful as a starting point for the further investigation of the structural changes occurring to a working catalyst during variation of the reaction conditions. Importantly, this information can be correlated to changes to catalytic performance. More detailed results of the ammonia-synthesis catalysts will be published elsewhere.

5.5 Conclusions

The constructed high-pressure continuous-flow reactor was successfully used in *in-situ* neutron diffraction on an ammonia-synthesis catalyst, working at 330°C under a pressure of 60 bar.

The preliminary data analysis confirms that all microstructural deviations of "ammonia-iron" that were derived at ambient pressure qualitatively also prevail at the technical harsh operation conditions. In particular, the absence of a stoichiometric iron nitride phase and the non-equilibrium structure of working metallic iron were confirmed to be no artefacts of low-pressure experimentation.

Acknowledgements The authors would like to thank Scott Olsen, Friedl Bartsch, Mai Anh Burke for technical support and the DFG (German research foundation) for financial support (BE 4767/1-1). Friedrich Karl Seitz and Frank Rosowski (BASF) are acknowledged for providing the catalyst and fruitful discussions.

Chapter 6

Microstructural and defect analysis of functional catalysts by diffraction and electron microscopy

Abstract The application of different methods for a microstructural analysis of functional catalysts is reported for the example of different Cu/ZnO-based methanol synthesis catalysts. Transmission electron microscopy and diffraction were used as complementary techniques to extract information on the size and defect concentration of the Cu nano-crystallites. The results, strengths and limitations of the two techniques and of different evaluation methods for line profile analysis of diffraction data including Rietveld-refinement, Scherrer- and (modified) Williamson-Hall-analyses, single peak deconvolution and whole-powder-pattern modelling are compared and critically discussed. It was found, that in comparison with a macrocrystalline pure Cu sample, the catalysts were not only characterized by a smaller crystallite size, but also by a high concentration of lattice defect, in particular stacking faults. Neutron diffraction was introduced as a valuable tool for such analysis, because of the larger number of higher-order diffraction peaks that can be detected with this method. An attempt is reported to quantify the different types of defects for a selected catalyst.

6.1 Introduction

The term microstructure summarizes all structural features of a solid state material beyond the ideal infinitely extended crystal structure, which in an analogous notation may be termed picostructure as it comprises the bond angles and distances between atoms on a picometer-scale and their periodicity. The microstructure includes particle size and shape, which can be studied conveniently with an optical or electron microscope in the micro- and nanometer range, respectively, but also other deviations from the ideal crystal lattice such as point, line and planar defects and clusters thereof as well as grain boundaries, interfaces, and crystal mosaicity. In the field of heterogeneous catalysis, knowledge of the microstructure of catalytically active phases is one important goal of catalyst characterization. This is not only true for the particle size as one of the determining factors for the specific accessible active surface area, but in particular also for the intrinsic properties of the surface and its faceting, which is determined by particle shape and size and surface defects. Such steps and kinks can substantially contribute to the catalytic performance in structure sensitive reactions. The increasing understanding of these effects was greatly fertilized by DFT calculations that showed, e.g., how lattice strain, surface steps and kinks or their poisoning will affect catalytic reactions such as ammonia synthesis [110], syngas chemistry [111, 112] or CO oxidation [113].

In experimental approaches, scanning probe microscopy and related techniques are very suitable tools to study the microstructure of model catalysts comprised of nanoparticles grown on flat surfaces [114]. In case of technically applied catalysts, however, usually powder diffraction methods and electron microscopy are used as complementary integral and local methods. While the latter allows a more or less direct observation of microstructural features [115], the former requires careful evaluation and analysis of the diffraction pattern and peak profiles [116]. In catalysis the most popular way of such evaluation is the application of the Scherrer formula on the width of a selected XRD peak. There are some examples of a deeper analysis of the microstructure of powder catalysts in the literature, e.g. for Au/ZrO_2 [117], Pt/SiO_2 [118], Ag/Al_2O_3 [119] and Ni-based hydrogenation catalysts [120]. However, often the routine microstructural analysis of diffraction data does not go beyond the simple estimation of the volume-weighted average crystallite domain size, which is obtained as the result of the Scherrer formula. One limitations of this analysis, which is unfortunately often not considered, is that it a priori assumes the absence of other peak broadening effects like lattice strain and that it give rise to anisotropic peak broadening effects if applied only for a single peak, typically the strongest non-overlapping XRD line. It also only yields average sizes and not size distributions, and if performed on a single peak is only valid for the crystallite dimension normal to the diffracting planes of the peak under study. Other complementary and more sophisticated methods for a microstructural analysis of diffraction data are available to address these issues [121, 122, 123]. These methods have mostly been developed in the field of materials science, e.g for metallurgy of construction materials, but can in principle also be applied for catalysts.

Two characteristics of applied catalysts need special attention and often complicate a straightforward adoption of these concepts. These are that i.) catalysts usually are multiphase composites, comprised for instance of active phase and support, which generate overlapping patterns while typically a special interest exists in only one, often in the minority phase; ii) highly active catalysts typically are nano-structured and often only weakly diffracting materials [116, 124]. In the recent past, our group has worked extensively on preparation and characterization of a family of catalysts that is to a lower extent affected by these problems, while still representing (or being closely related to) industrially relevant catalyst materials: Cu/ZnO-based catalysts for methanol synthesis. In the industrial formulation, the active Cu phase is the major component with a content of 50% or more and the Cu particle size in these catalysts is at the range of 5-15 nm [8] thus large enough to yield reasonable diffraction patterns of sufficient quality. Furthermore, it has been shown

Parameter	preparation condition	Cu:Zn ratio	BET Surface area^1	N_2O Surface area^2	normalized activity^3
	pH/T($°C$)/ageing (min)	nominal	m^2g^{-1}	m^2g^{-1}	$\%gm^{-2}$
C	6.5 / 65 / 60	100:0	34	6	0
CZ	6.5 / 65 / 60	70:30 110	26	37	
CZA-1	6.5 / 65 / 0	70:30	62	24	29
CZA-2	6.5 / 65 / 60	70:30	x	30	100

of

the calcined catalyst^1 ;^{2} of the reduced catalyst; ^{3} per Cu surface area, measured at 210 °C and 60 bar $CO/CO_2/H_2$

Table 6.1: characteristics of the investigated samples, values taken from SI of [9]

that the microstructure, in particular Cu lattice strain [36] and defect density [8] of the Cu phase, is an indicator of an increased catalytic performance and, thus, a microstructural analysis is directly relevant for understanding the catalysis of methanol synthesis. In a recent report [9], we have shown that the concentration of planar defects in the bulk of the Cu nanoparticles scales linearly with the surface area-normalized activity of the catalysts. This observation can be explained by the changes in surface faceting that are introduced by the termination of extended defects at the exposed surface of the particles forming steps and kinks. In collaboration with the SUNCAT group at Stanford, the higher catalytic activity was confirmed by DFT calculations that clearly showed that surfaces steps that were stabilized by planar bulk defects exhibit more favorable adsorption properties compared to flat Cu surfaces [9].

During this work, a set of characterization data, diffraction of neutrons and X-rays as well as transmission electron microscopy images, has been collected for $Cu/ZnO/(Al_2O_3)$ catalysts with different preparation history. Herein, we report a comparative microstructural analysis of a selection from these high-performance catalysts. The aim of this paper is to develop a consistent picture of the microstructure of Cu/ZnO-based methanol synthesis catalysts from different characterization techniques (TEM and diffraction) using various evaluation methods, but also to critically assess the different approaches and to review their limitations as well as their strengths in a scholastic manner. Furthermore, we want to advertise the careful application of sophisticated evaluation methods of diffraction data to characterize the microstructure of catalysts.

6.2 Materials and Methods

Four different samples were investigated in this study: two differently prepared ternary catalysts consisting of $Cu/ZnO/Al_2O_3$ (labeled CZA-1 and CZA-2), one binary Cu/ZnO catalyst that does not contain the alumina structural promoter (labeled CZ) as well as a macrocrystalline pure Cu-reference (labeled C-ref). All three catalyst samples are active in methanol synthesis and their relative catalytic performance as well as some major characterization data, which in part has been already published previously [9], is compiled in Table 6.1.

6.2.1 Sample preparation

The pure Cu reference catalyst C-ref was prepared by co-precipitation of a Cu^{2+} nitrate solution (1 M) with a basic solution of Na_2CO_3 (1.6 M) as the precipitating agent. The reaction was carried out at constant pH 6.5 at 65 $°C$ with an ageing time of 180 min. The blue green powder was isolated by filtration, washed with water and spray-dried. Upon calcination in air at 330 $°C$ for 3 h the hydroxide carbonate precursor was converted into the oxide, CuO. The binary sample CZ was synthesized accordingly, but using a mixed Cu^{2+}/Zn^{2+} nitrate solution (70:30 molar ratio). The ageing time was expanded until 30 min after a characteristic minimum in pH and a change in color from blue to bluish-green occurred [22, 17]. A ternary benchmark $Cu/ZnO/Al_2O_3$ catalyst CZA-2 was prepared accordingly, but with addition of 10 mol-% Al while the Cu:Zn ratio was maintained (Cu:Zn:Al = 63:27:10). This catalyst is a laboratory reproduction of the industrial catalyst following the well-established recipe developed by ICI in the 1960s [17, 18]. Another ternary catalysts CZA-1 was synthesized from an amorphous unaged precursor which was prepared by co-precipitation of a mixed Cu^{2+}/Zn^{2+} nitrate solution (1 M, 70:30) with an aqueous solution of Na_2CO_3 (1.69 M) containing 10 wt% $Na_2Al_2O_4$. The reaction was carried out at constant pH 6.5 at 65 $°C$ with simultaneous continuous pumping of the slurry to the spraydryer (21.6 ml/min) [30]. The residence time in the precipitation reactor was estimated to ca. 16-20 min. Thus in comparison with CZ and CZA-2, this catalyst precursor can be considered as unaged. Afterwards the blue powder was washed, filtered and spray dried again. Upon calcination in air at 330 $°C$ for 3 h all three catalyst precursors were converted into a mixture of the oxides. Around 7 g of a sieve fraction (250 - 355 μm) of the calcined samples were reduced in a fixed bed reactor (TPDRO 1100, CE instruments) in 5% H_2/He at 200 $°C$ (1 K min^{-1}, 80 ml min^{-1}) for 13 h and finally in 100% H_2 at 250 $°C$ for 5 h. The majority of the sample was used for the neutron diffraction experiments. A smaller part was passivated with N_2O and used for the catalytic tests reported in Table 6.1.

6.2.2 Neutron Diffraction

Approximately 5 cm^3 of the reduced sieve fractions were transferred under inert conditions into an indium-sealable vanadium sample holder for neutron diffraction. Neutron scattering data were collected using the Fine Resolution Powder Diffractometer (FIREPOD, E9) at BER-II research reactor hosted by Helmholtz Zentrum Berlin (HZB). The instrument works in Debye Scherrer geometry. The area detector consisting of 64 single ^{3}He detectors covers an angular range of $0° - 165° 2\theta$ with an angular resolution of 0.1°. By applying (711)-reflection plane of the Ge primary monochromator the wavelength $\lambda = 1.307666$ $\mathring{A}$ was chosen for the experiments. By this sufficient quality data could be gained within a scan time of 24 h per sample

6.2.3 X-ray Diffraction (XRD)

The catalyst CZA-1 was additionally investigated with XRD. The calcined materials was reduced before the measurement in an Anton Paar XRK 900 reaction chamber on a Stoe theta-theta diffractometer (Cu $K_{\alpha 1}$ radiation, $\lambda = 1.5418\ \mathring{A}$) equipped with a secondary graphite monochromator and a scintillation counter. For reduction the temperature was increased linearly in a 5% H_2 in He atmosphere (100 ml min^{-1}, 2 K min^{-1}) to 250 $°C$ and maintained isothermal for 2 h. The reduced catalyst was cooled to room temperature in the reduction gas before collection of XRD patterns ($30° - 100°2\theta, 0.02°$ steps, 16 s counting/step).

6.2.4 Diffraction data analysis

For sake of comparability, the diffraction data obtained from the X-ray or neutron diffractometer with different wavelengths (λ) was transformed from solid scattering angle (2θ) to a common abscissa in reciprocal space, Q, by Braggs law:

$$Q = \frac{4\pi sin(\theta)}{\lambda} \tag{6.1}$$

Instrumental broadening

The measured scattered intensity (I_{Qm}) was deconvoluted to account for the physical broadening of the sample due to size and structural imperfections (I_{Qs}) and the instrumental broadening (I_{Qi}), caused (in the case of x-rays) by wavelength dispersion and slits [125, 126] as well as axial beam divergence caused by monochromator geometry (in neutron diffraction) [127]. To determine instrumental resolution, adequate reference materials were measured [126]. For the present study LaB_6 was used for the XRD and Y_2O_3 for the neutron diffraction measurements. An attempt to describe the 2θ-dependence of the instrumental contribution was done by the experimental function described first by Caglioti et al [128], later simplified by Rietveld et al. [77]. A detailed description of modelling the instrumental resolution and deconvolution of the instrumental broadening can be found in the supporting information. Before peak deconvolution, the raw data has been smoothed using the Savitzky-Golay and weighted average filter.

Analytical profile functions for pattern decomposition

For the application of pattern decomposition methods, the experimentally observed line profiles in constant wavelength X-ray and neutron diffraction data were described by pseudo-Voigt functions (linear combination of Gaussian and Lorentzian profiles) as introduced by Wertheim et al. [129] with a mixing parameter η varying in a range from 0 (pure Gaussian) to 1 (pure Lorentzian):

$$I_{Q_m} = \eta \cdot L(Q) + (1 - \eta) \cdot G(Q) \text{ for } 0 < \eta < 1 \tag{6.2}$$

with

$$G(Q) = \exp\left[-\ln(2)\cdot\left(\frac{Q-Q_0}{H_G}\right)^2\right] \tag{6.3}$$

and

$$L(Q) = \frac{1}{1+\left(\frac{Q-Q_0}{H_L}\right)^2}\ . \tag{6.4}$$

The mixing parameter η relates the full width at half maximum (FWHM) H_{pV} of the peak profile to the FWHMs of the individual Lorentzian (H_L) and Gaussian (H_G) components. For the determination of instrumental broadening or in classical line profile analysis, the commonly used integral breadth β_{pV} is the ratio between integral intensity and amplitude. It can be easily derived by the shape mixing parameter η and the FWHM of the pseudo-Voigt peak H_{pV} according to:

$$\beta_{pV} = \frac{\pi H_{pV}/2}{\eta + (1-\eta)\left[\pi(ln2)\right]^{1/2}}\ . \tag{6.5}$$

Refinement and simulation methods

The refinement of structural parameters conducted along this study was performed using Diffrac.Suite TOPAS by Bruker [130] applying the well known algorithm introduced by H.M. Rietveld [77] that fits the observed reflection intensities by least-square minimization. For cases, where the scattering intensities between the theoretical and observed pattern differ tremendously, the software offers the possibility to perform a so-called hkl-fit by decoupling the structure factor coefficient from the linear addition. This method, the Pawley technique is a variation of the Le Bail-method [131], which uses the Rietveld-algorithm to estimate reflection intensities without a structural model, wherein the reflection positions are given by the generated unit cell of the phase. This is in particular useful, when a good fit is needed for irregular (asymmetric) profiles due to texture or dislocations or in the case of the presence of a phase with an unknown structure, the observed structure factor can be used for the structural model according to Rietveld-algorithm. The latter technique has been applied in this study. In the comparison with the convolutional fitting techniques (see below) all refinements done with the TOPAS software are referred to a Rietveld-type fitting in the discussion.

The simulation of the Cu-pattern with varying concentrations of coherent, intrinsic stacking faults was carried out with DIFFaX, a Fortran program, written by M. M. J. Treacy [132]. DIFFaX computes the average interference wavefunction scattered from each layer type occurring in a faulted crystal, by exploiting the recurring patterns found in randomized stacking sequences. In our simulations we used an infinite crystal size with a random sequence of intrinsic stacking faults in the [111] direction (ideal sequence in fcc: A-B-C-A) with a transition probability from 0.1 to 3.3% from A to B and vice versa. The reflection intensities in the calculated powder pattern where fitted with an analytical pseudo-Voigt function to determine their Fourier-coefficients as a function of the stacking fault probability α. Whole-powder-pattern-modelling (WPPM) was carried out with PM2K, a program, written and made freely available by M. Leoni [10]. In contrast to the linear addition of coefficients, performed in the Rietveld-algorithm, PM2K fits the observed intensity of a powder pattern by an ab-inito Fourier-synthesis of a theoretical pattern with least-square minimization. The initial structure model is defined by the input lattice parameter of the phase and its indexed reflection peaks. As any (micro-)structural feature of the sample contributes an average interference wavefunction, the determination of their specific Fourier-coefficients can be used to convolve them in the Fourier-synthesis (for details see supporting information). In our fitting procedure, the reflection intensities delta-function of the Cu-phase in the Q-space were convolved with instrumental broadening determined according [128, 77], a log-normal distribution of spherical particles (determined by TEM) with an average domain size determined from modified Williamson-Hall-Plot, a stacking-fault probability in accordance with simulated DIFFaX-profiles and linear (1D) edge and screw dislocations described by a burgers vector determined by TEM. The neutron wavelength, sample displacement, initial lattice parameters and the Chebyshev background-polynomial parameters were adapted from the previous Rietveld-refinement.

6.2.5 Transmission electron microscopy

A Philips CM200FEG microscope operated at 200 kV and equipped with a field emission gun and the Gatan imaging filter was used for TEM. The coefficient of spherical aberration was $C_s = 1.35\ mm$. The information limit was better than 0.18 nm. High-resolution TEM (HRTEM) images with a pixel size of 0.016 nm were taken at the magnification of 1 083 000× with a CCD camera.Projected areas have been measured and equivalent diameters calculated for 1500-4000 Cu particles in each sample; in all cases the values of standard error of the mean diameter were 0.5 nm or less. Frequency distributions of Cu particle sizes fitted well to log-normal functions.

6.3 Results and Discussion

6.3.1 Transmission electron microscopy

All three catalysts have been subjected to a detailed TEM and HRTEM study. Images taken at moderate resolution (Fig. 6.1a-c) confirm the nanostructured nature of the composite catalysts. The Cu metal particles appear darker than the oxide phase and exhibit an approximately spherical shape. It is noted that the Cu/ZnO-catalysts are not classical supported systems with extended support particles that may have a distinct orientation with respect to the electron beam. Cu/ZnO rather are bulk-catalysts with aggregates of Cu and oxide nanoparticles of comparable size. Thus, each image shows several dozens of Cu particles with a random orientation with respect to the electron beam. Because

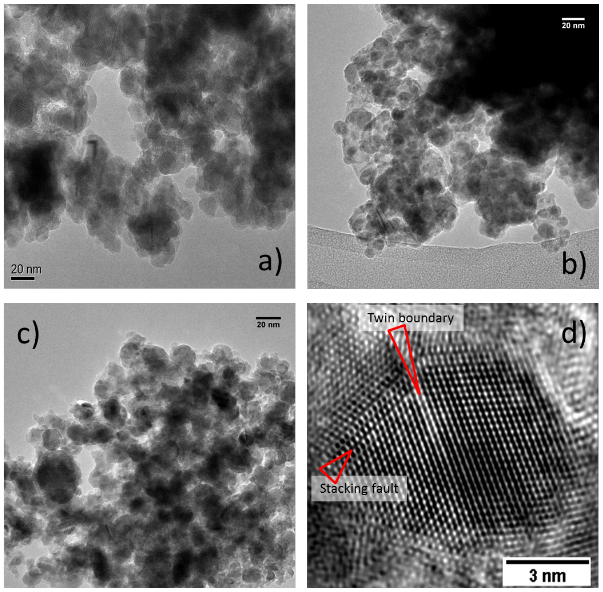

Figure 6.1: Representative TEM images of CZ (a), CZA-1 (b) and CZA-2 (c) taken at moderate magnification that were used for particle size evaluation. HRTEM image of a Cu nanoparticle in the sample CZA-1 that shows the presence of planar defects (stacking faults and twin boundaries, arrows). For more HRTEM-images cf. [8, 22, 30, 5]

the TEM images do only show circular projections of the Cu particles, it can be safely concluded that the particle shape can indeed be approximated by a sphere and is not, for instance, a projection of aligned nano-rods. Thus, after reduction, the Cu particles in the Cu/ZnO-based catalysts exhibit an isotropic shape and a surface faceting that does not favor exposition of large terraces.

Evaluation of the Cu particle sizes based on a series of several images such as shown in Figure 6.1a-c yielded the particle size distribution (PSD) curves as shown in Figure 6.2. The PSD histogram was found to be relatively uniform (see supporting information) and can be fitted with a log-normal function, which is in agreement with earlier work [30, 8]. From the PSD data, the volume weighted average Cu particle size has been calculated. It was 13.2 ± 0.1 nm, 10.5 ± 0.5 nm and 11.0 ± 0.2 nm for the catalysts CZ, CZA-1 and CZA-2, respectively (the ±-value being the standard error, not the width of the PSD). This result is in agreement with the observation that the presence of the Al promoter yields to smaller Cu particles and a higher resistivity of the microstructure against sintering during reduction [32]. The description of the catalysts microstructure based on these direct observations obtained by TEM appears to be complete and unerring. However, several well-known pitfalls have to be taken into account and are briefly recalled in the following. First of all, it is important to consider that TEM is a local method. Care has to be taken to ensure that the aliquot of material transferred in the microscopy is representative of the whole batch of material under study. Also, the images taken need to be representative of the whole aliquot, e.g. by taking an adequate number of different TEM images at moderate

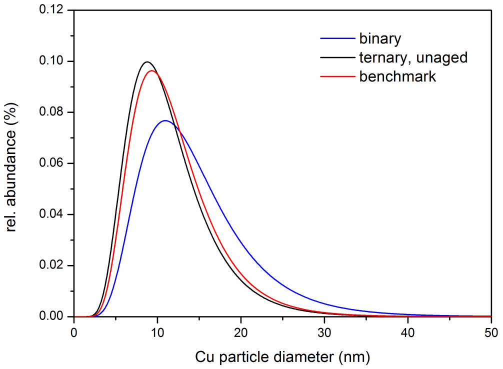

Figure 6.2: Log-normal fits of the particle size histograms obtained by evaluation of the TEM images of the three different catalysts (the histograms are presented as supporting information).

resolution at different locations of the aliquot. A selection of different TEM images used for the PSD evaluation of the sample CZA-1 showing different Cu/ZnO/Al_2O_3 aggregates of homogeneous microstructure is shown as an example in the supporting information. Concerning the former issue, it is important to assess the homogeneity of the sample by other complementary methods. This may include integral methods like diffraction to see if several phases are present (see below). But also other microscopy techniques of lower resolution like SEM can be useful to identify different types of material in a sample. EDX is especially important to detect local variations in the chemical composition that would indicate a heterogeneous sample. For the Cu/ZnO catalysts studied here, a relatively homogeneous microstructure was confirmed by a TEM-EDX study. The results for sample CZA-1 are shown in the supporting information showing that the fluctuations of the average local composition of the different Cu/ZnO/Al_2O_3 aggregates are lower compared to comparable catalysts reported in literature [8].

Based on such validated TEM data, a high validity range of the log-normal distribution of the particle sizes can be achieved, which requires a reasonable maximum relative error. Romeo et al. stated, that for a number larger than 1000 arguments (particles) the relative error reaches its minimum [133]. To safely exclude improper statistics to affect the results, at least 1300 particles have been evaluated for each catalyst in this study. Another source of uncertainty is the presence of very small particles below 3 nm. Their clear visibility in the TEM images is determined by contrast effects of the image generation and can be obscured leading to an underestimation of the lower-size tail of the PSD peak [134]. This effect is not only a function of the phase contrast between metal particle and support, but also depends on the quality of the used microscope and on the setting of the microscopy parameters for image taking [135]. Last, but not least the lower cut-off for the recognition of small particles critically depends on the eye of the operator. In particular in highly dispersed powder systems, the individual decision of the operator whether a small contrast variation is assigned to a particle or not will influence the average results. For example, in our group generally higher average volume-weighted particle sizes were obtained if the same TEM images were evaluated by a less experienced co-worker in all conscience. It is noted that the relative difference observed between different samples were usually confirmed by all operators. Thus, care has to be taken when comparing TEM-derived data reported in different literature studies, in particular if absolute values are concerned. The relative trend of a sample series determined under identical conditions by the same operator, however, can be regarded as reliable provided the material is homogeneous and the relative contrast of particles and support is comparable. However, it is certainly advisable in all cases to complement the size information determined by TEM by integral methods. Concerning our three Cu/ZnO-based catalysts, we conclude that both alumina-promoted CZA catalysts show relatively uniform PSDs with similar narrow widths, while the unpromoted CZ catalyst exhibits significantly larger Cu particles and a slightly wider PSD.

Additional information on the microstructure of the catalysts can be obtained from high resolution images. Due to the intrinsically bad statistics of HRTEM data, this information should not be used for quantification or extrapolation. However, atomic resolution images such as shown in Figure 6.1d enable inspection of the Cu lattice in individual particles concerning the presence of extended defects. Planar defects, stacking faults and twin boundaries, are found quite frequently in most investigated Cu particle of all catalyst samples. An example is shown in Figure 6.1d. These defects originate from imperfections in the stacking sequence of the close packed (111) layers and their influence on the diffraction peak profiles will be discussed below in more detail.

6.3.2 Phase identification and Rietveld refinement of the neutron diffraction data

The phase analysis and crystal structure refinement using the Rietveld method will be treated here on basis of the neutron diffraction patterns. The evaluation of the XRD results will be discussed later in section 6.3.5 that reverts on the results presented in this section. The advantage of neutron vs. X-ray diffraction is that the intensity scattered at the nuclei does not decay with Q, while X-rays interact with the spatially extended electron clouds of the atoms. Thus, higher intensity and a larger number of higher order peaks are usually detected at large Q using neutrons. This is in particular important for a more reliable refinement of highly symmetric structures with only few reflections such as the fcc-Cu structure in our catalysts.

The neutron diffraction patterns of the four samples are shown in Figure 6.3. All observed peaks do either belong to fcc-Cu or to Wurzite-type ZnO indicating the absence of other crystalline phases. It can be seen at first sight, that the Cu peaks of the catalysts are significantly broadened compared to those of C-ref. Furthermore, clear differences exist in the crystallinity of the ZnO component. As a first step of (micro)structural analysis, the Rietveld-refinement procedure [77] was applied to the raw patterns. This widely-applied method [121] is used to refine crystal structure parameters and to determine the phase fractions in multi-phase samples. The Rietveld method fits the whole pattern simultaneously by calculation of the expected intensity at a given Q and least-squares minimization of the difference between calculated and observed intensities through variation of the atomic structure parameters including atomic coordinates, Debye-Waller-factors and site occupancy. This method is very powerful and preferred to single peak and pattern decomposition methods in particular if the pattern is affected by peak overlapping. The best fits of the four samples are graphically represented in Figure 6.3. The lattice parameters of the Cu phases in the catalysts were 361.32 ± 0.06 pm, 361.26 ± 0.12 pm and 361.19 ± 0.15 pm for CZ, CZA-1 and CZA-2, respectively (the ±-values being 3× the estimated standard deviation of the Rietveld fit). These values are slightly lower than the lattice parameter refined for C-ref, which was 361.413 ± 0.012 pm, and close to the literature value. The Cu lattice compression in the catalysts samples is small but significant and consistently observed in all three catalyst samples. It is likely an effect of the nanostructured nature of the sample, which has been observed for many other metals [136, 137] and reported previously for this class of catalysts [5].

An important difference of the three catalysts is the crystallinity of the oxide phase. While in CZ the ZnO peaks are clearly present, they are much weaker in CZA-2, finally the pattern of CZA-1 can be satisfactorily fitted without any contribution of an oxide phase despite the similar ZnO content of all three samples. This is a results of the different preparation method as the suppression of precursor ageing as well as the presence of the Al_2O_3 promoter yields to a more amorphous ZnO component [30]. No crystalline Al-containing phase can be detected in the patterns of the two CZA samples. The observed differences in peak widths are typically attributed to small domain size and/or lattice strain effects. Both effects can be discriminated by the Q-dependence of the peak widths, which is stronger for strain broadening. The peak widths and profiles are determined during the Rietveld refinement foremost with the goal to model the experimental pattern as good as possible with the lowest possible number of refined parameters. Thus, the Q-dependency of the peak profile parameters is usually described using simple and steady functions with only a few parameters. Although these restrictions are certainly not optimal for a microstructural analysis of the peak profiles, most standard-Rietveld refinement programs have modules included that compare these few parameters with the instrumental resolution determined on a strain-free and macrocrystalline standard pattern and deliver a physical interpretation of this data in addition to the average crystal parameters. This procedure allows for estimation of the domain size as well as of the lattice strain, but it has to be taken into consideration that the Rietveld routine forces all different forms of peak broadening into this simplified scheme, regardless of its real physical origin. However, if only isotropic strain and isotropic size effects are present, i.e. the peak profiles can indeed be described reasonable well by a steady function over the whole Q-range, this method can deliver accurate results. It is noted that some Rietveld programs additionally allow the use of different Q-dependencies for different families of hkl, i.e. they take anisotropy of the size (shape) of the domain and of the lattice strain into account.

The Rietveld software package used for this study makes use of the so-called double-Voigt approach to differentiate between size an strain effects [138]. The crystallite domain size is

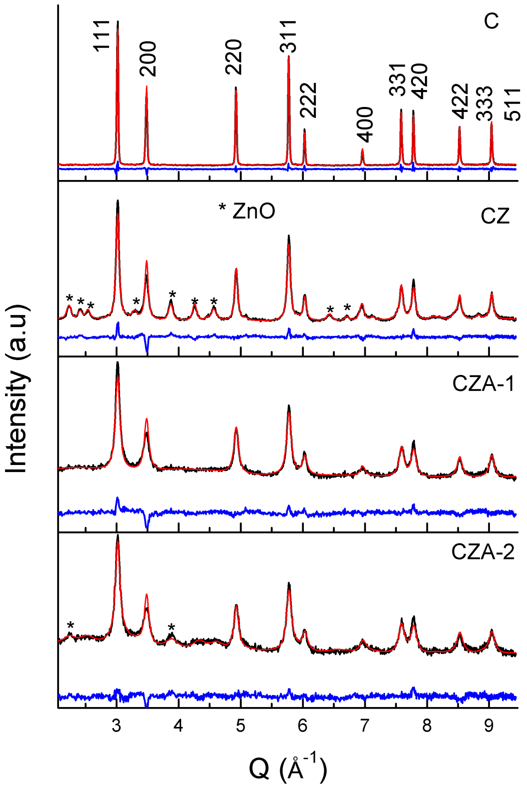

Figure 6.3: Rietveld plots of the C-ref material and the samples CZ, CZA-1 and CZA-2 and (black experimental data; red calculated pattern; blue difference curve). The peaks due to fcc-Cu are indexed in the uppermost panel, those due to Wurzite-type ZnO are marked *. Note the systematic deviations in the difference curves of the three catalysts.

given as an average volume-weighted column length based on the integral breadths of all reflections and amounts to 9.9 ± 1.2 nm, 5.8 ± 0.6 nm and 7.1 ± 1.5 nm for CZ, CZA-1 and CZA-2, respectively. These values are smaller than the particle sizes determined by TEM, but the relative trend of the three samples is in good agreement between both methods. Generally, a smaller size is expected for the coherently scattering domains determined by diffraction compared to the particle size determined by TEM as one particle might consist of several domains. This size discrepancy between TEM-size and diffraction-size can be related to the observed presence of planar defects in the Cu particles, because individual particles can be divided into domains by stacking faults and twin boundaries (see below). The lattice strain $\Delta d/d_0$ is extracted from the Rietveld fits as a Gaussian distribution of the lattice spacings around an average value d_0. Generally low values are observed for the catalysts and 0.05 ± 0.02%, 0.16 ± 0.06% and 0.07 ± 0.05% was found for CZ, CZA-1 and CZA-2, while an even lower value of 0.018 ± 0.004% was detected for C-ref.

While Rietveld refinement is the preferred method to determine the (crystalline) phase composition and any details of the average ideal structure (like the Cu lattice parameter), the quantification of deviations from the ideal structural model that was used to calculate the expected intensities has to be treated with care. This is because the strain and size values given above do usually not consider effects of anisotropy. Anisotropic peak broadening can be induced by different sources such as anisotropic particle shape, anisotropic strain and defects. Careful inspection of the difference curves of the best Rietveld fits shown in Figure 6.3 reveals clear indications for anisotropic effects in the three catalyst samples. It can be seen that the Rietveld routine does not succeed in accurately fitting all peak profiles of the Cu phase in the catalysts. Systematic deviations exist between experiment and calculated pattern as a result of the refinement yielding the best compromise for the peak profiles using the isotropic functions available. These deviations include an underestimation of the intensities of the 111, 311 and 420 peaks, while the 200 is overestimated and shows a negative residual in the difference curve. A similar but less clear effect is also observed for the higher order 400 peak, best seen in the pattern of CZ. Such systematic deviations are not observed for the macrocrystalline C-ref material. These deviations contain important information on the Cu micro- and defect structure that is not reflected in the Rietveld refinement results and will be evaluated in more detail in the following sections. Due to the isotropic cubic crystal structure of Cu and the approximately spherical shape of the particles seen in TEM, anisotropic size or strain effects can be excluded as the source of these deviations. As discussed by Warren [76] and later demonstrated by Balogh et al. [139] significant amounts of intrinsic stacking faults as well as twin boundaries can cause extensive anisotropic and nonuniform peak profile changes, which cannot be attributed neither to size nor to strain broadening. As the defective nature of our investigated material is known from earlier work [8, 9]and from the HRTEM results presented in Figure 6.1d, planar defects are the likely origin of these effects in the methanol synthesis catalyst. Tsybula et al. point out, that in case of nanocrystalline materials, local imperfections in the regular structure can be considered as elements of the nanostructure, being integral or specially imposed parts of the latter [121].

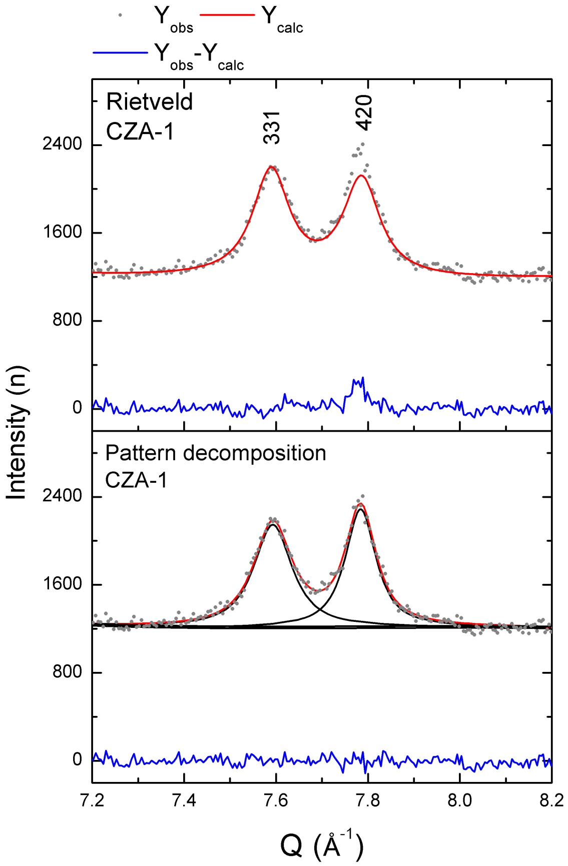

Figure 6.4: Comparison of the fitting results of the 331-420 peak doublet of CZA-1 using the Rietveld method and the model-free pattern decomposition method. The larger deviations between calculated and experimental data in the upper panel are due to the restrictions implied by the ideal structural model used for the refinement.

6.3.3 Pattern decomposition methods

Evaluation of a diffraction pattern using the pattern decomposition method is based on the description of the experimental pattern by the sum of several analytical functions for the peaks (here: pseudo-Voigt functions) and the background (e.g. a polynomial). Contrary to the Rietveld method, no structural model restricting the relative peak positions and intensities and no pre-defined form of the Q-dependency of the peak profiles is used. Thus, the primary result of pattern decomposition is a number of independent peak profiles containing Q-position, width and shape parameter. This method can be applied to single peaks, sections of the pattern or the whole data range. While extraction of structural information (lattice parameter) from this data is much less accurate compared to the Rietveld method, the peak profile parameters contain all information due to anisotropic effects needed for a full microstructural analysis. A comparision of Rietveld fit and pattern decomposition is shown in Figure 6.4 for the 331 and 420 peaks of the sampe CZA-1. These two peaks, which due to their high Q and often low intensity are only rarely recorded in XRD patterns of fcc nanomaterials, show an anisotropic broadening. The 331 at lower scattering angle is significantly broader compared to the neighbouring 420 peak. The Rietveld routine applied in this study tries to fit these peaks with similar widths and with interdependent positions given by the Cu lattice parameter. As a result, the intensity of the sharper 420 peak is not properly described in the calculated pattern. Additionally, only the outer tails of the doublet are adequately fitted while the inner tails are underestimated. As a consequence, the calculated spacing of the peaks is larger than the experimentally observed one. Naturally, the model-free pattern decomposition approach with its higher numbers of parameters and less restrictions allows fitting this feature more satisfactorily. It is noted, however, that this method generally deals much worse with peak overlapping and some instrumental artefacts like the zero-shift of the Q-scale that can be treated much better with the Rietveld method. For the analysis of the catalysts in this study, a combination of Rietveld and pattern decomposition was used to mitigate these problems. The zero-shift and the peak profiles of the ZnO phase (if present in crystalline form) were determined by Rietveld refinement and used for correction of the raw peak profiles of the Cu phase extracted from pattern decomposition. Furthermore, the instrumental contribution to the peak profiles was deconvoluted from the experimental data as described in the Appendix A.

Application of the Scherrer equation

As mentioned in the introduction, the application of the Scherrer equation is probably the most popular method of extracting size information from diffraction data, but it is subjected to several limitations that need to be taken into account for a physical interpretation of the results. P. Scherrer related the integral breadth β of a diffraction line to the finite size of the diffracting crystals normal to the diffracting planes, also named column length L, or apparent crystal size, by the expression [140, 141]:

$$L = \frac{\lambda}{\beta cos\theta} \tag{6.6}$$

The apparent crystal size D_{eff} can be obtained from the column length L by

$$D_{eff} = KL \tag{6.7}$$

wherein K is a form-factor (Scherrer-constant), which takes the size distribution of different reflecting planes (e.g. for spheres) into account. It has to be considered that a distribution of crystallite sizes will affect the breadth of a reflection in different ways [125, 76, 142, 143]. In case of a certain size-distribution (e.g. Log-Normal) a modified Scherrer-Constant must be used. Langford et al. described, that the breadth of diffraction maxima for crystallites having the same shape vary systematically with the indices of reflection. If a certain crystallite shape is known or assumed from additional methods, adequate values might be assigned to K [143].For this study, a value of $K = 0.89$ for spherical shape was used based on the TEM results (while $K = 0.9$ is recommended for cubic crystals and also in case of unknown crystal shape [125]). Applicability of Scherrer-Formula is restricted to pure physical broadening solely due to crystallite sizes below approximately 100 nm. Accordingly, the results obtained for the macrocrystalline C-ref sample should not be physically interpreted.

The crystallite domain sizes calculated by application of the Scherrer equation on the individual peak profiles obtained by pattern decomposition are presented in Table 6.2. It can be seen that the anisotropy of the peak profiles is reflected in variations of the calculated domain sizes. For example, within the sample CZA-1 the resulting sizes vary between 1.7 and 4.8 nm obtained for the 400 and 111 peak, respectively. This is a result of the anisotropic peak profiles already observed in the difference plots of the Rietveld refinements. Accordingly, the Scherrer approach predicts for all samples a larger domain size in the [420] direction compared to [331] as a result of the sharper peak profile of the former reflection, as seen in Figure 6.4. These variations shall not be interpreted as anisotropy of the particle shape, which as seen by TEM is rather isotropic. The average values are smaller than the ones obtained by the Rietveld analysis, probably because the strain contribution to the peak width is neglected in the Scherrer analysis. Even the size trend CZ> CZA-2 > CZA-1 that has been consistently found by Rietveld analysis and TEM is now changed to CZ > CZA-1 > CZA-2, which might be an artifact due to the slightly differences in strain.

The values in Table 6.2 are an example how important microstructural information can be

D_{hkl}	111	200	220	311	222	400	331	420	422	333/511	D_{eff}
	nm	nm	nm	nm	nm	nm	nm	nm	nm	nm	nm
C	16.62	15.67	18.12	18.61	19.01	17.68	18.07	18.92	18.15	17.42	17.83
CZ	6.72	4.89	6.38	6.13	6.93	3.85	4.91	6.16	4.61	5.48	5.61
CZA-1	4.79	3.99	4.52	4.67	4.81	1.65	3.46	4.29	3.80	4.06	4.00
CZA-2	4.08	3.30	4.25	3.96	4.07	1.54	3.21	3.89	3.85	3.47	3.56

Table 6.2: Results of the apparent crystal size determined by application of the Scherrer formula on the integral breadth of each individual peak resulting from pattern decomposition (K = 0.89). The averaged apparent crystal size is given in the last column.

easily overlooked if the analysis is solely based on Scherrer evaluation of a single arbitrarily chosen peak. It must be kept in mind that such one-peak evaluation gives only a crude estimation of the domain sizes, but does not reflect the whole microstructural information from the peak profiles and cannot account for anisotropic effects. The example of the Cu/ZnO-based catalysts furthermore shows that the resulting size domain information should not be pre-maturely interpreted as particle size.

Williamson-Hall Methods

In contrast to the Scherrer analysis, the evaluation of peak profiles obtained by pattern decomposition using the method of Williamson and Hall is able to discriminate between

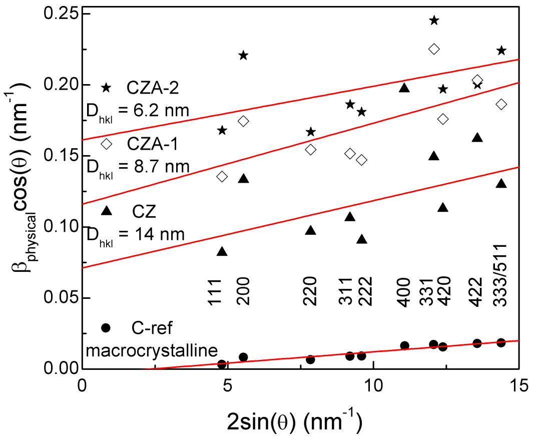

Figure 6.5: Williamson-Hall plots of C-ref and the three catalyst sample CZ, CZA-1 and CZA-2. The deviations of the three catalysts from linearity are discussed in detail in the text.

strain and size effects and yields average values of microstructural parameters [142]. In the case of negligible instrumental broadening (e.g. for certain synchrotron data or for a semi-quantitative evaluation of a series of samples measured on the same machine) the application can be straightforward, but otherwise great care must be taken to model or measure instrumental contribution very accurately.

The method assumes that, if the reflection profiles can be satisfactorily fitted by a pure Lorentzian function, the total physical broadening of a reflection profile is a linear addition of size (β_S) and strain (β_D) effects. The so-called Williamson-Hall plot is a good starting point for a quantitative description of the microstructure. For isotropic effects, the plot of$\beta_{total}(cos\theta)/\lambda$ (in nm^{-1}) versus $2sin(\theta)\lambda$ (in nm^{-1}) should results in a straight line. The crystallite domain size D_{hkl} can be derived from the intercept and the mean residual strain ϵ_{hkl} from the slope [144].

However, such a plot does hardly give straight lines for the three catalyst samples as shown in Figure 6.5. Only the macrocrystalline C-ref sample shows an almost linear distribution of the data points indicating that Cu-ref is the most isotropic material in the study as expected and in agreement with the other methods applied. Due to the large scattering, the Williamson-Hall plots of the other samples should not be evaluated in detail. The large deviation from linear regression can be interpreted as anisotropic behavior due to non monotonous 2θ-dependence of the diffraction profile widths [145]. Such anisotropy in Williamson-Hall plots was attributed to lattice dislocations/imperfections [146, 145] and/or twin faulting [75, 76].

Thus, the Williamson-Hall plots in Figure 6.5 are a graphical representation of the anisotropy that has been observed already in the systematic deviations of the difference curve of the Rietveld refinement and in the scattering of the domain size values obtained by the Scherrer analysis. Close inspection of Figure 6.5 reveals that the deviation from linear behavior is in particular caused by an extraordinary broadening (a too high value of $\beta(cos\theta)$) of the 200, 400 and 331 peaks those peaks that tend to be overestimated by the Rietveld algorithm and that deliver the lowest size values upon application of the Scherrer equation. Note that values for the 400 of the catalysts CZA-1 and CZA-2 are larger than 0.5 and not shown in Figure 6.5. If an attempt is made to quantify size and strain despite the non-linearity of the plots (red lines in Fig. 6.5, excluding the 400 peaks), crudely estimated size values are obtained that are larger than the Scherrer results and now fall closer to the results obtained by Rietveld refinement or TEM analysis (size data given in Figure 6.5, strain in supporting information). However, the results still suggest that the crystallites in CZA-2 are smaller than in CZA-1.

Ungar and Borbely introduced a modified Williamson-Hall plot, which they applied successfully on the line profile analysis of an ultrafine grain Cu specimen [147] that can account for the anisotropic behavior using an additional fundamental parameter, the contrast factor C. The average contrast factor $\overline{C}$ is a weighted average of individual contrast factors, which is obtained by averaging over all permutations of the Miller indices of a particular reflection. In the modified Williamson-Hall plot the FWHM ΔK^D is plotted versus a term $K\sqrt{C}$. ΔK^D is a strain term contributing to line broadening and D is the average grain or particle size ($K = 2\ sin\theta/\lambda$ and $\Delta K = 2\ cos\theta(\Delta\theta)/\lambda$ [147]. Ungar and Tichy point out, that the numerical calculated C factors of copper were averaged assuming equal dislocation population in each possible slip system and equal probability of edge and screw dislocations [146]. Numerical values for different slip systems as well as average $\overline{C}$ factors are given in the literature [147, 146]. The values used for C in this study were calculated according to [146]. For sake of conciseness the reader is referred to the literature [146, 147, 148, 149] for mathematical derivation and theoretical background. As the correlation is for spherical particles and the slope is fitted over several orders of reflections, the averaging Scherrer-factor of 0.9 (log-normal distributed spheres) was used in Eq. 6.6. The modified Williamson-Hall plots of the three catalyst sample are shown in Figure 6.6. It can be seen that the modified Williamson-Hall method deals much better with the anisotropy of the experimental peak profiles and that the deviation from linearity is less compared to the classical Williamson-Hall plots. Concerning the size data, the numerical results obtained from this method are slightly larger and can be considered as more reliable, but have no influence on the relative order of the catalysts.

The systematic deviations in the classical Williamson-Hall analysis and the fact, that the modification to take the effect of defects into account, delivers less deviation are additional indications that the microstructures of the methanol synthesis catalysts are affected by structural defects. The anisotropy induced by stacking faults in an fcc lattice is discussed in the following section in detail, concerning the effect of twin boundaries and line defects like dislocations, the reader is referred to the Appendix [150, 151, 152].

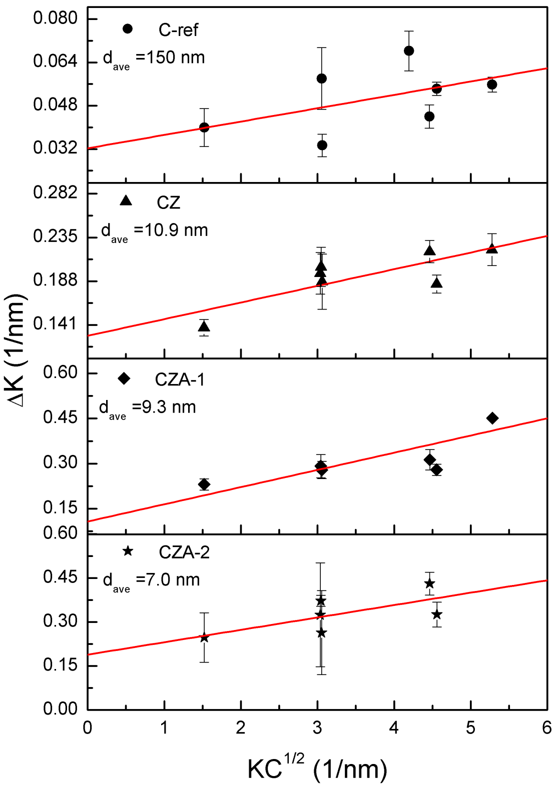

Figure 6.6: Modified Williamson-Hall plots of the C-ref and the three catalysts samples CZ, CZA-1 and CZA-2.

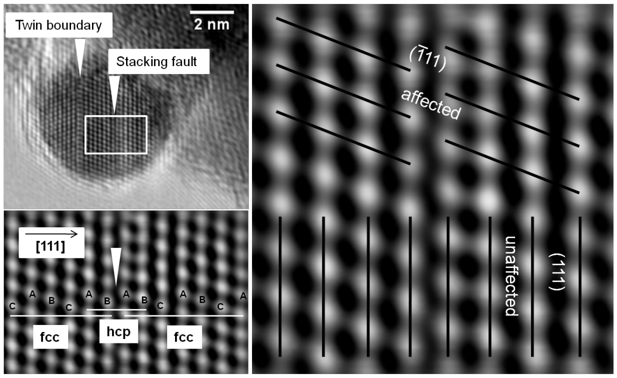

Figure 6.7: HRTEM image of a typical faulted Cu nanoparticle in a Cu/ZnO-based methanol synthesis catalyst. The close-up of the Cu lattice shows the stacking sequence of the (111) layers around the intrinsic stacking fault (left hand side) and exemplifies the different effects on the (111) and $(\bar{1}11)$ components of the 111 diffraction peak.

6.3.4 Anisotropy due to defects

Cu is known to form stacking faults in direction of the crystallographic [111] direction [76, 86, 74], the ideal stacking fcc sequence being A-B-C-A-B-C. By addition of an additional A layer one achieves a sequence of A-B-C-A-B-A-C-A-B an extrinsic stacking fault. According to Warren [76], extrinsic stacking faults do not contribute significantly to peak broadening; therefore only intrinsic stacking faults (missing C layer, A-B-C-A-B-A-B-C-A) are considered here. If an intrinsic stacking fault occurs, the fcc structure becomes locally isostructural to the hcp structure with a section of an A-B-A-B stacking sequence. The layer A is displaced to B by x=2/3, y=1/3 and z=1 and B to A by x=1/3, y=2/3 and z=1. This is a known source of anisotropic peak broadening as observed in the neutron diffraction data of the three catalyst samples. It is described in the literature and in many crystallography textbooks [76, 153] that stacking faults affect those components of the peak, for which $h + k + l = 3N \pm 1$, while components with $h + k + l = 3N$ are not affected. As an example, of the eight components of the highest 111 peak, six will be affected, while two remain unaffected. (The multiplicity of {111} is eight and the peak contains intensities diffracted at (111) and $(\bar{1}\bar{1}\bar{1})$, which remains unaffected, and at $(\bar{1}11)$, $(1\bar{1}1)$, $(11\bar{1})$, $(\bar{1}\bar{1}1)$, $(\bar{1}1\bar{1})$, $(1\bar{1}\bar{1})$, which will be affected.) To illustrate these two groups, the (111) and $(11\bar{1})$ planes are drawn into a HRTEM image of a typical faulted Cu particle [5] in Figure 6.7 representing peaks that are unaffected and affected by stacking faults in the (111) orientation.

In practice, this means that six components of the 111 peak will be shifted and broadened and form a shoulder at the higher angle tail of the 111 peak. This type of peak broadening will be most pronounced for those peaks that do not contain any contribution that remains unaffected, which are the 200 (6 components broadened and shifted to lower angles), the 400 (6 components broadened and shifted to higher angles) and the 331 (6 components broadened and shifted to lower angles and 18 components broadened and shifted to higher angles). Indeed, these three peaks that show the largest deviation from the linear behavior in the Williamson-Hall plots and deliver the lowest domain sizes in the Scherrer-analysis. Based on these qualitative considerations, also the systematic deviations in the Rietveld residual can be understood. For example, Figure 6.4 shows the inability of the Rietveld algorithm to adequately describe the peak profiles of the 331 and 420 peaks based on the ideal fcc model and an isotropic evolution of the peak width with Q. As a result of stacking faults, a net shift of the peaks towards each other (12 components of the 420 will be shifted to lower angle while 12 components will remain unaffected) and a larger width of the 331, which does not contain any unaffected components, can be expected. Indeed the experimental data clearly shows a narrower peak of the 420 resulting in a higher peak maximum compared to the 331. Furthermore, the extra intensity at the inner tails of the peak doublet indicates that the true peak positions are closer together on the Q-scale than calculated by the Rietveld software.

As shown above, the model-free pattern decomposition method can be used to analytically describe these small but systematic differences in the peak profiles. In a recent paper, we have applied such pattern decomposition to determine the peak positions and relative d-spacings of the 111 and 200 in comparison to the 222 and 400 for a series of Cu/ZnO-based methanol synthesis catalysts [9]. It was found that both pairs are shifted into opposite directions (111 and 200 towards and 222 and 400 away from each other) as is expected as a result of the presence of stacking faults. The deviation from the ideal value was used to quantify the stacking fault probability in the catalysts according to simple equations introduced by Warren [76]

$$\Delta(2\theta_{200} - 2\theta_{111})^\circ = \frac{-90\sqrt{3}\alpha}{\pi^2}\left(\frac{tan\theta_{200}}{2} + \frac{tan\theta_{111}}{4}\right) \tag{6.8}$$

$$\Delta(2\theta_{400} - 2\theta_{222})^\circ = \frac{+90\sqrt{3}\alpha}{\pi^2}\left(\frac{tan\theta_{400}}{4} + \frac{tan\theta_{222}}{8}\right) \tag{6.9}$$

where α is the stacking fault probability. As a result of stacking fault determination according to Eq. 6.9, a linear relation between stacking fault probability and the specific activity of the exposed Cu surface area was found. The stacking fault probabilities α of C-ref, CZ, CZA-1 and CZA-2 were 0.0018, 0.0061, 0.0050 and 0.0155, respectively [9]. This quantification is capable of finding reliable trends within a series of samples, but the absolute values suffer from the fact that it is solely based on the peak positions and neglects additional information from the peak widths and shapes. Velterop et al.[154] pointed out that the relation between peak maximum shift and stacking fault probability deviates from linear behavior above $\alpha = 0.025$, because the peak positions in the convoluted raw data are dominated by the unaffected components. Herein, we report an attempt to additionally use the full peak profile information for such quantification. The profiles of deconvoluted Cu peaks that are affected by stacking fault broadening can be simulated using the DIFFaX software [132]. The profiles expected for three different stacking fault concentrations are shown in the first row in Figure 6.8 for selected reflections. These profiles are generally much narrower than the experimental peaks, because in the simulation no additional sample or instrumental broadening was considered. The different evolution of the peak profiles with increasing stacking fault concentration can be seen. For instance, the 111 peak (222 peak) develops a shoulder at the higher (lower) angle side, while the 200 peak (400 peak) is symmetrically broadened and shifted to lower (higher) angles. However, for the 220 for instance no such clear trend is observed (Fig. 6.8).

To analyse the experimental peak shapes, the raw data has been deconvoluted by the instrumental contribution (see supporting information for details). Although the signal-to-noise ratio of the neutron diffraction patterns of the catalysts is lower than recommended for a thorough peak shape analysis [142], the quality of the data after smoothing is sufficient for an estimation of the number and relative position of the different contributions to the total peak profile. It should be noted, that only smoothing-routines, which do not affect the peak position should be applied (e.g. weighted average or Savitzky-Golay, the latter was used here), As seen in Figure 6.8, there is a good qualitative agreement between the simulated and measured peaks concerning the expected presence or absence of shoulders as a result of those peak components, which are affected by stacking faults. For example, a shoulder at the higher (lower) angle side of the 111 peak (222 peak) can be seen in all deconvoluted profiles of the catalyst samples, while the 200 peak (400 peak) do not show asymmetric broadening. Only negligible peak anisotropy was observed for the macrocrystalline C-ref sample. It is noted that, in contrast to the raw data, the deconvoluted peaks can be described by pure Gaussian, which indicates that macroscopic stresses can be neglected as a source of anisotropy. If only the affected components of the deconvoluted peaks are used for an estimation of the stacking fault probability α according to Eq.6.9 generally higher values are obtained as reported in Figure 6.8, in particular for the CZA-1 catalyst.

Summarizing the results obtained until this point, it can be concluded that a consistent picture of the catalysts microstructures emerges. There is a pronounced difference in particle and crystallite domain size between the binary CZ and the promoted CZA catalyst samples based on the results obtained by TEM and diffraction. Moreover, there are clear indications for the additional presence of structural imperfections that need to be taken into account for a complete description of the catalysts microstructures. These indications are deviations from isotropic behavior observed in the Rietveld, Scherrer, and Wiliamson-Hall analyses and in the deconvoluted peak profiles. The individual deviations might not seem dramatic, but careful inspection clearly reveals a systematic pattern that can consistently be explained by the effect of stacking faults in the Cu nanoparticles. It is thus important to keep in mind that defects can have a significant effect on the quantitative results, e.g., of the Scherrer evaluation. It is noted that in addition to the effect of stacking faults discussed above in detail, also twin faulting, dislocations and microstain will affect the diffraction peak profiles. A disentanglement of these contributions is not straightforward and an attempt will be reported in the following section.

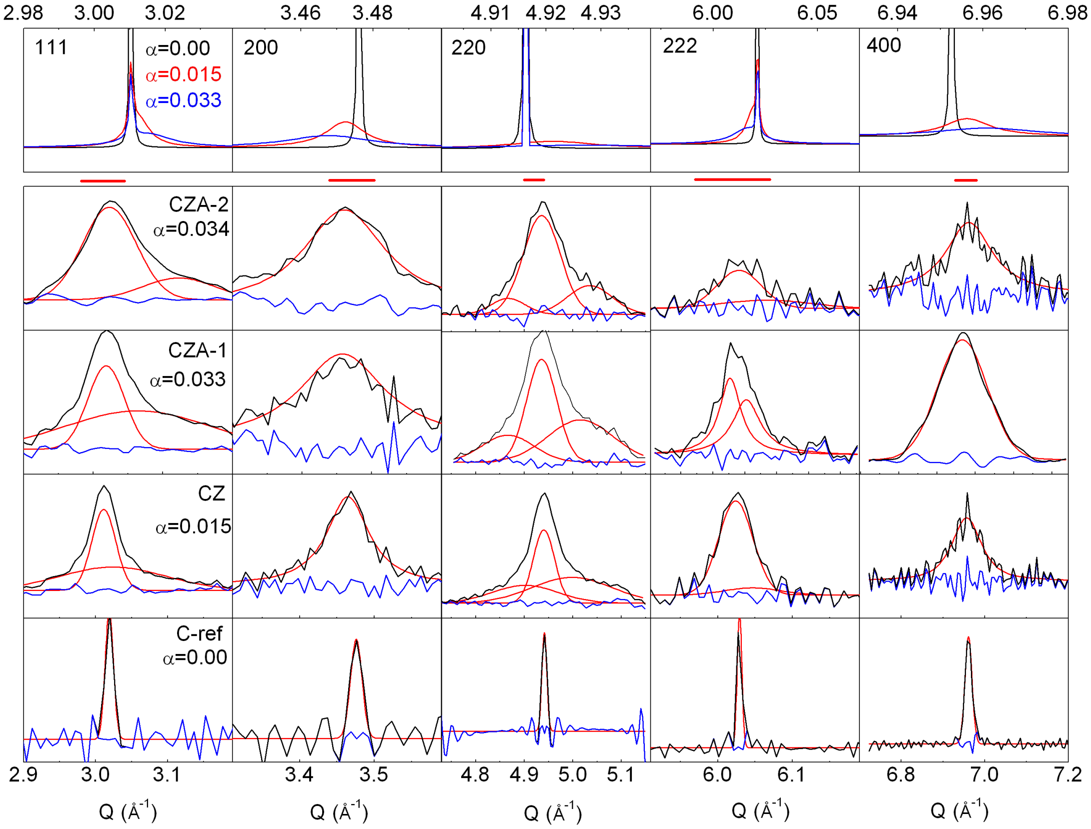

Figure 6.8: Deconvoluted smoothed peak profiles of CZA-2 (2nd row), CZA-1 (3rd row), CZ (4th row) and C-ref (bottom row) compared to DIFFaX simulations of stacking fault-affected fcc-Cu (1st row). The profiles of the 111 (1st column), 200 (2nd column), 220 (3rd column), 222 (4th column) and 400 (last column) are shown. The same deconvolution procedure was applied to all peaks and all experimental patterns. Note the smaller Q-scale for the 1st row on the uppermost panels, which is compared to the scale of row 2-5 by the red lines between the 1st and 2nd row.

6.3.5 Whole Powder Pattern Modelling (WPPM) including structural imperfections

WPPM of the neutron diffraction data

The WPPM method is the most sophisticated way to extract microstructural information on defects from powder patterns. In this section, the comprehensive analysis of the catalysts microstructure based on this method will be described. It is noted that accurate application of this method requires very high quality data in terms of signal-to-noise, preferably higher than in our neutron diffraction datasets. However, based on the previously obtained results from other methods that clearly confirm a visible effect of defects on the peak profiles and deliver reasonable starting parameters for the refinement and on the fact that the relatively high number of ten peaks can be simultaneously fitted, we report an attempt to use WPPM on the neutron diffraction pattern of the catalyst CZA-1 and the reference material C-ref, which are not affected by peak overlap due to the presence of other crystalline phase than Cu.
WPPM includes a Fourier-synthesis from the parameter-dependent Fourier-coeffcients (A_L) that allow the refinement of a variety of defect parameters. In comparison with the manual pattern decomposition methods used for the Scherrer and Williamson-Hall analyses or the peak deconvolution method as shown above, the major advantage of this method is that, unlike in Rietveld fitting, the whole pattern information is used simultaneously. In contrast to the Rietveld-algorithm, the methodology behind WPPM is a convolutional fitting of the experimental pattern. Each contribution to a scattered intensity in an experimental powder pattern, whether due to the ideal structural model or originating from structural imperfections, can be described by a simplified Fourier-series of the type:

$$I_{Q_m} = \int A_L exp(-2\pi i L Q) dL \; . \tag{6.10}$$

In this study the program PM2K written by Leoni et al. [10] was used. In addition to the lattice parameter of Cu, also the domain size D_{ave}, the stacking fault probability α, the twinning probability β, the average dislocation density ρ, the effective outer cut-off radius R_e, the Burgers vector b (describing the magnitude and direction of a shear caused by dislocation) and the stacking fault energy γ are refined to model the peak profiles. Thus, the methodology simultaneously accounts for the effect of various types of defects, and good starting parameters are essential to achieve a stable fit and physical meaningful results.
In a first step the initial contrast factors were refined with the C-reference without the inclusion of any defect model. The refined contrast factors are very similar to the values calculated from literature values of the anisotropic elastic constants for the modified Williamson-Hall analysis (see supporting information) and were applied to the catalyst sample. The crystal volume was calculated from the PSD determined by TEM (see above) and fixed during refinement. Initial values for α have been calculated according to equation

sample	a	D_{ave}	α	β	ρ	R_e	b	γ	GOF
	$10^{-1}nm$	nm	10^{-2}	10^{-2}	$10^{16}m^{-2}$	$10^{-9}m$	$10^{-10}m$	mJ/m^2	
C	3.6116	(21.13)	0.006	0.16	0.14	0.0002	2.5538	(3.8)	1.6779
CZA-1	3.6098	5.34	3.68	7.41	8.97	17.7	2.5525	18.1	1.2408

Table 6.3: Refinement results of the PM2K-fit of the neutron diffraction patterns of C-ref and CZA-1 (a = lattice parameter; D_{ave}=average domain size; α= stacking fault probability; β = the twinning probability; ρ = dislocation density; R_e = effective outer cut-off radius; b = the Burgers vector; γ = stacking fault energy; GOF = goodness of fit).

6.9 and via the relation $(1.5\alpha + \beta)$[76], β was directly determined through

$$\beta = \frac{a(1/D_{200} - 1/D_{111})}{1 - \sqrt{3/2}} - 1.5\alpha \tag{6.11}$$

using the Scherrer equation only on the unaffected deconvoluted peak contributions to determine D_{hkl}. The starting value for D_{ave} was taken from the modified Williamson-Hall analysis.

By using these initial parameters, a stable and reliable fit was achieved.

A direct comparison of the residuals from WPPM and Rietveld (Fig. 6.9) reveals the consistency of the underlying structural and defect model. It can be seen that the PM2K method deals much better with the experimental peak profiles and successfully models the anisotropic features that cause deviations in the difference curve of the Rietveld fit. For instance, comparison of the 331-420 region of the pattern reveals that the PM2K fit describes this doublet almost equally well as the model-free pattern decomposition method shown in Figure 6.4.

The results of the WPPM (Table 6.3) confirm once again that the difference between the macrocrystalline C-ref and the catalyst CZA-1 is not only the smaller domain (and particle) size of the latter, but that the Cu phase in the catalyst is substantially faulted and bears stacking faults, twin boundaries and dislocations that can explain the shifts and anisotropy of the peak profiles. The order of magnitude of the achieved stacking fault energy of the catalyst is in reasonable accordance with the literature results reported in the work of Reed and Schramm [152] who determined values in the range of 25 to 70 mJ/m^2 by XRD. Interestingly, the Burgers vector assuming an equal ratio between edge and screw dislocations, which is a general materials property of Cu, is refined to a similar value in both materials despite their very different microstructure. The slight lattice contraction of the Cu nanoparticles in the catalyst sample that has already been observed by Rietveld refinement is confirmed by the PM2K results indicating an overall consistent fitting result. Figure 6.10 shows an area-normalized comparison of the domain size distribution extracted from the WPPM-fit and the PSD as determined by particle counting in the TEM images. With the knowledge of the defective nature of the Cu particle, the discrepancy is easily explained by the difference in the underlying methodology. While in TEM the model is fitted to the appearance frequency of the particles (with a real space diameter), the WPPM

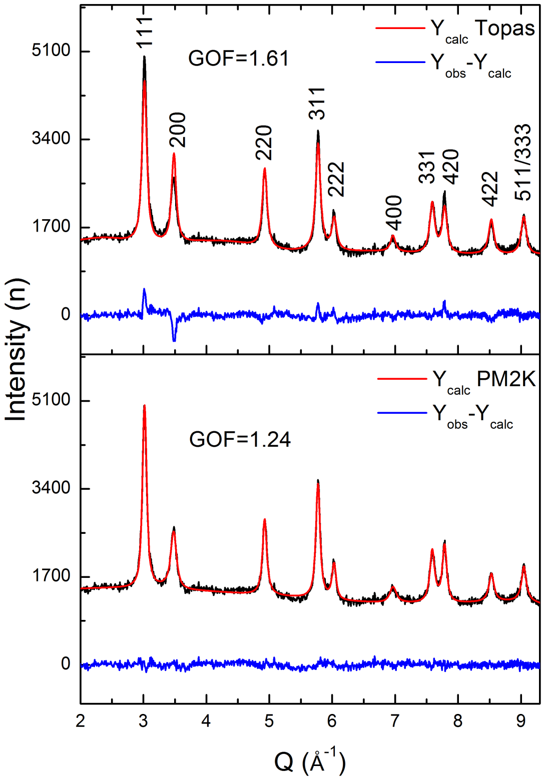

Figure 6.9: Comparison of the best fits using an ideal structure model (Rietveld, upper panel) and a methodology that accounts for the presence of lattice imperfections (WPPM, lower panel)

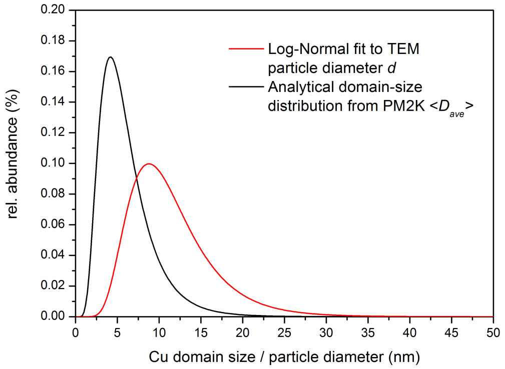

Figure 6.10: Comparison of area-normalized distribution functions for the domain sizes extracted from the WPPM and the particle sizes determined by TEM.

distribution assumes a relatively narrow log-normal distribution of coherently scattering domains around D_{ave}. Figure 6.10 can be interpreted in a way that each particle observed in TEM (approximately 10 nm) roughly consists of two domains of a size of approximately 5 nm, which are separated by a planar defect.

Analysis based on standard-XRD

The use of X-rays for diffraction experiments is much more common and as this is a laboratory technique also more convenient than neutron diffraction. In catalysis research XRD is a standard technique for catalyst characterization, but the application of microstructure analysis methods, with the exception of the Scherrer formula, is not routine. In this last section, we discuss how the features of anisotropy affect a standard XRD pattern for the example of the CZA-1 catalyst. The comparison between the Rietveld and WPPM fit is shown in Figure 6.11. The problems of the Rietveld fit are less obvious in the XRD data and only clearly seen for the first two reflections. However, if carefully inspected, Figure 6.11 shows similar phenomena as discussed previously in detail for the neutron data. The ideal structural model cannot simultaneously fit the more narrow width of the 111 and the shifted position of the 200 in an adequate manner. In the light of the above considerations, the experienced XRD scientist can find indications for defects in the typical down-up-down and up-down pattern of the difference curves of the 111 and 200 peaks even in this routine XRD pattern of standard quality. Indeed, the WPPM-fit can describe the experimental data much better taking the presence of defects into account. It is noted that also a full quantitative defect analysis of fcc metal nanoparticles is possible based using the WPPM method on XRD data as has been shown by the group of Weidenthaler for Au/ZrO_2 catalysts [116], but such complete analysis requires extremely high quality data.

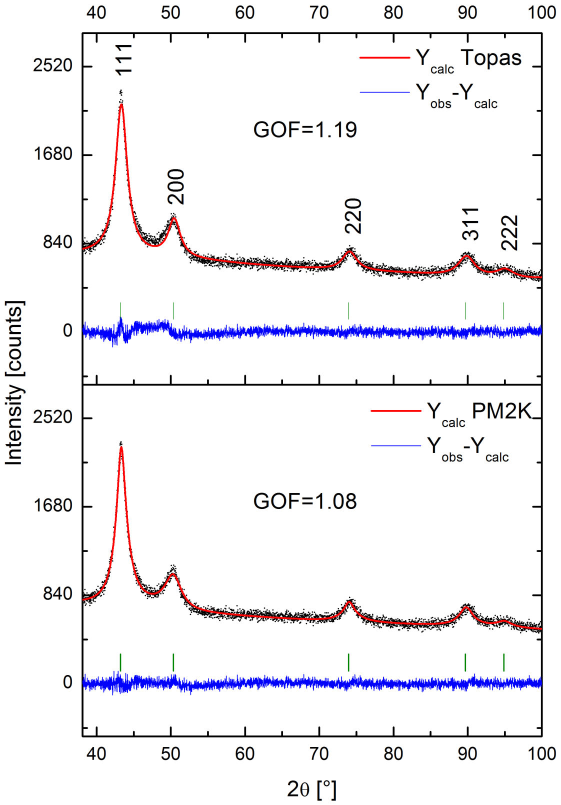

Figure 6.11: Full XRD pattern of the sample CZA-1. The upper panel shows the best fit obtained by Rietveld refinement without considering structural imperfections, while the lower panel is the WPPM fit taking defects into account.

6.4 Conclusion

As discussed in the sections above, fcc metals like Cu can contain a large number of lattice imperfections of different dimensionalities ranging from vacancies over edge or screw type dislocations to areal defects such as stacking faults and twin boundaries. The observed intensity in a diffraction pattern is a convolution not only of the contributions due to the reflecting planes and instrumental broadening, but also of such lattice imperfections and of contributions due to size distribution. This can be used for a microstructural analysis of diffraction data, for which well-established methods are available whose application unfortunately still an exception in catalysis research. For the example of the methanol synthesis catalysts, it was shown that the presence of defects yields to deviations from an isotropic evolution of the peak profiles with Q in neutron diffraction patterns of several nano-structured Cu/ZnO-based materials. In comparison with a macrocrystalline pure Cu reference sample, clear indications for the presence of stacking faults in the catalysts Cu particles have been observed in the residual of the Rietveld fits, in the scattering of the peak widths extracted from pattern decomposition, in the profile analysis using peak deconvolution as well as in the whole power pattern modelling. The existence of this type of defect was furthermore directly proven by HRTEM observations. In comparison with the domain size determined by diffraction methods, the particle size found the TEM images was significantly larger, which also points to the presence of planar defects that may separate the nano-particles into individual smaller domains.

The deconvolution of the instrument function from the experimental pattern is mandatory to quantitatively describe the faulting probability. By an accurate determination of the apparent crystallite size with the help of the symmetric analytical fit of the unbroadened peak contributions by the classical Scherrer or modified Williamson-Hall analysis, physically meaningful values can be achieved. However, as the classical models for determining domain sizes from diffraction data rely on the assumption of uniform and mono-modal particle size distributions, complementary TEM studies are mandatory. Furthermore, it is noted that the results obtained by peak deconvolution exhibit high sensitivity to smoothing if such process was applied on noisy data. The (semi)quantification of microstructural parameters like size and defect concentration of the catalysts CZ, CZA-1 and CZA-2 yielded different absolute values depending on the method used. Concerning the size, a clear trend was found among the three catalysts showing that the unpromoted catalysts CZ was least-nanosized, while the two differently prepared Al_2O_3-promoted catalysts exhibit similar crystallite sizes. Depending on the method used, only slight but significant relative differences concerning these two samples were also observed. The large differences in the exposed Cu surface area between these catalysts must, however, be explained by embedding of the Cu particles in CZA-1 in the amorphous oxide matrix. Concerning the defect concentration, the relative results are not so clear. Based on the determination of the stacking fault probability from the peak shifts, CZ and CZA-1 show lower values than CZA-2 in agreement with the intrinsic catalytic activities. Based on the analysis of the deconvoluted peak profiles, both ternary CZA catalysts are richer in defects than the binary CZ. For the datasets reported in this study, we regard the peak shift method as more

Method	Measure	Mark
Integral breadth	coloum length	L
Scherrer-Formula	apparent crystal size	D_{eff}
Rietveld	volume-weighted domain size	D_{vol}
TEM	particle diameter	d
Modified Williamson-Hall	average domain size	D_{ave}
WPPM	average domain size	D_{ave}

Table 6.4: Difference in the measure of the "size-effect" according to specific methods.

reliable regarding the relative differences of the catalysts, because the peak maxima can be more accurately determined even for unsmoothed profiles. In any case, care has to be taken when comparing absolute data of size or defect concentrations that have been determined by different methods. To be more concise, table 6.4 summarizes the difference between different measures all describing "size-effect" determined by the introduced methods.

The most sophisticated method of defect analysis from powder diffraction data is the WPPM, but high quality data and proper initial parameters concerning instrumental contribution, faulting probability, dislocation density, linear expansion properties and particle size distribution are required, which is often a problem for realistic catalysts. However, a good measure for the quality of a fit is rather a matching, flat residual than numerical correlation factors. If this is obtained with physically plausible parameters and in general accordance with the results achieved with complementary methods, a reliable (semi-)quantitative microstructural characterization should also be possible for many catalysts. Qualitatively, the typical signature of planar defects on the peak profiles can be sometimes already seen in standard XRD evaluation, if the fitting residual is carefully inspected as was shown for the methanol synthesis catalysts under study. For such complex composite nano-materials, we recommend the comparative application of different line profile analysis methods to scan for consistent anisotropic effects. This can already by easily done using a simple pattern decomposition method like the Williamson-Hall analysis or even the Scherrer method if applied on more than one reflection always bearing specific physical limitations and expressiveness in mind.

Chapter 7

The in-situ structure of a methanol synthesis catalyst [1]

Heterogeneous catalysts are dynamic materials that interact with the gas phase present in catalytic reactions. Changes that may occur when a catalyst is in contact with reactive molecules comprise adsorbate-induced surface reconstruction [155, 156], surface segregation [157, 158], inclusion of foreign atoms from the gas phase into the sub-surface [159] and compound formation in the bulk such as oxide [160], hydride [159], carbide [161] or nitride [56] formation of a metal catalyst. These modifications will affect the catalytic properties and depend on the chemical potential of the gas phase species. An extrapolation of experimental results obtained at low pressure to pressure regimes of industrial relevance is often not straightforward (”pressure gap”[162, 163]). To better understand the impact of dynamic catalyst changes, application of in situ techniques [164, 165] working at industrially relevant conditions is desirable. Here, we report on the potential of neutron diffraction (ND) as a tool for in situ analysis of heterogeneous catalysts. ND studies have been carried out on many inorganic materials in various sample environments [166]. Pioneering in situ ND studies of catalysts has been performed by Turner et al.[65] and Walton et al.[66] Inelastic neutron scattering was used for catalyst characterization by the groups of Albers, Lennon and Parker.[67, 68, 69, 70, 71] Similar to in situ XRD,[167] ND is complementary to other in situ techniques used in catalysis research, such as ambient pressure XPS,[168] XAFS[62] or Raman spectroscopy [169]. It is uniquely suitable for in situ-studies in thick-walled metallic tubular reactors which allow application of realistic reaction conditions. No special pressure-tight windows or complex reactor design is required, if a wall material is chosen that shows only minor absorption of neutrons and thus allows sufficient penetration through the walls [3]. ND is a bulk-sensitive method that gives quantitative, average structural (lattice constant) and microstructural (domain size, lattice strain, defects) information. In contrast to XRD, the scattering power is independent of the diffraction angle providing diffraction peaks at higher angles with higher intensity. This is in particular useful for the investigation of highly symmetric nanomaterials that often suffer from few and weak XRD peaks available for structural analysis. Figure 7.1 compares ex-situ ND with XRD data and figure 7.2 shows a TEM image of the $Cu/ZnO/Al_2O_3$ catalyst used in this study. Such catalysts are employed for the industrial synthesis of methanol from syngas ($H_2/CO/CO_2$). While being used today mainly as base chemical and feedstock for chemical industry, methanol has interesting potential as a sustainable synthetic fuel in a future energy scenario [170] if produced from anthropogenic CO_2 and regenerative H_2. The exothermic methanol formation is favoured at low T and high P. In the industrial process is conducted at T = 493-573 K and P = 3.5-10 MPa [171]. The nature of the active sites of $Cu/ZnO/Al_2O_3$ catalysts and of the often observed "Cu-ZnO synergy" has been vividly debated [31]. For instance, a model emphasizing the role of defects found in the active Cu phase after the industrially applied synthesis [8] seems in apparent contradiction to a model focusing on the dynamic interaction of Cu and ZnO leading to dynamic morphology changes of the Cu particles [41, 40, 172]. The latter was related to metal-support interaction and observed on supported model catalysts. Due to the high mobility of Cu according to this model, annealing of structural defects can be expected under working conditions. Based on a structure-activity correlation and DFT calculations, we have recently presented a model for the active site of methanol synthesis that combines both views.[9] Planar defects have been shown to lead to changes in surface faceting of the Cu nanoparticles associated with formation of steps and kinks that represent high energy surface sites of special catalytic activity. For a series of Cu/ZnO-based catalysts a linear correlation of the defect concentration with the intrinsic activity of the exposed Cu surface was observed. In addition, surface decoration [41] of Cu with ZnO_x by strong metal support interaction [34] (SMSI) has been confirmed by HRTEM and in situ-XPS on a high-performance catalyst [9]. Hence, ZnO rather than Cu seems to be the mobile component in course of Cu-ZnO interaction, thus enabling dynamic changes and a static Cu defect structure at the same time. The predominating planar defects in the Cu particles are twin boundaries and stacking faults that can be observed in TEM images (Fig.7.2, b) and quantitatively studied with diffraction techniques. In the present study, an industrial $Cu/ZnO/Al_2O_3$ catalyst with similar properties as the materials presented in ref.[8] has been used for methanol synthesis and its microstructure has been studied under industrial working conditions using in situ ND. A typical syngas mixture was applied at 523 K and 6 MPa in a continuous flow reactor, which was described in detail elsewhere [3]. Catalytic activity studies in the laboratory confirmed stable methanol productivity in the range reported for state-of-the-art $Cu/ZnO/Al_2O_3$ catalysts. During the ND experiment the reaction was in thermodynamic equilibrium. Analogous in situ diffraction studies were carried out in a high-flux experiment with a time resolution of 5 min (ILL, Grenoble, France) [97, 173] and in a high instrumental resolution experiment (Bragg institute, Lucas Heights, Australia).[98] The catalyst was reduced in a D_2 stream in the reactor prior to the catalytic reaction. During the in situ study, methanol was detected at the outlet of the reactor by mass spectrometry. Figure 7.3 shows the high-resolution neutron diffraction patterns of the reduced catalyst in 0.1 MPa Ar at 523 K right before the synthesis and during synthesis under 6 MPa of syngas after 3 and 24 h time-on-stream (TOS). The Rietveld-fit of the fresh catalyst in Ar (Fig. 7.3, top) reveals the presence of fcc-Cu as the

---

[1] Adapted from [5]

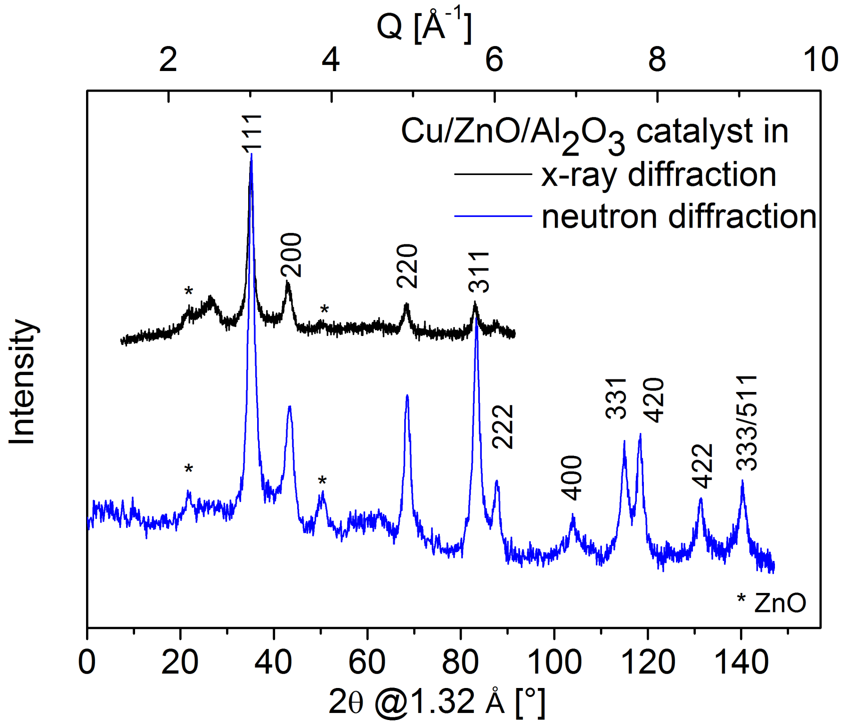

Figure 7.1: Diffraction pattern of the fresh Cu/Zn/Al2O3 catalyst aquried at room temperature with ND (black pattern) and laboratory XRD (Cu K$_\alpha$, grey pattern). Peaks due to Cu are indexed. Due to different wavelengths used, the abscissa is given in reciprocal space.

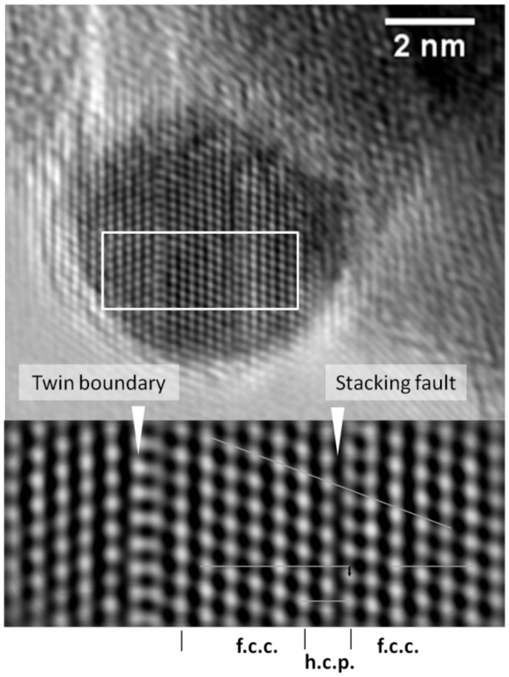

Figure 7.2: High-resolution TEM image of a typical ellipsoidal copper particle in the used catalyst. Planar defects and the resulting thin hcp domain are marked in the close-up.

major phase with a unit cell length of $a = 3.6268$ (± 0.0008) $\AA$ at 523 K (more results of the Rietveld analysis are presented as supporting information). Additional weaker peaks of the catalyst are due to the ZnO component (green profile). No major changes of the Cu phase are obvious from a first comparison of the three ND patterns recorded at different conditions and the lattice parameter of Cu does not vary significantly. Thus, bulk inclusion of C or H species from the gas phase in the Cu lattice of working catalysts can be readily excluded. Only a slight sharpening of the Cu peaks can be detected, which corresponds to an increase in crystalline domain size from 5.9 (± 0.1) nm to 6.4 (± 0.1) nm with time and is due to sintering of the Cu particles.

Planar defects are expected [8, 76, 86] to contribute to the anisotropic broadening of the ND peaks. Line profile analysis turned out to be complex and data analysis suffered from the nanostructured nature of the samples and the in situ conditions (for details see supporting information). However, application of a pattern decomposition method has been shown [9] to allow qualitative confirmation of the presence of stacking faults in the Cu nanoparticles. This evaluation is based on the peak positions, which can be determined with higher precision compared to the other peak profile parameters. An ideal defect-free Cu is expected to show a ratio of the distances between the (111) and (200) lattice planes of $2/\sqrt{3}$=1.1547. The presence of stacking faults causes a shift of the 111 and 200 peaks towards each other and lowers this ratio.[74] Thus, the resulting deviation from cubic symmetry can be used as a measure for the stacking fault probability α, which is calculated according to $\alpha = 8.3 \cdot [(2/\sqrt{3}) - (d_{111}/d_{200})]$ [74]. Figure 7.3 shows the evolution of $\mathrm{d}_{111}/\mathrm{d}_{200}$

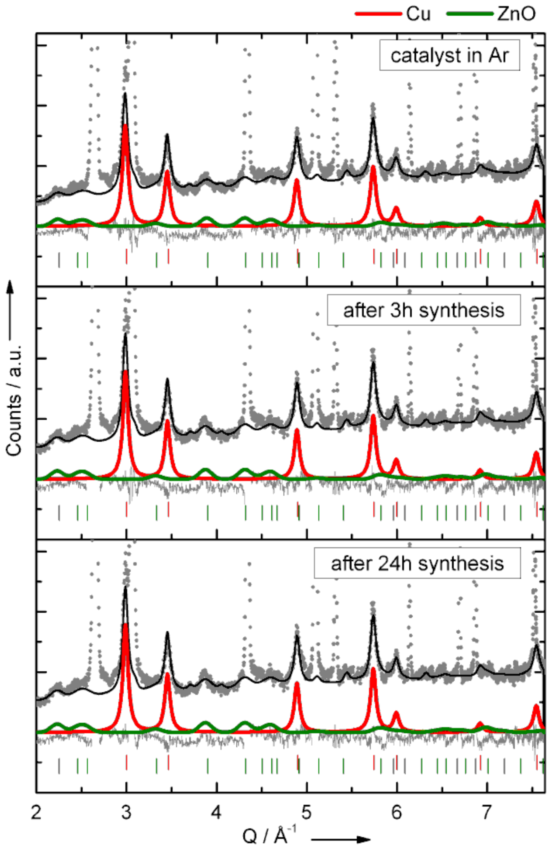

Figure 7.3: Rietveld-fits of the catalyst before (0.1 MPa Ar, upper panel), at the beginning (center) and after 24 hours of methanol synthesis (bottom) at 523 K and 6 MPa. Experimental data is shown in grey, the calculated pattern of the catalyst as black line. The thin grey line is the difference between experimental and calculated pattern. The contribution of the Cu phase and ZnO is marked as red and green lines with tick marks at the positions of Bragg reflections. Additional strong peaks due to the Al reactor wall were treated as peak-phase during Rietveld-analysis and are excluded from the overall calculated profile shown here.

of the Cu catalyst versus TOS during methanol synthesis. Similar values are obtained

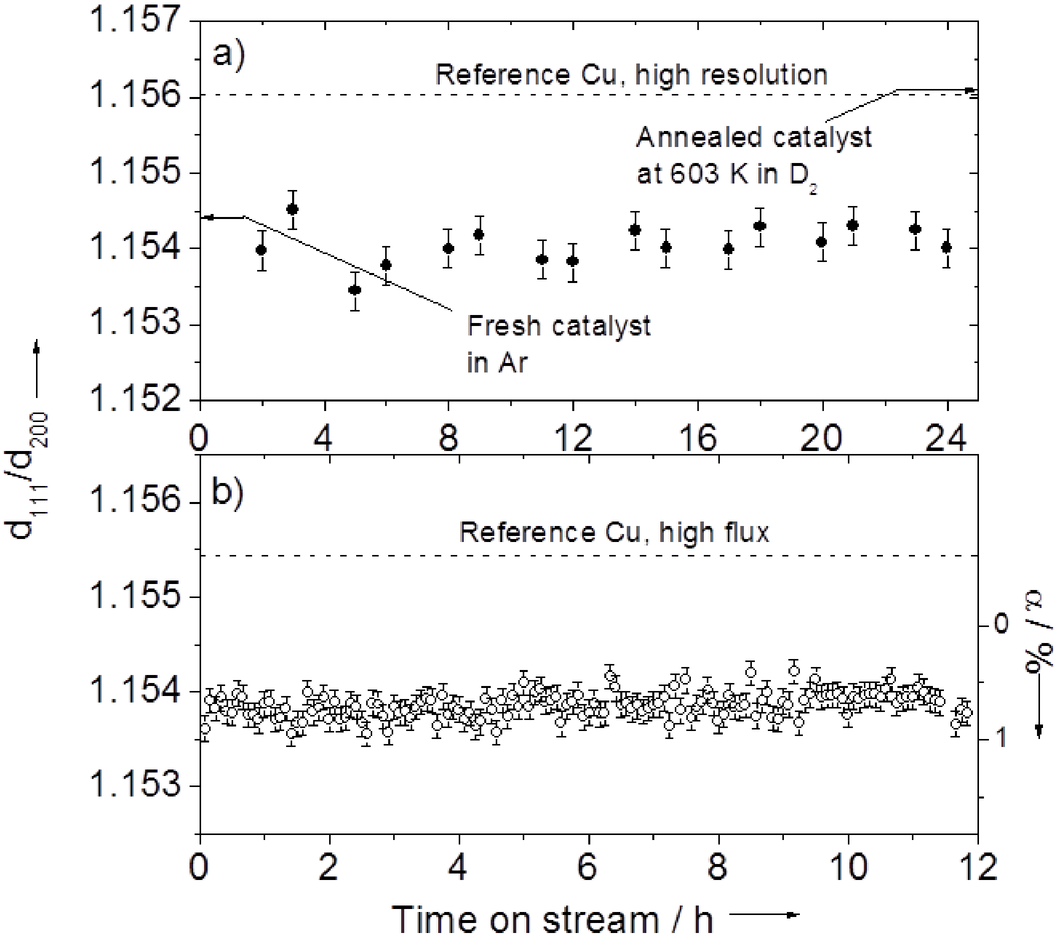

Figure 7.4: d_{111}/d_{200} ratio of Cu in the catalyst and reference sample over TOS during methanol synthesis under industrially relevant conditions in the high resolution- (a) and high flux-experiments (b). This ratio is a measure for the defectiveness of Cu (see text). The formally resulting stacking fault concentration α is shown on the right axis of (b). The error bars are the standard deviations of the two datasets neglecting systematic errors due to, e.g., wavelength and zero-shift.

in both the high-flux and the high-resolution experiments that are significantly lower than that observed for a macrocrystalline Cu reference powder measured in the same reactor tube. It is noted that the experimental values of this defect-poor reference deviate from the theoretical value expected for a perfect fcc lattice in both experiment (cf. right hand axis in Fig. 7.4b). This is attributed to systematic displacement errors of the complex in situ cell at the beamline, which will lead to an offset-like effect in d_{111}/d_{200}. Thus, in contrast to previously reported ex situ ND data, [9] α is evaluated in a semi-quantitatively fashion in this study and only the consistent internal trends observed during the two in

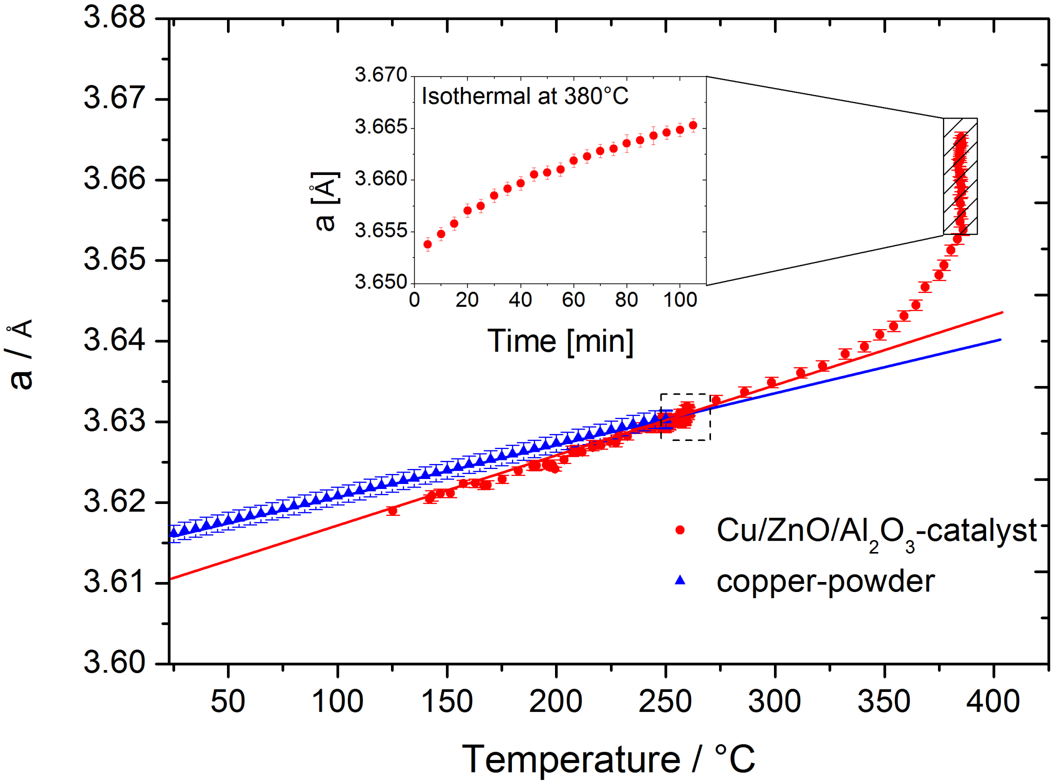

Figure 7.5: Evolution of the lattice parameter of Cu in the Cu/ZnO/Al$_2$O$_3$ catalyst and of the Cu reference powder with temperature. The Cu powder was heated in Ar at 0.1 MPa, while the calcined catalyst was heated to 523 K in D_2 (0.1 MPa), then subjected to 12 hours of methanol synthesis at 523 K in the syngas feed (6 MPa) and finally heated in D_2 (0.1 MPa) to 653 K. Heating rate was 1 K/min and one ND pattern corresponds to ca. 5 K. The dashed square at 523 K marks the period of 12 h synthesis. The right axis shows the lattice expansion relative to the reference at 298 K.

situ experiments are discussed in the following. However, it is noted that the magnitude of deviation between catalyst and reference on the α-scale corresponds to a few %, which is in agreement with previous studies of similar materials [8, 9].
These results confirm that the Cu phase in the active catalyst bears stacking faults. Furthermore, this data proves that the planar defects in the Cu nanoparticles are relatively stable under working conditions and do not disappear when switching from Ar to syngas on a time scale proposed for Cu morphology changes ($<$ 30 min[172]), but resist for 24 hours TOS. Annealing of the defects would lead to an approach toward the reference value, which is in both experiments hardly significant in the investigated time interval. Figure 7.3 reveals that the difference between the catalytically active copper phase and a bulk reference copper material, that has been observed before [8] and ascribed to the peculiar microstructure of the former,[36] is mostly conserved under working conditions. This finding supports the concept of a rather static Cu phase, which maintains its defect structure. In turn, the results suggest that the observed strong interactions between Cu and ZnO [9] manifest themselves rather in form of mobile ZnO_x than mobile Cu in the industrial high performance catalyst. The material under study here exhibits relatively large Cu nanoparticles and poorly crystalline ZnO and the observations are not necessarily in contradiction with previous reports of a mobile Cu phase and static ZnO, which were made on highly crystalline ZnO decorated with very small Cu particles,[41] as such differences might be able to cause to a switch of the mobile component during SMSI-induced dynamics. To study the response of the catalyst to higher T than applied for methanol synthesis, the sample has been heated after the 24 h TOS experiment in D_2 atmosphere to 603 K (high resolution experiment) and 653 K (high-flux experiment). This is beyond the temperature limit of approximately 573 K, which should not be exceeded in methanol synthesis to suppress activity loss due to sintering [32]. At 603 K the Cu crystallites have grown significantly to 9.4 ($\pm$0.2) nm as revealed by ND peak width analysis. At the same time, also the defects have been annealed and α is at the same level as the bulk reference (Fig. 7.3a). The evolution of the Cu lattice parameter over the full T-range is shown in Fig. 7.5 (high flux data). The thermal expansion of the reference Cu powder as well as of the catalyst is linear at $T \leq 523$ K. Interestingly, the lattice parameters at room temperature as well as the thermal expansion coefficient of catalyst and reference differ. The extrapolated Cu lattice parameter is 3.114 ($\pm$ 0.0009) $\mathring{A}$ for the catalysts and thus 0.1% smaller than that of the bulk reference, which corresponds to the literature value. The low value for the catalyst is in agreement with ex situ results[9] and ascribed to the nanostructured nature of the sample. Lattice contraction with decreasing particles size has been observed for many metals.[136, 137] Also different thermal expansion coefficients have been previously observed for nanomaterials compared to their bulk counterparts [174, 175] and are probably influenced by the smaller particle size, the contact to the oxide phase and the presence of defects. It can be seen in Figure 7.4 that the period of methanol synthesis over 12 hours (dashed square) did not lead to any lattice expansion. Thus the beginning formation of α-brass in the bulk of the Cu particles by partial reduction of the ZnO component can be safely excluded during methanol synthesis under industrial conditions. Spencer[42] reported a low diffusion coefficient of zinc in copper at methanol

synthesis condition of 523 K that increased when going to 623 K. Accordingly, brass formation is observed at higher T in D_2 and causes a deviation from the linear behaviour starting at around 603 K. In this T-regime, thermal expansion is superimposed to the lattice expansion due to successive substitution of Cu by larger Zn atoms in the newly formed alloy as is evidenced by the continuing lattice expansion in the isothermal regime at 653 K (Fig. 7.5, inset). Based on the results of Grazzi et al.,[176] the concentration of Zn in the alloy can be estimated to 4.88 (± 0.05) mass-% after 100 minutes of isothermal treatment at 653 K in 0.1 MPa D_2. In summary, the potential of in situ ND to study solid catalysts in a realistic reactor at high pressure conditions that are relevant for applications has been demonstrated for a $Cu/ZnO/Al_2O_3$ methanol synthesis catalyst. The metallic Cu component is nanostructured and highly defective. The deviation from ideal bulk-Cu is manifested in a lattice contraction at room temperature and an increased thermal expansion coefficient. In addition, a high concentration of stacking faults has been detected in the Cu nanoparticles, which were proved to be stable under working conditions. The bulk inclusion of reactive species from the gas phase as well as the formation of brass during methanol synthesis can be excluded. The latter alloying was observed only at significantly higher T. Under reaction conditions, the non-ideal nature of Cu was found to be relatively stable in industrial catalysts. Future work using this methodology will aim at correlation of the described structural properties with catalytic performance and include information about the evolution of the microstructure with deactivation of the catalyst over a longer TOS.

Experimental Section

The catalyst was provided by Clariant Produkte (Deutschland) GmbH. The methanol synthesis reaction was done at 523 K and 6 MPa in thermodynamic equilibrium with a syngas mixture (CO_2:CO:D_2:Ar = 8:6:75:6) in a flow cell described previously.[3] Diffraction experiments were carried out on D1B (ILL, Grenoble, F)[97] and on ECHIDNA (ANSTO, Lucas Heights, AUS).[98] Sieve fractions of the catalyst and the polycrystalline Cu reference (99,8%, Heraeus) were used (200-300 μm). Rietveld refinement was done with the Topas 4.2 software. Multiple peak fitting during pattern decomposition was carried out with OriginPro 8.5 peak analyzer. For more experimental details, please refer to the supporting information.

Chapter 8

Structure and phase composition of an operational ammonia catalyst

Ammonia synthesis is one of the largest processes in chemical industries. It was first operated at BASF one hundred years ago based on the fundamental work of Fritz Haber[177] and process engineering by Carl Bosch. Haber combined feed gas recycling with application of high pressure (P = 200 bar) and a Ruthenium catalyst to achieve sufficiently high conversions of nitrogen according to $N_2 + 3\ H_2 \rightleftarrows 2\ NH_3$. This success enabled the large scale production of artificial fertilizers, which was a prerequisite to face the worlds increase in population and is known as the extraction of bread from air - a term that was coined later by Max von Laue.
Today, contrary to the generation of syngas for ammonia, only little has changed in the industrial process for the actual synthesis of ammonia[178].The process is operated at typical temperatures of 500 °C and pressures around 200 bar, resulting in ammonia concentrations in the exhaust gas of up to 17 vol.%. Approximately 80% of the worldwide ammonia output of 136 Mtons[12] (2011) is used for the production of fertilizers. A key development for the modern Haber-Bosch process, however, has been the catalyst development at BASF that was led by Alwin Mittasch in the early 20th century. After testing 22 000 different formulations in a gigantic effort, the work was concluded in 1922 with the identification of a very unique catalyst synthesis [103]. To achieve a highly active iron catalyst, magnetite, Fe_3O_4, was promoted by fusing it together with irreducible oxides (K_2O, Al_2O_3, later also CaO) in an oxide melt at temperatures around 1000 °C. The fused magnetite is mechanically granulated and its reduction need to be conducted with great care in the syngas feed to finally give the active α-Fe catalyst[179]. This special synthesis leads to certain crucial properties of the resulting α-Fe phase, which is commonly termed “ammonia iron”. In addition to its outstanding economic relevance, ammonia synthesis acts as a “drosophila reaction” for catalysis research and has always been a test case for the maturity of catalysis science in the context of a technologically mature application. Today, due to the enormous efforts in surface science, physical and theoretical chemistry, and chemical engineering a consistent picture of the reaction mechanism and the role of the Fe catalyst and its promoters has emerged. Key contributions to the modern understanding of the ammonia synthesis reac-

tions came from the teams lead by Gerhard Ertl [59, 51], Michel Boudart [180, 16], Gabor Somorjai [55], Haldor Topsøe [181] and Jens K. Nørskov [182, 183], just to mention a few. However, even after 100 years of application and research there still is scientific interest in the Haber-Bosch process, mainly because of two aspects. Firstly, catalysts with improved low-temperature activity, higher specific surface area and higher tolerance against poisons and on-off operations are generally desirable. Also the development of a more elegant synthesis route for the Fe-based catalyst without the melting step and the extremely critical activation procedure could foster the potential application of ammonia as an energy storage molecule [184]. Secondly, there still is a gap between the model studies conducted with well-defined simplified materials with clean surfaces at low pressures to elaborate the current knowledge of ammonia synthesis and the industrial process. These so-called pressure and materials gaps often prevent straightforward extrapolation of model studies to real industrial processes. Thus, the question of a dynamical change of the catalyst under true reaction conditions remains to be studied and calls for in situ experimentation.

This point requires special attention in case of the ammonia synthesis over iron catalysts, because it is well known and has been studied for decades in the context of steel hardening [185, 186, 187, 188, 189, 190] and catalytic ammonia decomposition [191] that iron can be easily nitrided by ammonia. Ertl and co-workers described the reaction mechanism of ammonia synthesis [51, 52]. He and other authors showed that the reaction is structure sensitive [53, 59, 55, 192]. The dissociative chemisorption of di-nitrogen on the iron surface is the rate limiting step in ammonia synthesis [59] and opens possibilities for sub-surface diffusion of the atomic nitrogen [55]. Ertl et al. proposed the surface dissolution of nitrogen into iron forming a surface nitride of the approximate composition Fe_2N and the presence of in-situ formed metastable γ-Fe_4N [59] Thus, for experimental conditions remote from the Haber-Bosch process, participation of stoichiometric bulk nitrides like FeN has been excluded. Instead, Herzog et al. proposed formation of subnitrides of the type $Fe_{10-20}N$ based on a diffraction study on an industrial material, but at ambient pressure [56].

The partial pressure of ammonia p_{NH_3} determines the thermodynamical nitriding ability of the gas stream and the formed phases [185]. In the Haber-Bosch process, p_{NH_3} is high due to the high total pressure and the relatively high product concentration. The ammonia decomposition reaction furthermore provides a "virtual" pressure of atomic nitrogen [61, 60], which is higher than the corresponding hydrostatic pressure due to the easier formation of atomic nitrogen from the product ammonia compared to reactant di-nitrogen [57]. According to the Lehrer-Diagram [185] the existence of metastable γ- or ϵ-FeN is thermodynamically expected at the virtual ammonia pressures of the Haber-Bosch process. The discrimination of these stoichiometric bulk iron nitrides from N-free α-Fe by diffraction is straightforward, as they have different crystal structures, beginning with bcc α-Fe containing up to 0.4 at.% N, over fcc γ-Fe with a maximum solubility of 20 at.% N, followed by hcp ϵ-Fe_xN, with a N solubility between 15 and 33 at.% [189]. Owing to the elastic coherent scattering length of N for thermal neutrons (9.36 fm), which is almost as high as Fe (9.45 fm)[84], an increasing number of N atoms in the Fe-host lattice contribute to a higher scattering intensity in neutron diffraction. However, the (reversible) formation of FeN in ammonia synthesis was so far not directly observed, which might be related to the lack of experimental methods that are suitable for these demanding conditions. Thus, the in situ-nitriding of the ammonia synthesis catalysts has been debated in the literature [193, 56, 194]. Herein, we report in situ neutron diffraction data obtained on an industrial catalyst under conditions much closer to the Haber-Bosch process to answer the question of a dynamical bulk nitridation of the ammonia synthesis catalyst. This method and the experimental setup used have been recently shown to enable direct in situ observation of the bulk structural properties of working catalysts [3, 5]. Here, ammonia synthesis was conducted on an industrial catalysts provided by BASF in a tubular fixed bed reactor made of a Nickel alloy at conditions given by the safety limits of 425 °C and 90 bar. Syngas (N_2:D_2, 1:3) was fed through the catalyst bed at a low space velocity to approach thermodynamic equilibrium of the ammonia synthesis reaction corresponding to a product concentration of 14.7 vol.% NH3 (measured: 12.6 vol.%). The experiment was performed at the SPODI beamline [195] of the FRM-II neutron research reactor in Munich, Germany. The reactor walls and the catalyst bed were penetrated by the neutron beam during the experiment and high resolution neutron diffraction data was recorded. According to the Lehrer-diagram, the conditions are sufficient for formation of the γ-phase of iron nitrides. At 425 °C and 75 bar the transition from the α-phase to γ happens at 0.9 vol.% NH_3 for pure iron, while the ϵ-phase is expected at 7.6 vol.% NH3. In addition to the ammonia synthesis conditions, milder conditions were applied before and after the reaction to check for reversible changes.

In figure 8.1, the neutron diffraction pattern of the post-reaction industrial catalyst is compared to two reference materials, commercial iron (α-Fe) and iron nitride ($Fe_{2-4}N$). The commercial iron nitride has been prepared from iron by nitridation with ammonia and quenching. In the pattern of this reference sample, the γ-Fe_4N_{1-y} (63 wt.%), ϵ-$Fe_3N_{1.245}$ (24 wt.%) and ϵ-Fe_3N_1 (13 wt.%) phases of iron nitride can be identified. As seen from the comparison and confirmed by Rietveld refinement, all peaks of the Fe phase in the catalysts can be explained by the presence of α-Fe, and a phase transformation induced by nitridation leading to a stable bulk iron nitride can be excluded.

To check for the possibility of a reversible formation of a metastable Fe-N phase during operation, as expected from the phase diagram, the patterns of the activated catalyst in the pre-reaction state, the in situ pattern recorded at a self-generated ammonia concentration of 12.6 vol.% as the post reaction state are compared in Figure 8.2. In addition to the peaks of the metallic iron, a faint contribution of an additional magnetite phase (Fe_3O_4) phase was observed in the pre-reaction catalyst. The presence of magnetite is a consequence of the kinetic difficulty to fully reduce the catalyst and single-crystalline magnetite particles are proposed to act as spacers to prevent the metallic Fe-platelets from sintering [82]. However, the crystalline magnetite readily disappeared at TOS=26 h in the operational catalyst probably due to the higher reducing potential of the syngas at 75 bar and 425 °C and the catalyst is found to be in a strongly reduced state [57].

It is evident from Figure 8.2 that no in situ transformation into metastable bulk nitrides has taken place due to inclusion of nitrogen atoms from the formed ammonia despite the high p_{NH_3}. Like the post-reaction state (Figure 8.1), the catalyst in working condition can be described to a first approximation by a single α-Fe phase. We can, thus, safely

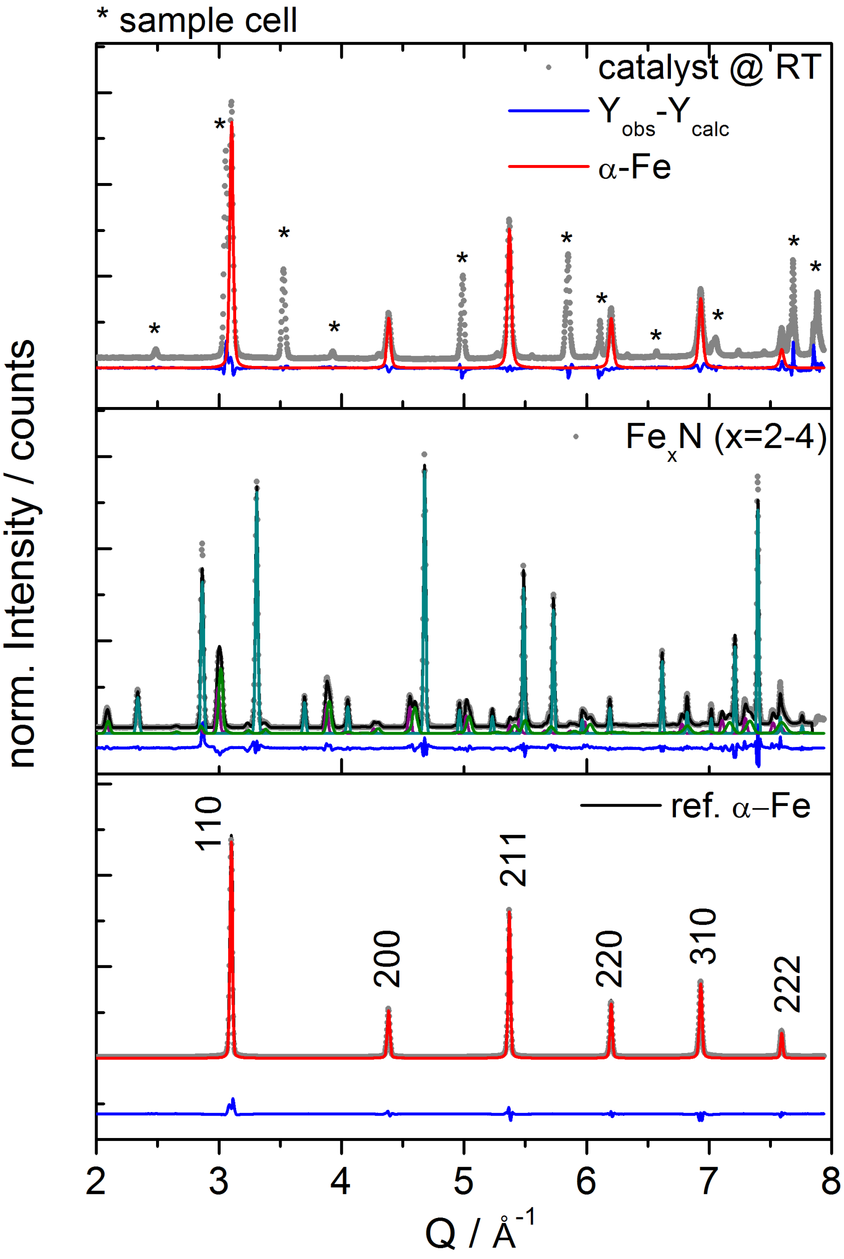

Figure 8.1: Neutron diffraction pattern of commercial iron powder (bottom, red) and iron nitride (middle, black, $Fe_{2-4}N$) and the post-reaction industrial ammonia synthesis catalyst at room temperature (top). Rietveld refinement revealed the presence of α-Fe (red profile) and peaks due to the reactor cell walls (marked).

conclude that the virtual pressure of nitrogen during the experiment was not sufficient for nitriding of the entire bulk, because no peaks of the $Fe_{2-4}N$ reference pattern (Fig. 8.1) were observed at any time. Such phases were recently described [190] and are commonly observed in Fe-based catalysts for ammonia decomposition. In the following, we address the microstructure of the stable α-Fe phase in the catalysts in comparison with the reference material and its evolution under reaction conditions. In comparison with the α-Fe reference, the peak profiles of the catalyst are significantly broadened as seen in Figure 8.3 indicating a difference in the microstructure of both materials. Also the intensity ratio of the α-Fe peaks differs for the reference (100:23:68:27:37:13, expected for ideal α-Fe: 100:24:64:25:43:15 [196] and the catalyst (100:21:57:23:30:16, pre-reaction state) with a stronger 110 and 222 in the latter. At the same time, an anisotropic peak broadening of the 110 and 310 profiles was observed (see supporting information). These observations clearly indicate a microstructural and textural effect of the preparation and activation process and/or additives on the catalyst. In addition, it can be seen in the inset of Figure 8.2 that the peak profiles of the catalyst are not fully satisfactorily described by the Rietveld fit, which is another indication that points to presence of deviations from the ideal structure [197].

Earlier studies revealed that the activated ammonia catalyst shows a strongly hierarchical microstructure [198, 199, 78]. Anisotropic Fe platelets have been observed in the surface near region [57]. Therefore, the deviation of the catalysts peak intensities and breadths from the α-Fe powder reference [4] can be explained as 'structural anisotropy' of the ammonia-iron caused by defects, size and strain effects [10, 200, 201] (a short discussion of line profile effects of defects in α-Fe is given in the supporting information). It seems likely that the unexpected stability of the α-Fe in the catalyst is related to these microstructural effects.

While the difference between catalyst and reference was obvious, it was surprising to see hardly any changes in the peak shapes of the catalyst upon changing the conditions (Fig. 8.2, 8.3 a)). This observation strikingly confirms the stability not only of the iron bulk against nitridation, but also of the catalysts peculiar microstructure. Neither thermal annealing of defects, nor any reversible or irreversible dependence of the catalysts structural features on p_{NH_3} could be found. It turned out that the variation of the peak breadth between the reduced and pre-reaction state is explained by a faint reduction of the apparent α-Fe domain size upon further heating and reduction under syngas by c.a. 5 nm to 26 nm ± 5 nm at TOS=0h. As a function of TOS, an increase of averaged, apparent domain size is observed, up to a value of 32 nm ± 7 nm for the operational catalyst at TOS=88h during coincidental increase of the mean residual strain (MRS) by 0.03%. The persistency of the lattice parameter of the α-Fe with 288.43 pm over the entire operational period obviates any restructuration of the host structure. The diffusion-controlled cooled post-reaction catalyst under Ar exhibits the largest domain size (36 nm $\pm$ 8 nm) and as well the highest MRS with 0.24% of the sample series. Interestingly, its lattice parameter (286.79 pm) does not differ tremendously from reference α-Fe at the same temperature (286.78 pm). These trends in the series of samples observed by Rietveld refinement were confirmed by model-free line profile analysis by Williamson-Hall method (details see Sup-

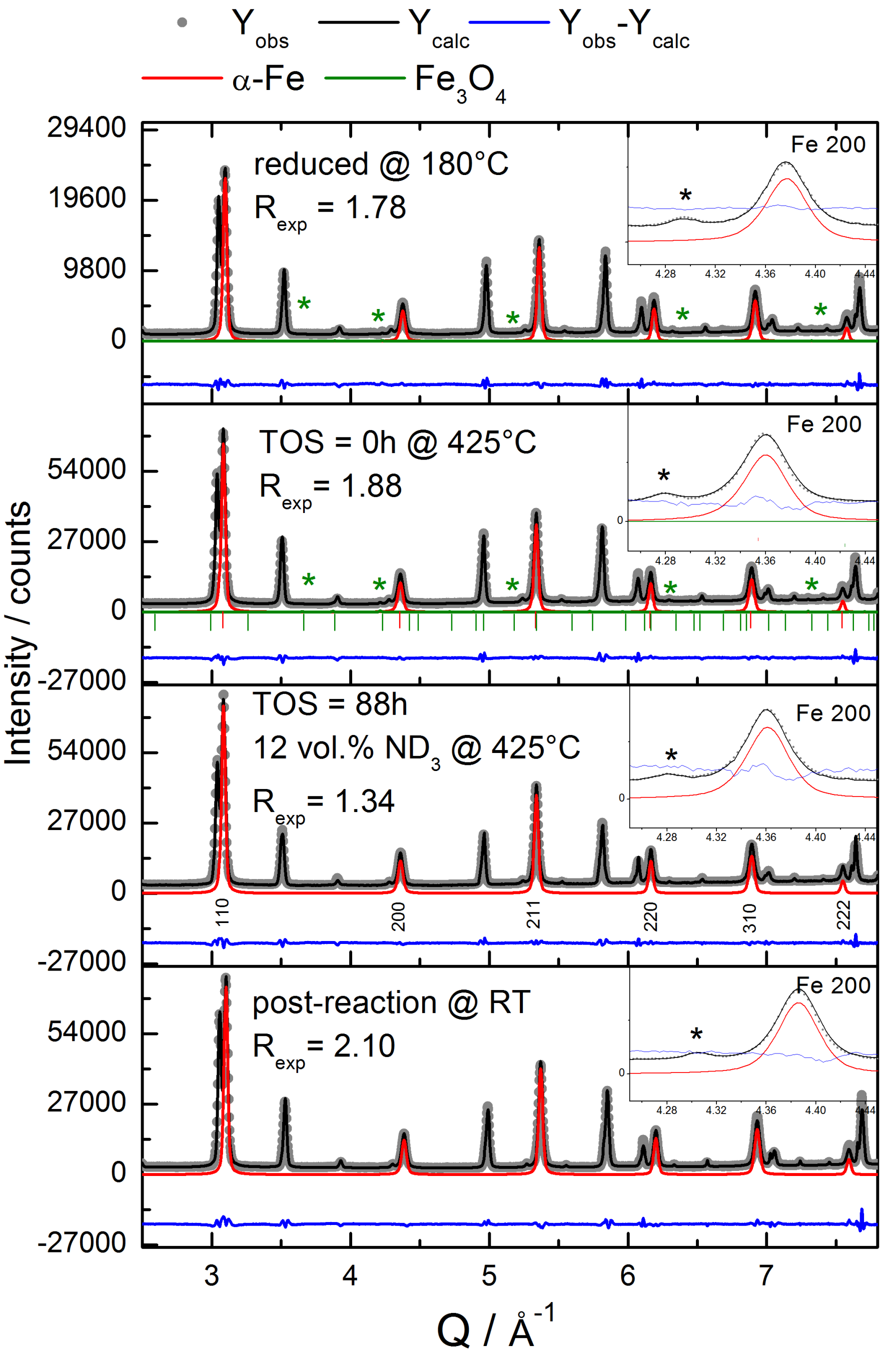

Figure 8.2: Neutron diffraction patterns of the ammonia synthesis catalysts at different conditions. The solid red line indicates the fitted contribution α-Fe phase to the patterns. a) reduced, initial catalyst in 5 bar D_2 at 180 °C (the olive line is the profile of magnetite, peaks additionally marked by asterisks); b) pre-reaction catalyst at 425 °C under 75 bar syngas at TOS=0h; c) in-situ reaction state at 425 °C under 75 bar syngas, which is converted to yield 12 vol.% ND_3 at TOS=88 h d) post-reaction catalyst in 75 bar Ar at room temperature. The insets show the magnification of the 200 peak of α-Fe, wherein the black asterisks marks the contribution from the Ni-reactor tube.

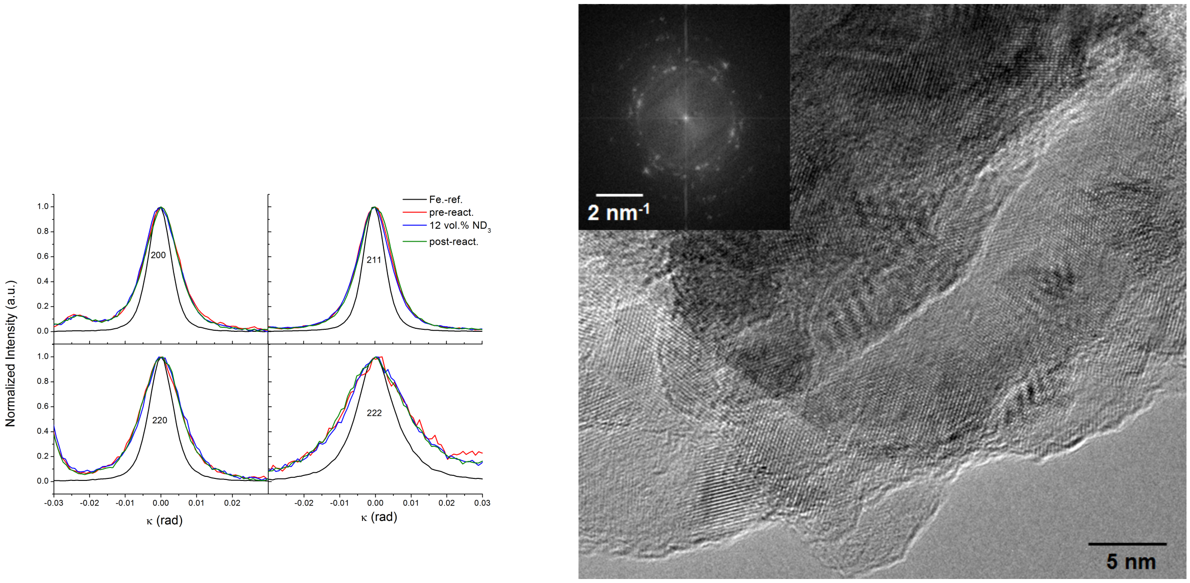

(a) (b)

Figure 8.3: a) Normalized peaks profiles of the 200 (right, top), 211 (left, top), 220 (right, bottom) and 222 (left, bottom) of the catalysts a-Fe reflections. The thermal shift from 28 °C (reference-iron, black and post-reaction state, green) to 180 °C (pre-reaction state) and 425 °C (12 vol.% ND_3) was compensated by normalizing to the peak maxima on the x-axis. b) Representative HRTEM micrograph of the post-reaction ammonia catalyst. The inset in the upper left corner shows the power spectrum of the TEM image. The interference in the outer region of the iron lattice is assigned to a tetragonal inclusion into the host lattice.

plementary Information). Taking the determined lattice parameters at RT, 180 °C and 330 °C (from earlier measurements [4]) into account, the linear thermal expansion coefficient can be determined. The determined value for the temperature regime (26 °C to 330 °C) of 11.9×10^{-6} K^{-1} ±0.2% is in good agreement with the given literature value of 11.8×10^{-6} K^{-1} [47]. Ridley and Stuart state, that the true coefficient for pure α-Fe increases almost linear to just above 550 °C [80]. With respect to that, the measured lattice constant of the catalyst under reaction conditions at 425 °C is 0.1% larger than expected for this temperature. The most probable explanation for the variation in d-spacing, which is consistent with the literature view on the active catalyst is the presence of endotactic chemical impurities [181, 57], expressed in a fashion of incorporation of individual molecules of hercynite into the lattice of the α-Fe host lattice. The phenomenon of the replacement of seven iron atoms by one hercynite molecule was named paracrystallinity by Hosemann et al. [81] (detailed information in SI). The consequence of the replacement of the iron atoms is expressed in elastic deformations in the vicinity of the hercynite molecule due to differences in the molecular structure compared to the host structure, which results in a higher lattice constant of the α-Fe lattice [14].

While the measured apparent domain size at TOS=0h with 26 nm ±5 nm confirms the values of earlier measurements [14, 106], it remains open, if the observed variation in the peak breadth over TOS is really a consequence of increasing apparent domain size or either a contribution from non-statistical distributed, anisotropic strained diffraction planes in the domain resulting due to hercynite incorporation, which is expressed in an increase of paracrystallinity over TOS by almost 1.1% (c.f. SI).

Regarding the lattice parameter of the subsequently fully reduced minority magnetite phase (840.9 pm at 180 °C and 843.8 pm at 425 °C), a solid solution of alumina and the magnetite of the type $Fe_{3-x}Al_xO_4$ [106] can be excluded due to a very high concordance to reference values given in literature ($\tilde{8}$40.6 pm at 180 °C and $\tilde{8}$43.4 pm at 425 °C [107]).

Conclusively it is claimed, that the presence of strain in varying amounts over entire TOS is indicating that the proposed lattice distortion has formed already as a result of catalyst activation, probably with other atoms in the interstitials of the iron lattice. It is noted that refined phase content of the magnetite is below 1.4 wt.% and thus close to the detection limit for minor phases, in particular if these are crystallographical related to the main phase like in this case.

We, however, note that the interpretation of the above results is consistent with the literature view on the active catalyst. The unnitridated α-Fe still clearly is the major phase of the catalyst. Thus nitrogen dissolution may be limited to a small fraction of the catalyst and we tentatively locate these domains in the surface near region of the larger iron particles (d 100 nm [4]) leading to a situation that can be described as a Fe-N surface phase (0.8-0.96 monolayers [53, 202]) supported on a core of unaffected α-Fe, which dominates the diffraction pattern. This picture is in agreement with the model that the bulk α-Fe provides the skeleton for a surface Fe-species, which is supposed to play the crucial role in the catalytic process [56, 57, 82, 83]. Because hardly any reversible structural change was observed, our diffraction results encourage post-reaction high resolution TEM (HRTEM) studies of the near surface region. A representative HRTEM image of the post-reaction catalyst is given in Figure 8.3b.

An anisotropic, platelet-like morphology of the iron particles was observed. The lattice spacings are due to the α-Fe phase and the crystalline domains, in agreement with the diffraction analysis, exhibit sizes of a few nanometers. In conclusion, this work has provided experimental evidence that validates the understanding obtained on iron surfaces from surface science in low-pressure experimentation and theoretical model approaches for the industrial ammonia synthesis reaction. No major dynamic phase changes due to nitridation have been observed on an industrial ammonia synthesis catalyst when subjected to a self-generated NH_3 concentration of 12.6 % at 75 bar and 425 °C , i.e. close to the conditions in the Haber-Bosch process. The stability of the α-Fe phase in the catalyst was not expected based on the thermodynamics of pure iron at such NH_3 partial pressures. In comparison to reference Fe, the industrial catalyst shows a complex and defective microstructure that was inherited from the preparation and activation processes. Also this unique microstructure was stable and hardly any structural healing was observed during operation. The absence of nitridation is thus not due to the general absence of a gap between low and high pressure, but can be rather explained due to the cancellation of the expected pressure effect by the materials effect. While the former thermodynamically favors bulk nitridation, the latter kinetically stabilizes the defective α-Fe phase likely a result of the presence of additives and of the preparation history of Mittaschs synthesis. The complex real structure of this catalyst after activation and its stability appears to be a prerequisite for high performance and should be target of any alternative synthesis approaches for ammonia synthesis catalysts aiming at a simpler and more elegant preparation.

Experimental Section

A BASF S6-10 catalyst was carefully reduced and dried. 17.1703 g of the reduced catalyst were transferred via an Ar-glovebox into the flow cell for the neutron experiment and sealed air-tight. The experiment was carried out on high-resolution thermal neutron diffractometer SPODI [195] at the research reactor Heinz Maier-Leibnitz (FRM II) of the Technical University Munich in Garching, Germany. For the in-situ studies a modified version of a continuous flow-cell was used, which was already described elsewhere [3]. At the beamline, the pre-reduced catalyst was activated by heating up slowly from RT to 180 °C with a heating rate of 1 Kpm in a D_2 stream of 9.6 l/h at 4.4 bar. Further heating to reaction state was done under 75 bar D_2/N_2/Ar-Syngas (72:23:6) with a rate of 0.5 Kpm to 425 °C . The reaction slowly approached a steady state concentration of ND_3 of 12.6 vol.% after 88 h TOS, which is close to equilibrium. The catalyst bed temperature as well as reaction pressure were monitored by an in-bed-thermocouple and pressure gages at reactor inlet and outlet. The gas-phase composition and flow were monitored with a Pfeiffer-Thermostar mass-spectrometer and film-flow-meters. For each reaction state, pre-reaction, in-situ (TOS=88 h) and post-reaction, 3 diffraction pattern (each 30 min) were acquired and the ND_3 yield was determined by bubbling the exhaust stream through water and subsequent titration. Analysis of the patterns was carried out by Rietveld-refinement. Further details of the experiment can be found as supporting information.

Appendix A

Mathematical appendix for data evaluation

A.1 Analytical determination of instrumental broadening (IRF)

As it is crucial for analytical profile fitting routines to determine H_{pv} -or more precisely β_{pV}- at every certain point along entire range of the diffraction profile, an accurate determination of instrumental broadening is a prerequisite. Assuming pseudo-Voigt peak shape, initial peak parameters (Q_0, H and η) which are needed for accurate structural analysis could be achieved by any fitting routines which support the pseudo-voigt peak function. The data obtained in this study was decomposed and analyzed by Xfit-Koalariet [130] and Origin 8.5.1.

The shape parameter η, which is the exact description of the analytical profile can be obtained by the fitting of the reflection profiles of a suitable reference compound. From η, the full width at half maximum (FWHM) H_{pV} of the pseudo-Voigt peak is related to the individual Lorentzian (H_L) and Gaussian (H_G) FWHM components. Thompson et al. gave a numerical approximation which relates (H_L, H_G) and (H, η) via the expressions [203]:

$$\frac{H_L}{H_{pV}} = 0.72928\eta + 0.19289\eta^2 + 0.07783\eta^3 \tag{A.1}$$

and

$$\frac{H_G}{H_{pV}} = \left(1 - 0.74417\eta - 0.24781\eta^2 - 0.00810\eta^3\right)^{1/2} \tag{A.2}$$

The integral breadth β_{pV}, which was used along this study to model IRF and create classical Williamson-Hall-Plots, is the ratio between integral intensiy and amplitude, given by the relation:

$$\beta_{pV} = \frac{\pi H_{pV}/2}{\eta + (1-\eta)\left[\pi(ln2)\right]^{1/2}} \; . \tag{A.3}$$

The integral breadths of Lorentzian and Gaussian components are converted from the FWHM's of the corresponding components according to [143]:

$$\beta_L = \frac{\pi}{2} H_L \quad \text{and} \quad \beta_G = \frac{1}{2}(\pi/ln2)^{1/2} H_G \; . \tag{A.4}$$

In Rietvelds [77] original approach to model the IRF of a low-resolution neutron diffractometer, it was assumed that for the range between Q_{min} and Q_{max} the shape parameter of the pseudo-Voigt function, η, strictly follows a linear trend

$$\eta = a + b\theta. \tag{A.5}$$

In a first approximation, the description of the IRF by Eq. 5 and Eq. 6 is sufficient when the instrument can be considered only as an arrangement in horizontal geometry, which is causing primary Gaussian broadening [125, 77]. While on high resolution neutron diffractometers there is a considerable axial beam divergence [127], this effects results in an additional Lorentzian broadening. As a consequence, Eq. 6 was enhanced to account for that fact by a Lorentzian term (Eq. 7)[126, 87].

$$H_G = \sqrt{Utan^2\theta + Vtan\theta + W + P/cos^2\theta} \tag{A.6}$$

and

$$H_L = \frac{X}{cos\theta} + Ytan\theta + Z \tag{A.7}$$

The graphical interpretations of the numerical results of Eqs. 6 and 7 are depicted in Fig.A.1 for the neutron diffractometer and Fig. A.2 for the X-ray diffractometer. It should be pointed out, that the numerical values for U,V,W,P and X, Y, Z have no significant physical meaning, as their are only used to achive the best possible fit for the IRF.

A.2 Deconvolution of instrumental contribution [1]

The measured experimental pattern I_{Q_m} is a convolution of the interference function I_Q given by the scattering vector Q of the crystal lattice and the instrument function gQ. The convolution integral given by

$$I_{Q_m} = \int_{-\infty}^{+\infty} I_{Q-Q_i} g(Q_i) dQ_i \tag{A.8}$$

---

[1] The following paragraphs are adapted from [6] and [7]

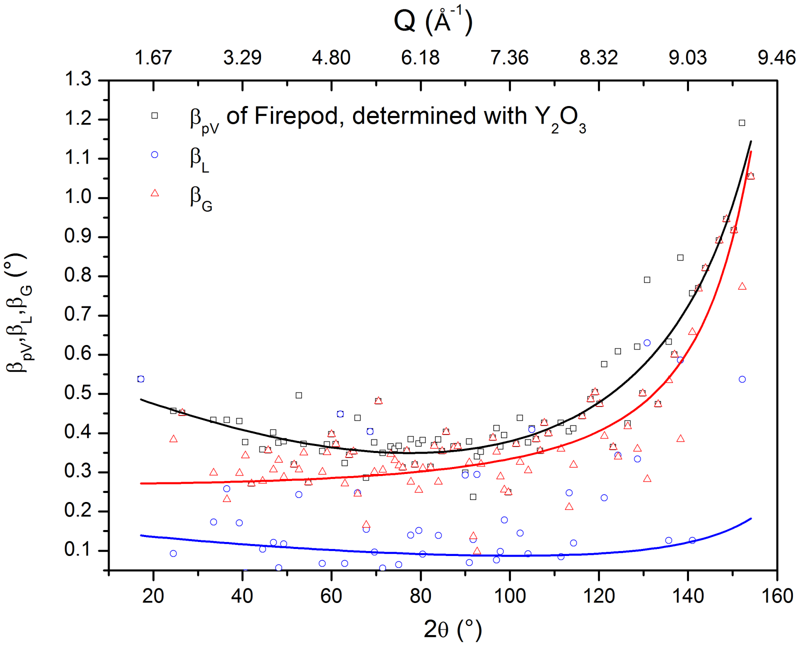

Figure A.1: IRF of the fine resolution powder diffractometer (Firepod, E9) at the research reactor BER II at Helmholtz-Centre Berlin in the former configuration [127] with Y_2O_3.

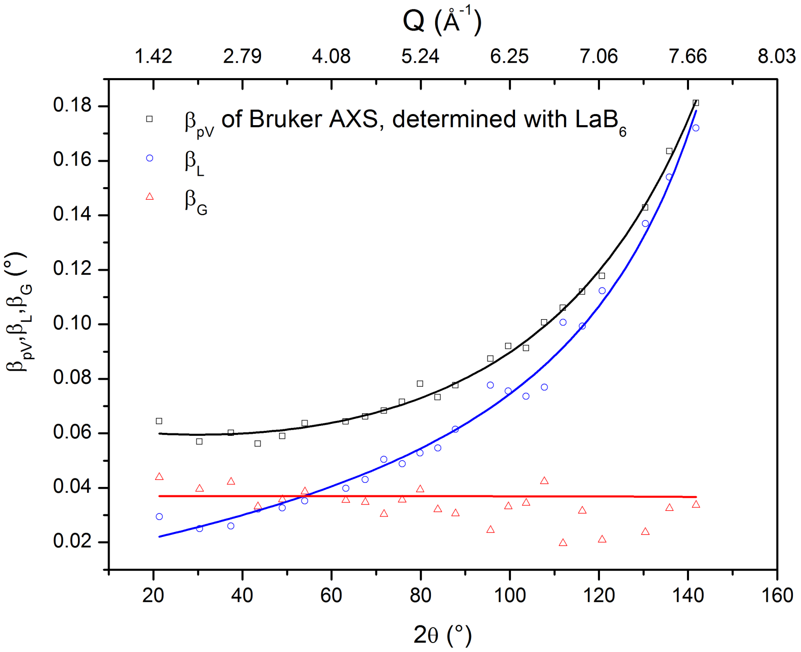

Figure A.2: IRF of the X-ray diffractometer (Bruker D8 Advance) in Bragg-Brentano geometry, determined with LaB_6.

By setting the expressions for the measured experimental pattern $I_{Q_m} = h(Q)$ and the pure structural interference function $I_Q = f(Q)$ one achieves

$$h_Q = \int_{-\infty}^{+\infty} f_{Q-Q_i} g(Q_i) dQ_i \tag{A.9}$$

$$= (f * g)(Q) \tag{A.10}$$

As it is assumed, that the Fourier-transformation of a convolution of two functions is equal to the product of the Fourier-transform of each factor, it follows

$$\frac{1}{\sqrt{2\pi}} \int_{-\infty}^{+\infty} (f * g)(Q) exp(iQL) dQ = \sqrt{2\pi} F(L) G(L) \tag{A.11}$$

wherein F(L) and G(L) are the Fourier-transformations of f(Q) and g(Q). While the scattering vector Q is a reciprocal unit, it represents the information depth in the scattering material, the so called column length L. Therefore, each constituent $h(Q)$, $f(Q)$ and $g(Q)$ of the pattern could be expressed as a Fourier-series of the type

$$h(Q) = \int H(L) exp(-2\pi iQL) dQ \tag{A.12}$$

$$f(Q) = \int F(L) exp(-2\pi iQL) dQ \tag{A.13}$$

$$g(Q) = \int G(L) exp(-2\pi iQL) dQ \tag{A.14}$$

As each peak of $h(Q)$ and $g(Q)$ used for the correction has a discrete data-point in Q in the observed range, for a given peak-center Q_0 the probing intervals (Q_n) are given as $n = 0, 1, 2, 3, ...N$. Therefore, Eqs. A.14 can be written in the analytical form [6]

$$h(Q) = \sum_{n=-N/2}^{N/2} H(L_n) exp(-2\pi iQL_n) dQ \tag{A.15}$$

$$f(Q) = \sum_{n=-N/2}^{N/2} F(L_n) exp(-2\pi iQL_n) dQ \tag{A.16}$$

$$g(Q) = \sum_{n=-N/2}^{N/2} G(L_n) exp(-2\pi iQL_n) dQ; . \tag{A.17}$$

The correction for instrumental broadening is carried out by complex division according to:

$$F(L) = \frac{H(L)}{G(L)} \tag{A.18}$$

By back-transformation of $f(Q)$, I_Q can be achieved.

A.3 Fourier coefficients and Fourier-synthesis

It is supposed, that the instrument-corrected scattering signal, implicit in Eqs. A.6 and A.8 can be expressed as a Fourier-series of the type

$$f(Q) \;=\; \frac{a_0}{2} + \sum_{m=0}^{\infty} (a_m \cos mQ + b_m \sin mQ) \tag{A.19}$$

where the Fourier coefficients a_m and b_m are terms like domain size, dislocations, anti-phase domains and faulting, which contribute to the broadening of the scattering peak. By applying a manual least-squares fitting procedure to the broadened peaks one gets an analytical function $f'(Q)$ which can be used to determine Fourier coefficients according to

$$a_n \;=\; \frac{1}{\pi} \int_{-\pi}^{\pi} f'(x) \cos nx \, dx \quad (n = 0,\, 1,\, 2,\, \ldots) \tag{A.20}$$

and

$$b_n \;=\; \frac{1}{\pi} \int_{-\pi}^{\pi} f'(x) \sin nx \, dx \quad (n = 1,\, 2,\, 3,\, \ldots) \tag{A.21}$$

Since the sine is an odd function, the coefficient b_n becomes zero, if the curve is considered as symmetric (e.g. pseudo-Voigt, Gauss).

Appendix B

Used program codes

B.1 Instrument resolution determination by Origin

The following fitting-routine was developed in OriginC, to determine instrumental resolution parameters according to ”Caglioti” directly from XFit results of LaB_6 or Y_2O_3 with FWHM and 2θ-values.

```
#include <origin.h>
void _nlsfCagliotti(
// Fit Parameter(s):
double U, double V, double W, double P, double X, double Y, double Z,
// Independent Variable(s):
double x,
// Dependent Variable(s):
double& y)
{
  // Beginning of editable part
  y=sqrt(U*tan(((x/2)*(PI/180)))^2+V*tan(((x/2)*(PI/180)))+W+P/cos(((x/2)*(
      PI/180)))^2)+X/cos(((x/2)*(PI/180)))+Y*tan(((x/2)*(PI/180)))+Z

}
// Curve(s)
Curve x_y_curve,
// Auxilary error code:
int& nErr)
{
  // initialize parameters

  get_exponent (x_data, y_data, NULL, &A);

  // End of editable part
```

B.2 Stacking fault simulation using DIFFAX

The following code was used to calculate diffraction intensities from Cu-catalysts, that contain coherent stacking faults. DIFFaX (v 1.812) was written by Michael M. J. Treacy in Fortran. The stacking faults appear in a infinity crystal in {111}-plane of hexagonal-packing. The stacking fault probability (α) is considered to by 1%. According to previous Rietveld-refinements, B_{iso} is considered to be 0.2. The pV-mixing parameter μ is assumed to be constant over the 2θ-range from 10-175°. The minimum increment is $\Delta 2\theta = 0.01$.

```
{data file for copper, with random hexagonal intergrowths}
{probability of cubic stacking = 90%}
{cubic stacking sequence = 111111111.... or 222222222...}
{Hexagonal staking sequence = 1212121212121212....}

INSTRUMENTAL                              {Header for instrumental section}
NEUTRON                                    {Simulate neutron diffraction}
1.307666                                   {Neutron wavelength}
{gaussian 0.1 trim}                       {Instrumental broadening (much faster)}
PSEUDO-VOIGT 0.04844 0.0 0.3133 0.2186 TRIM {Instrumental broadening (
    Caglioti)}

STRUCTURAL                                {Header for structural section}
2.5560 2.5560 2.0869 120.0                {unit cell coordinates, a, b, c, gamma}
UNKNOWN                                   {hexagonal, c = cubic [111]}
2                                         {111 sheet, plus its mirror}
infinite                                  {Layers are very wide in the a-b plane}

LAYER 1
CENTROSYMMETRIC
Cu    1   0.0   0.0   0.0   0.2   1.0

LAYER 2 = 1             {Layer 1 is isostructural to layer 2 and viceversa}

STACKING                                {Header for stacking description}
recursive                               {Statistical ensemble}
infinite                                {Infinite number of layers}

TRANSITIONS                             {Header for stacking transition data}
{Transitions from layer 1}
0.001    1/3    2/3   1.0     {layer 1 to layer 1}
0.999   2/3    1/3   1.0     {layer 1 to layer 2}

{Transitions from layer 2}
0.001    1/3    2/3   1.0     {layer 2 to layer 1}
0.999   2/3    1/3   1.0     {layer 2 to layer 2}
```

B.3 Fourier-synthesis using PM2K

The following code was used in PM2K (written by Matteo Leoni) to refine an unaged Cu-sample with partly diffraction-amorphous ZnO. Instrument resolution, log-normal size distribution, stacking faults (2D) and line defects (1D) were included into the convolution. The Background is afterwards added to the convoluted intensity and modelled by a 6th order Chebyshev-polynomial.

```
// load the input data and associate it to the WPPM model
loadData(”2-7088-LC.xy”, WPPM())
// enable output of results as a .fit file
enableFileFit()

// add spectral components
addWavelength(0.1307666, 1)

// define the lattice (for cerium oxide)
addPhase(aCu 3.609803e-001, aCu, aCu, 90, 90, 90)
// start definition of broadening contributions
par !W 3.2373e-001, !V 0, !U 3.6410e-002
//   Parameters for eta (a + b th + c th^2)
par !a 5.995e-002, !b  4.75e-003, !c -2.30176e-005
convolveFourier(CagliotiUVWabc(U, V, W, a, b, c))
convolveFourier(SizeDistribution(”sphere”,”lognormal”, mu 1.427031e+000,
    sigma 4.985432e-001 max 30 min 0))
par !Dave:=exp(mu+sigma^2/2); /*(arithmetic) mean size*/
par !sd:=sqrt(exp(2*mu+sigma^2)*(exp(sigma^2)-1)); /*standard deviation*/
splitPeaks(”fcc”)
convolveFourier(FaultingWarren(alp 3.679448e-003, bet 7.412676e-002))
convolveFourier(Wilkens(rho -8.971250e-003,Re -1.768587e+000,
    0.304602,-0.500211,0.298341,-0.708806, !mix 0.5,burgers := aCu*sqrt(2)
    /2;))
// add the peaks
addPeak( 1,  1,  1 , @ 7.707255e+001)
addPeak( 2,  0,  0 , @ 4.792527e+001)
addPeak( 2,  2,  0 , @ 1.247087e+002)
addPeak( 3,  1,  1 , @ 2.799106e+002)
addPeak( 2,  2,  2 , @ 9.597580e+001)
addPeak( 4,  0,  0 , @ 8.903351e+001)
addPeak( 3,  3,  1 , @ 2.638652e+002)
addPeak( 4,  2,  0 , @ 2.440246e+002)
addPeak( 4,  2,  2 , @ 1.471154e+002)
addPeak( 3,  3,  3 , Int333 4.079655e+001)
addPeak( 5,  1,  1 , @ :=Int333*3.044;)
// add diffractometer misalignment and specimen displacement
// 2theta shift contributions
//shift(SpecimenDisplacement(185, @ -3.252060e-002))
shift(ZeroError(@ 3.173666e-002))
//shift(LaB6tancorrection(ax -5.761528e-002,bx 2.048272e-001,cx -8.616463e
    -001,0))
// consider Lorentz-Polarization correction
```

```
mul(LPFactorSecondary(0,0))
// add the phase background
add(Chebyshev(@ 1.071614e+003,@ 3.128031e+001,@ -3.826774e-001,@ 1.612235e
    -003,@ -2.253188e-006))
```

Appendix C

Reactor construction

C.1 Fatigue crack analysis and materials database

The materials used for the construction of the ammonia and methanol synthesis reactor had to be assessed regarding their long term stability. The numerical values of the yield strength as a function of temperature were gained by suppliers specifications or specific publications (references see text). In a first attempt, the applicable pressure onto the tube was estimated by von Mieses yield criterion.
Generally assuming, that a non-reversible deformation or failure of an object is a consequence of exceeding the ultimate yield strength (σ_v) of a material -also named the von Mises criterion-, three principle stress coordinates (tensors) are contributing. In a simple uniaxial stress situation or tension, the problem is one-dimesional and therefore reduced to axial strain (σ_l). In the case of plain stress (e.g. compression) Mises criterion becomes planar, described by circumferential strain (σ_u^2). Applying pressure (e.g.inner wall of a tube) yields additionally into radial strain (σ_r). Therefore, the so called yield surface is sum of all tensors, where each of the tensors must be smaller then the ultimate yield strength:

$$\sigma_v = \frac{1}{\sqrt{2}} \cdot \sqrt{(\sigma_u - \sigma_l)^2 + (\sigma_l - \sigma_r)^2 + (\sigma_r - \sigma_u)^2} \tag{C.1}$$

As from Hook's law known, any material is elongated proportional to applied uniaxial tension. Hook's law, simply speaking, collapses at the end of the linear elangation process with materials failure the so called ultimate tensile strength, R_{eH}. To present materials from total failure, the applicable load limit = ultimate yield strength is set to a limit, were a maximum permanent deformation of 0.2% is recognized. Therefore, the relation between $\sigma_{0.2}$ and $Rp_{0.2}$ can be described as:

$$\sigma_v = \frac{R_{eH}}{\nu_N} \tag{C.2}$$

$$\sigma_{0.2} = Rp_{0.2} \tag{C.3}$$

wherein ν_N is a specific weakening coefficient of junctions in the material, typically 1-0.85. For the geometry of a pressurized (p) tube, with a given inner diameter (d_i) and a wall

Nimonic 80 A, W. Nr. 2.4952

Temperature	Tors. modulus	Dyn. Young's mod.	$Rp_{0.2}$	Specific heat	LTE
°C	kN/mm^2	kN/mm^2	N/mm^2	J/Kg°C	$10^{-6}/°C$
20	85	219	570	448	12.8
100	84	216	550	469	12.8
200	82	210	530	494	13.3
300	79	204	500	519	13.7
400	77	197	475	548	14.1
500	74	191	475	573	14.5
600	70	183	475	599	15
700	67	175	450	628	15.5

Table C.1: Mechanical properties of Nimonic alloy 80A. Heat treated 8 h at 1080°C and air cooled for 16 h at 700°C, cooled to RT by air(Values taken from Special Metals).

thickness (s), σ_l, σ_u and σ_r are given by:

$$\sigma_l = p\frac{d_i}{(4s)} \tag{C.4}$$

$$\sigma_u = \frac{p}{2}\left(\frac{d_i}{s} - 1\right) \tag{C.5}$$

$$\sigma_r = \frac{-p}{2} \tag{C.6}$$

For a given applied pressure, wall thickness is calculated according:

$$s_{0.2} = \frac{d_i \cdot p}{(2\sigma_{0.2} - p) \cdot \nu_N + 2p} \tag{C.7}$$

The maximum applicable pressure for a given wall thickness is calculated therefore by:

$$p_{0.2} = \frac{s \cdot 2\sigma_{0.2} \cdot \nu_N}{d_i + (s \cdot \nu_N)}. \tag{C.8}$$

For the calculation of applicable fatigue crack load, $\sigma_{0.2}$ is replaced by σ_v. Following tables depict the used values for $Rp_{0.2}$ used for design and calculation of the reactors. Nimonic is a heat-durable, age-hardenable Ni-Cr alloy, strengthened by additions of Ti, Al and C for temperatures up to 815°C, which was used for the construction of the ammonia-reactor. The $AlMg_3$-alloy was used for low-temperature applications, due to it's no-gamma-emission property, like e.g. methanol synthesis.

C.2 Construction drafts for ammonia reactor

The following construction drafts show the assembled reactor body and flow cell of the reactor used for ammonia synthesis. For technical details referring to the methanol reactor c.f. to Chapter 4.

AlMg3, W. Nr. 3.3535

Temperature	Tors. modulus	Dyn. Young's mod.	Rp$_{0.2}$	Specific heat	LTE
°C	kN/mm^2	kN/mm^2	N/mm^2	J/Kg°C	10^{-6}/°C
20	70	n.d.	82	n.d.	23.8
100	70	n.d.	82	n.d.	23.8
200	n.d.	n.d.	80	n.d.	n.d.
300	n.d.	n.d.	73	n.d.	n.d.
400	n.d.	n.d.	41	n.d.	n.d.
500	n.d.	n.d.	36	n.d.	n.d.

Table C.2: Mechanical properties of aluminium alloy AlMg3 (Values taken from [94].

SS 316L, W. Nr. 1.4401

Temperature	Tors. modulus	Dyn. Young's mod.	Rp$_{0.2}$	Specific heat	LTE
°C	kN/mm^2	kN/mm^2	N/mm^2	J/Kg°C	10^{-6}/°C
20	n.d.	200	600	500	16.5
100	n.d.	194	582	n.d.	16.5
200	n.d.	186	561	n.d.	17.5
300	n.d.	179	536	n.d.	17.5
400	n.d.	172	508	n.d.	18.5
500	n.d.	165	484	n.d.	18.5
600	n.d.	n.d.	≤300 n.d.	n.d.	

Table C.3: Mechanical properties of stainless steel alloy 316L (Values taken from Swagelok).

SS 304, W. Nr. 1.4301

Temperature	Tors. modulus	Dyn. Young's mod.	Rp$_{0.2}$	Specific heat	LTE
°C	kN/mm^2	kN/mm^2	N/mm^2	J/Kg°C	10^{-6}/°C
20	n.d.	200	230	500	16
100	n.d.	194	157	n.d.	16
200	n.d.	186	127	n.d.	17
300	n.d.	179	110	n.d.	17
400	n.d.	172	98	n.d.	18
500	n.d.	165	92	n.d.	18
600	n.d.	n.d.	90	n.d.	n.d.

Table C.4: Mechanical properties of stainless steel alloy 304 (Values taken from Matweb online-resource).

REVISION HISTORY

REV	DESCRIPTION	DATE	APPROVED

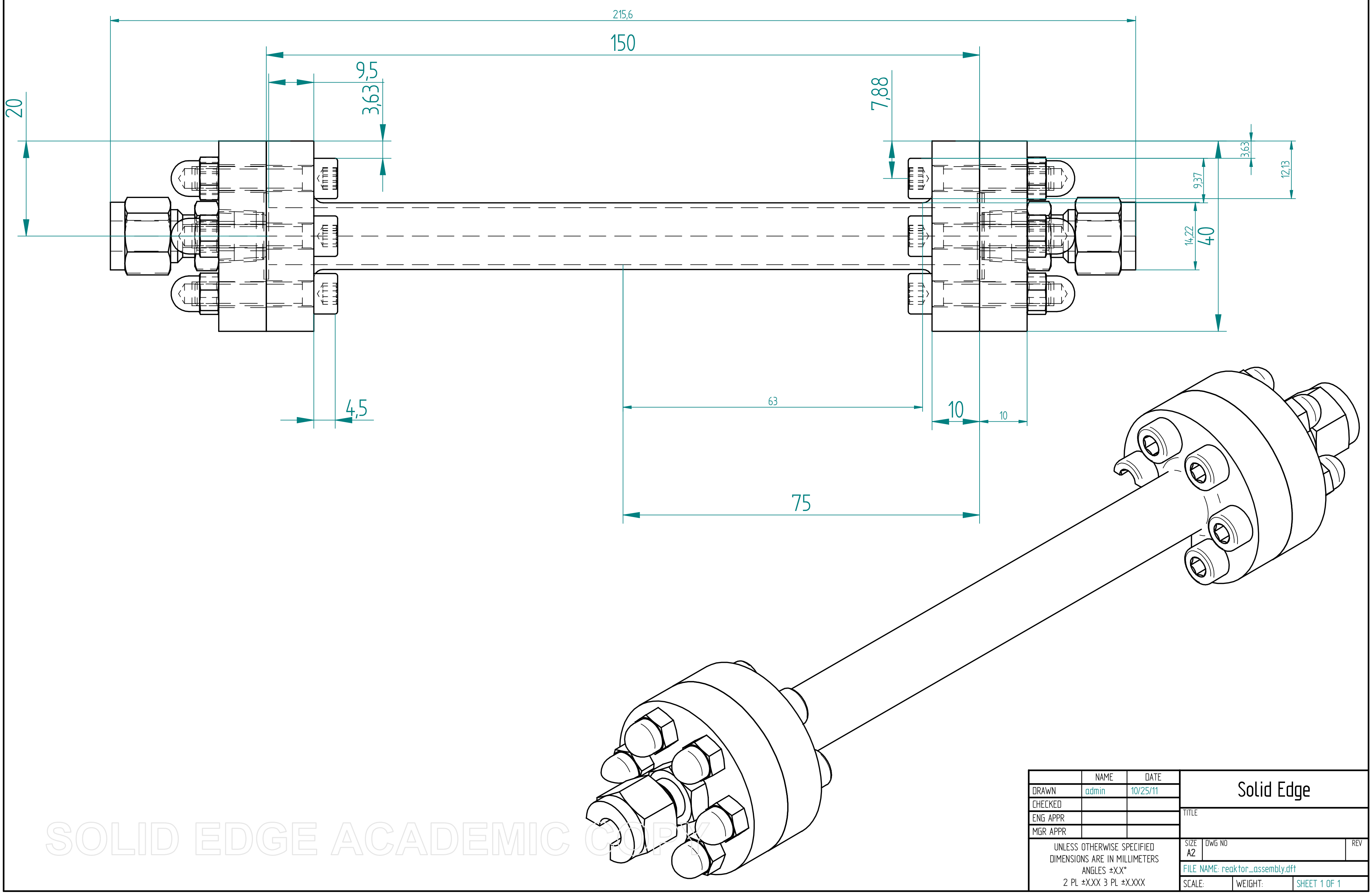
215,6
150
9,5
3,63
20
7,88
3,63
12,13
9,37
14,22
40
4,5
63
10
10
75

SOLID EDGE ACADEMIC COPY

	NAME	DATE
DRAWN	admin	10/25/11
CHECKED		
ENG APPR		
MGR APPR		

UNLESS OTHERWISE SPECIFIED
DIMENSIONS ARE IN MILLIMETERS
ANGLES ±X.X°
2 PL ±X.XX 3 PL ±X.XXX

Solid Edge

TITLE

SIZE A2
DWG NO
REV

FILE NAME: reaktor_assembly.dft

SCALE:
WEIGHT:
SHEET 1 OF 1

REVISION HISTORY			
REV	DESCRIPTION	DATE	APPROVED

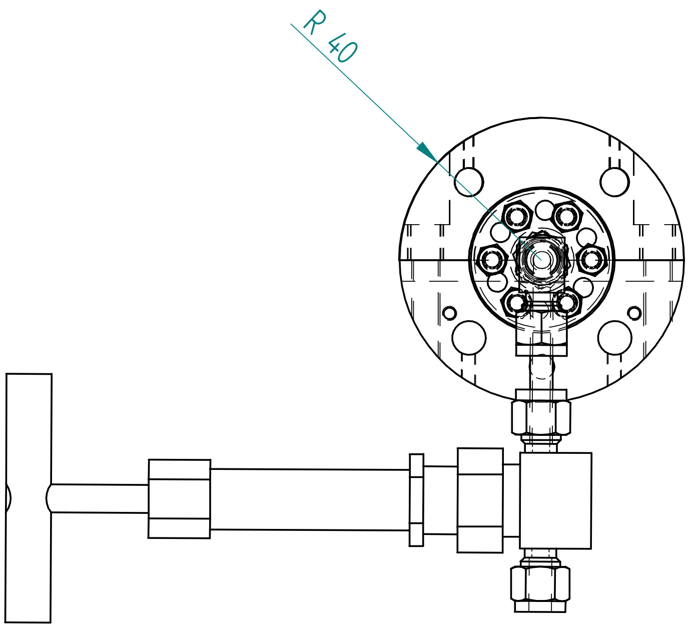

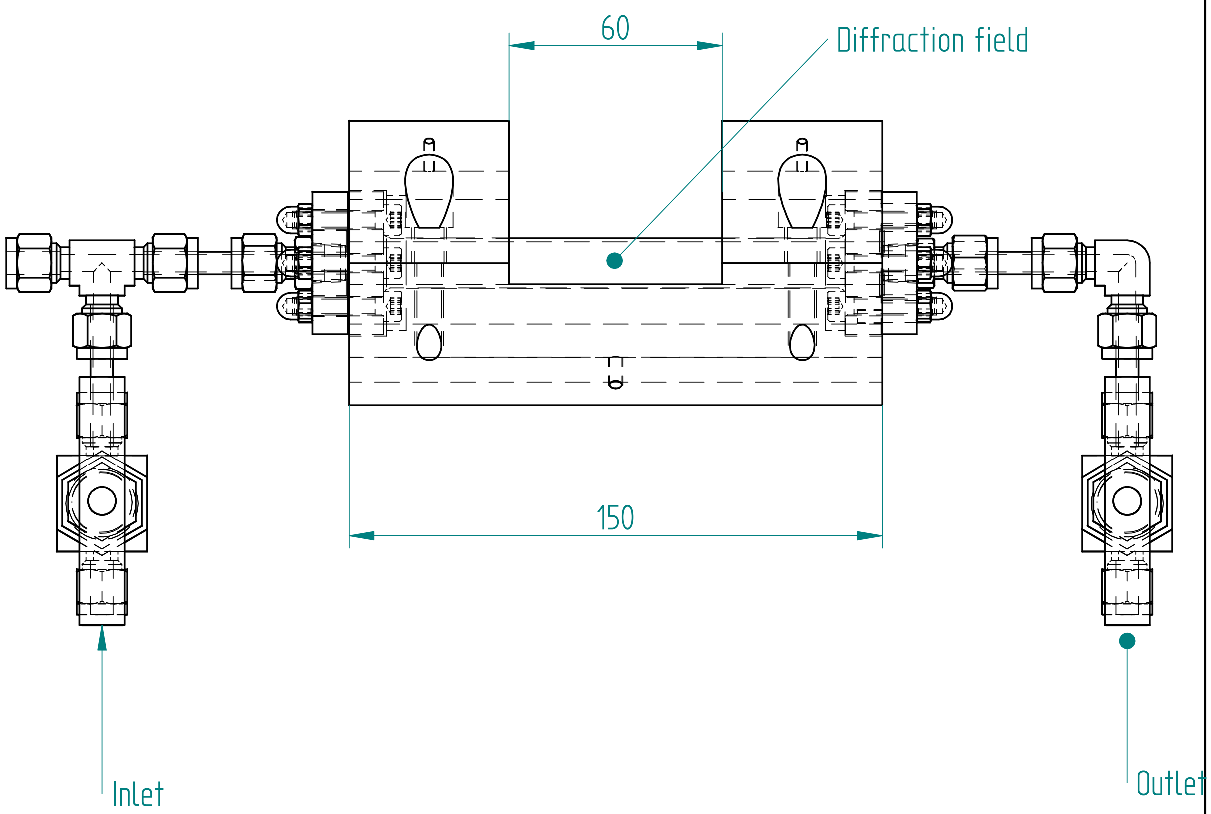
60
Diffraction field
150
Inlet
Outlet

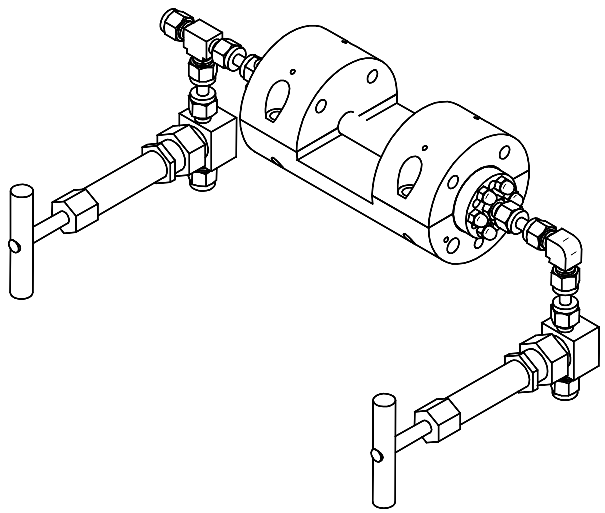

Specification of operation parameters:
110 bar @ 100°C
100 bar @ 300°C
95 bar @ >400°C
90 bar @ >600°C

SOLID EDGE ACADEMIC COPY

	NAME	DATE
DRAWN	admin	01/01/01
CHECKED		
ENG APPR		
MGR APPR		

UNLESS OTHERWISE SPECIFIED
DIMENSIONS ARE IN MILLIMETERS
ANGLES ±X.X°
2 PL ±X.XX 3 PL ±X.XXX

Solid Edge

TITLE

SIZE A2
DWG NO
REV
FILE NAME: Draft2
SCALE:
WEIGHT:
SHEET 1 OF 1

Appendix D

Supplementary information to Chapter 8

D.1 Further experimental details

A commercial iron catalyst (BASF S6-10) consisting mainly of fused iron oxides was reduced under atmospheric pressure for 17 days, by heating slowly up in a 100 ml/min H2 stream with 1 Kpm to 433 K and holding it at this temperature for two days to allow the catalyst to dry. After drying, the catalyst was heated up further with 0.05 Kpm to 733 K, where it was kept under steady conditions to allow reduction. This treatment is an important prerequisite to obtain the active form of the industrial catalyst, which is ascribed to the formation of a highly ordered, epitactic platelet structure of the active catalyst by diffusion controlled processes [57]. After the reduction procedure 17.1703 g of the catalyst were transferred via an Ar-glovebox into the flow cell for the neutron experiment and sealed air-tight. At the beamline, the pre-reduced catalyst was activated by heating up slowly from RT to 180°C with a heating rate of 1 Kpm in a D_2 stream of 9.6 l/h at 4.4 bar. Further heating to reaction state was done under 70 bar D_2/N_2-Syngas with a rate of 0.5 °C to 425 °C.

Reaction setup For the in-situ studies a modified version of a continuous flow-cell was used, which was already described in literature [3]. In contrast to studies carried out earlier, a reactor tube made of a Nickel-based alloy, seal-able by flanges with soft-iron gaskets was used. The high-temperature alloy used had an excellent corrosion resistivity against gaseous ammonia at elevated temperatures, as well as a high tensile yield strength, which allows reduction of the wall thickness to 1 mm to achieve a lower background signal. Precautions were taken to reduce pore-diffusion and heat transfer effects by using a catalyst sieve fraction in the range between 250 μm and 355 μm. However, the ratio of bed length to bed diameter was optimized rather with respect to the neutron beam geometry than for optimal flow condictions. The powder density of the catalyst sieve fraction was approx. 1.95 g cm^{-3} and a uniform packing density of the fixed bed reactor could not be easily achieved, which might have caused deviations from the idealized plug flow model [14]. A longitudinal temperature gradient in the catalyst bed in the range of $\Delta\ T$=12 K was measured as a result of the open furnace geometry for proper neutron diffraction pattern acquisition.

In-situ neutron diffraction As feedgas a mixture of 23 vol.% N_2 (5.0), 6 vol.% Ar (5.0) and 72 vol.% D_2 (2.8) was used. Purging of the lines was done with Ar (6.0). In spite of the usage of high-purity feedgas, an additional guard-reactor operated at 220 °C and loaded with a mixture of reduced S6-10 and pre-reduced high-purity iron-powder was introduced for conditioning of the syngas to avoid oxygen-poisoning of the catalyst.
Initially, a first pattern was acquired at 180 °C under D_2 at 4.4 bar, to catch the initial "freshly"-reduced, pre-reaction state. This pattern is used along this study as a reference state to compare with the post-reaction pattern and patterns recorded under increasing ammonia production rate. Afterwards the feed was switched to syngas and the pressure was increased to 70 bar, while the gas flow was kept constant at 9.6 l/h. Heating to reaction conditions was done under syngas feed with a rate of 0.5 Kpm to 425 °C. When the final reaction temperature was reached, pressure was increased to 75 bar. At this stage a pattern of the TOS=0 h catalyst was acquired. The gas phase composition was monitored by Mass-spectrometry at all times, while a quantitative ammonia determination was performed by titration experiments every 8 hours. Significant amounts of ammonia during this conditioning phase were only detected after 25.5 h of synthesis with 0.63% in the exhaust indicating a slow formation of the active catalyst. The reaction slowly approached a steady state concentration of ND_3 of 12.6 vol.% after 88 h TOS. For each reaction state, pre-reaction, in-situ (TOS=88 h) and post-reaction, 3 diffraction pattern (each 30 min) were acquired and the ND_3 yield was determined by titration.

Data acquisition and analysis The in-situ experiment was carried out on high-resolution thermal neutron diffractometer SPODI at the research reactor Heinz Maier-Leibnitz (FRM II) of the Technical University Munich in Garching, Germany. Its large monochromator take-off angle of 155 ° with a monochromator-sample distance of 5 m allow a sufficient neutron flux of 1×10^6 n cm^{-2} s^{-1} at a wavelength of λ=0.15481 nm [195], dedicated for in-situ studies. The implemented data reduction routine for the intensity integration along the Debye-Scherrer cones from the array of 80 vertical position sensitive ^{3}He detectors allows the acquisition of patterns with a typical step width of $\Delta(2\theta) = 0.05°$ [195], while the typical acquisition time per pattern was 30 minutes. As *alpha*-Fe shows ferromagnetic properties below the Curie-temperature (T_c) of 770 °C [47], the crystallographic and magnetic unit cell overlap, therefore not additional peaks are expected due to magnetism [204]. The catalyst bed temperature as well as reaction pressure were monitored by an in-bed-thermocouple and pressure gages at reactor inlet and outlet. The gas-phase composition and flow were monitored at all times with a Pfeiffer-Thermostar mass-spectrometer and film-flow-meters.
Analysis of the pattern was carried out by Rietveld-refinement of representative patterns

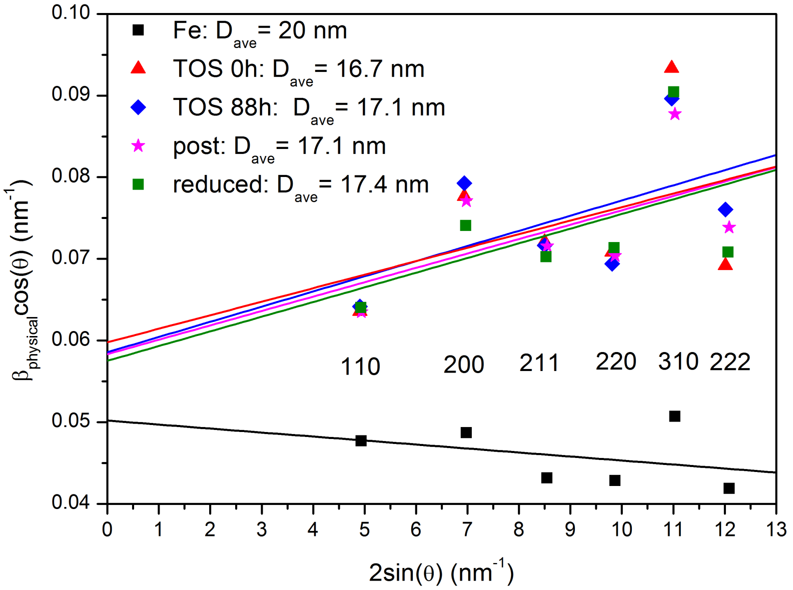

Figure D.1: Williamson-Hall plot from the single peak fit of the reduced, TOS=0h, TOS=88h, post-reaction catalyst and Fe-reference

before and after ammonia-synthesis, as well as for several in-situ pattern, while the corresponding ammonia production rate was determined by bubbling the exhaust gas for 1 h through a solution of 250 ml millipore water and subsequent titration of an aliquot of 15 ml with 0.1 mol l^{-1} HCl over the acquisition time of the pattern.

D.2 Line profile analysis by Williamson-Hall method

Size-strain analysis was carried out by WilliamsonHall method. Therefore the results of the single-peak fitting procedure were subtracted by the influence of the instrumental broadening (for details about the method ref. [197]). The resulting integral breadth is plotted as following: The negative slope for the iron sample is indicating anisotropy due to stacking faults and twin boundaries. The excessive amounts of defects in the Fe-reference can be explained with respect to the preparation history of the sample by ball milling [201]. Furthermore, the domain size of the macrocrystalline material is suspected to larger than 100 nm, which is the size limitation of Williamson-Hall analysis and the Scherrer-formula, which is used to determine the apparent crystal size, respectively.

List of Figures

1.1 Thermodynamic equilibrium yield calculation for different temperatures as function of pressure for methanol synthesis from syngas containing 8 vol.% CO_2, 6 vol.% CO and H_2 in balance. 5

1.2 Thermodynamic equilibrium yield calculation for different temperatures as function of pressure for ammonia synthesis from a syngas composition of 1:3 N_2 to H_2. 5

3.1 Scattering length b for thermal neutrons as function of the atomic number, numerical values taken from [84]. 16

3.2 Coherent, incoherent and total scattering cross sections σ for thermal neutrons as function of the atomic number [84]. 18

4.1 Process flow chart of operating reactor including gas supply and effluent analytics. The system is kept under high pressure until the back pressure regulator (BPR). Gas analytics is carried out under ambient pressure. . . . 27

4.2 Assembled flow cell inserted into the reactor body. 30

4.3 Reduction procedure of a commercial Cu/ZnO/Al_2O_3 catalyst. Normalized integrated intensities of the CuO(11-1) and Cu(111) peaks correlated with the catalyst bed temperatur (top) and effluent gas composition (bottom) during isobar reduction from 301 K to 523 K in D_2 feed. Missing ion-current between 130 min and 140 min is devoted to a artefact. 34

4.4 Rietveld refined neutron powder diffraction pattern of a working commercial Cu/ZnO/Al_2O_3 catalyst under syngas at 523 K and 6 MPa. 35

5.1 Flow reactor mounted on the Echidna instrument. The incident neutron-beam window is shown in the background. 38

5.2 Neutron powder diffraction pattern of a working commercial ammonia catalyst at 330 °C and under 60 bar of syngas. A Rietveld-refinement based phase deconvolution was applied to the data. Bragg-positions of α-iron (top) and a spinel phase (structural model: Fe_3O_4, bottom) are marked, the difference between the model and the data is shown by the solid line above. The inset compares the asymmetric peak broadening of the 211 reflex of the α-iron-phase to the instrumental resolution function (narrow peak). 40

5.3 TEM micrograph and energy dispersive X-ray (EDX) spectra of the sample used during in-situ neutron diffraction. The point analysis spectra reveal that in addition to the α-iron particles (1) areas which are enriched in oxygen and in the promoter species are also present (2,3). These areas are found near the edges of the iron particles (2) and as an embedding matrix consisting of partially crystalline calcium ferrite/iron aluminum spinel (3). 41

6.1 Representative TEM images of CZ (a), CZA-1 (b) and CZA-2 (c) taken at moderate magnification that were used for particle size evaluation. HRTEM image of a Cu nanoparticle in the sample CZA-1 that shows the presence of planar defects (stacking faults and twin boundaries, arrows). For more HRTEM-images cf. [8, 22, 30, 5] 50

6.2 Log-normal fits of the particle size histograms obtained by evaluation of the TEM images of the three different catalysts (the histograms are presented as supporting information). 51

6.3 Rietveld plots of the C-ref material and the samples CZ, CZA-1 and CZA-2 and (black experimental data; red calculated pattern; blue difference curve). The peaks due to fcc-Cu are indexed in the uppermost panel, those due to Wurzite-type ZnO are marked *. Note the systematic deviations in the difference curves of the three catalysts. 54

6.4 Comparison of the fitting results of the 331-420 peak doublet of CZA-1 using the Rietveld method and the model-free pattern decomposition method. The larger deviations between calculated and experimental data in the upper panel are due to the restrictions implied by the ideal structural model used for the refinement. 56

6.5 Williamson-Hall plots of C-ref and the three catalyst sample CZ, CZA-1 and CZA-2. The deviations of the three catalysts from linearity are discussed in detail in the text. 59

6.6 Modified Williamson-Hall plots of the C-ref and the three catalysts samples CZ, CZA-1 and CZA-2. 61

6.7 HRTEM image of a typical faulted Cu nanoparticle in a Cu/ZnO-based methanol synthesis catalyst. The close-up of the Cu lattice shows the stacking sequence of the (111) layers around the intrinsic stacking fault (left hand side) and exemplifies the different effects on the (111) and ($\bar{1}$11) components of the 111 diffraction peak. 62

6.8 Deconvoluted smoothed peak profiles of CZA-2 (2nd row), CZA-1 (3rd row), CZ (4th row) and C-ref (bottom row) compared to DIFFaX simulations of stacking fault-affected fcc-Cu (1st row). The profiles of the 111 (1st column), 200 (2nd column), 220 (3rd column), 222 (4th column) and 400 (last column) are shown. The same deconvolution procedure was applied to all peaks and all experimental patterns. Note the smaller Q-scale for the 1st row on the uppermost panels, which is compared to the scale of row 2-5 by the red lines between the 1st and 2nd row. 65

6.9 Comparison of the best fits using an ideal structure model (Rietveld, upper panel) and a methodology that accounts for the presence of lattice imperfections (WPPM, lower panel) 68

6.10 Comparison of area-normalized distribution functions for the domain sizes extracted from the WPPM and the particle sizes determined by TEM. . . 69

6.11 Full XRD pattern of the sample CZA-1. The upper panel shows the best fit obtained by Rietveld refinement without considering structural imperfections, while the lower panel is the WPPM fit taking defects into account. . 70

7.1 Diffraction pattern of the fresh Cu/Zn/Al2O3 catalyst aquried at room temperature with ND (black pattern) and laboratory XRD (Cu K_α, grey pattern). Peaks due to Cu are indexed. Due to different wavelengths used, the abscissa is given in reciprocal space. 75

7.2 High-resolution TEM image of a typical ellipsoidal copper particle in the used catalyst. Planar defects and the resulting thin hcp domain are marked in the close-up. 76

7.3 Rietveld-fits of the catalyst before (0.1 MPa Ar, upper panel), at the beginning (center) and after 24 hours of methanol synthesis (bottom) at 523 K and 6 MPa. Experimental data is shown in grey, the calculated pattern of the catalyst as black line. The thin grey line is the difference between experimental and calculated pattern. The contribution of the Cu phase and ZnO is marked as red and green lines with tick marks at the positions of Bragg reflections. Additional strong peaks due to the Al reactor wall were treated as peak-phase during Rietveld-analysis and are excluded from the overall calculated profile shown here. 77

7.4 d_{111}/d_{200} ratio of Cu in the catalyst and reference sample over TOS during methanol synthesis under industrially relevant conditions in the high resolution- (a) and high flux-experiments (b). This ratio is a measure for the defectiveness of Cu (see text). The formally resulting stacking fault concentration α is shown on the right axis of (b). The error bars are the standard deviations of the two datasets neglecting systematic errors due to, e.g., wavelength and zero-shift. 78

7.5 Evolution of the lattice parameter of Cu in the $Cu/ZnO/Al_2O_3$ catalyst and of the Cu reference powder with temperature. The Cu powder was heated in Ar at 0.1 MPa, while the calcined catalyst was heated to 523 K in D_2 (0.1 MPa), then subjected to 12 hours of methanol synthesis at 523 K in the syngas feed (6 MPa) and finally heated in D_2 (0.1 MPa) to 653 K. Heating rate was 1 K/min and one ND pattern corresponds to ca. 5 K. The dashed square at 523 K marks the period of 12 h synthesis. The right axis shows the lattice expansion relative to the reference at 298 K. 79

8.1 Neutron diffraction pattern of commercial iron powder (bottom, red) and iron nitride (middle, black, $Fe_{2-4}N$) and the post-reaction industrial ammonia synthesis catalyst at room temperature (top). Rietveld refinement revealed the presence of α-Fe (red profile) and peaks due to the reactor cell walls (marked). 86

8.2 Neutron diffraction patterns of the ammonia synthesis catalysts at different conditions. The solid red line indicates the fitted contribution α-Fe phase to the patterns. a) reduced, initial catalyst in 5 bar D_2 at 180 °C (the olive line is the profile of magnetite, peaks additionally marked by asterisks); b) pre-reaction catalyst at 425 °C under 75 bar syngas at TOS=0h; c) in-situ reaction state at 425 °C under 75 bar syngas, which is converted to yield 12 vol.% ND_3 at TOS=88 h d) post-reaction catalyst in 75 bar Ar at room temperature. The insets show the magnification of the 200 peak of α-Fe, wherein the black asterisks marks the contribution from the Ni-reactor tube. 88

8.3 a) Normalized peaks profiles of the 200 (right, top), 211 (left, top), 220 (right, bottom) and 222 (left, bottom) of the catalysts a-Fe reflections. The thermal shift from 28 °C (reference-iron, black and post-reaction state, green) to 180 °C (pre-reaction state) and 425 °C (12 vol.% ND_3) was compensated by normalizing to the peak maxima on the x-axis. b) Representative HRTEM micrograph of the post-reaction ammonia catalyst. The inset in the upper left corner shows the power spectrum of the TEM image. The interference in the outer region of the iron lattice is assigned to a tetragonal inclusion into the host lattice. 89

A.1 IRF of the fine resolution powder diffractometer (Firepod, E9) at the research reactor BER II at Helmholtz-Centre Berlin in the former configuration [127] with Y_2O_3. 95

A.2 IRF of the X-ray diffractometer (Bruker D8 Advance) in Bragg-Brentano geometry, determined with LaB_6. 95

D.1 Williamson-Hall plot from the single peak fit of the reduced, TOS=0h, TOS=88h, post-reaction catalyst and Fe-reference 111

List of Tables

6.1 characteristics of the investigated samples, values taken from SI of [9] . . . 45

6.2 Results of the apparent crystal size determined by application of the Scherrer formula on the integral breadth of each individual peak resulting from pattern decomposition (K = 0.89). The averaged apparent crystal size is given in the last column. 58

6.3 Refinement results of the PM2K-fit of the neutron diffraction patterns of C-ref and CZA-1 (a = lattice parameter; D_{ave}=average domain size; α= stacking fault probability; β = the twinning probability; ρ = dislocation density; R_e = effective outer cut-off radius; b = the Burgers vector; γ = stacking fault energy; GOF = goodness of fit). 67

6.4 Difference in the measure of the "size-effect" according to specific methods. 72

C.1 Mechanical properties of Nimonic alloy 80A. Heat treated 8 h at 1080°C and air cooled for 16 h at 700°C, cooled to RT by air(Values taken from Special Metals). 104

C.2 Mechanical properties of aluminium alloy AlMg3 (Values taken from [94]. . 105

C.3 Mechanical properties of stainless steel alloy 316L (Values taken from Swagelok).105

C.4 Mechanical properties of stainless steel alloy 304 (Values taken from Matweb online-resource). 105

Bibliography

[1] G. Schatz, A. Weidinger, Nukleare Festkörperphysik, B.G. Teubner, 1992.

[2] M. Hölzl, Struktur und Gitterdynamik wasserstoffbeladener austenitischer Edelstähle, Ph.D. thesis, Technische Universität Darmstadt (2003).

[3] T. Kandemir, D. Wallacher, T. Hansen, K.-D. Liss, R. Naumann d'Alnoncourt, R. Schlögl, M. Behrens, In situ neutron diffraction under high pressure Providing an insight into working catalysts, Nuclear Instruments and Methods in Physics Research Section A: Accelerators, Spectrometers, Detectors and Associated Equipment 673 (0) (2012) 51–55.
URL `http://www.sciencedirect.com/science/article/pii/S0168900212000538`

[4] T. Kandemir, F. Girgsdies, I. Kasatkin, E. Kunkes, K.-D. Liss, V. K. Peterson, R. Schlögl, M. Behrens, Heterogeneous Catalysis under pressure - In-situ neutron diffraction under industrial conditions, Journal of Physics: Conference Series 340 (1) (2012) 012053.
URL `http://stacks.iop.org/1742-6596/340/i=1/a=012053`

[5] T. Kandemir, F. Girgsdies, T. C. Hansen, K.-D. Liss, I. Kasatkin, E. L. Kunkes, G. Wowsnick, N. Jacobsen, R. Schlögl, M. Behrens, In Situ Study of Catalytic Processes: Neutron Diffraction of a Methanol Synthesis Catalyst at Industrially Relevant Pressure, Angewandte Chemie International Edition 52 (19) (2013) 5166–5170. `doi:10.1002/anie.201209539`.
URL `http://dx.doi.org/10.1002/anie.201209539`

[6] T. Wieder, Realstrukturaufklärung polykristalliner dünner Schichten mittels Röntgenbeugung, Habilitation treatise, Technische Hochschule Darmstadt.

[7] P. Maass, A. Rieder, A. K. Louis, Wavelets, B.G. Teubner, 1994.

[8] I. Kasatkin, P. Kurr, B. Kniep, A. Trunschke, R. Schlögl, Role of lattice strain and defects in copper particles on the activity of Cu/ZnO/Al2O3 catalysts for methanol synthesis, Angew. Chem.-Int. Ed. 46 (38) (2007) 7324–7327.

[9] M. Behrens, F. Studt, I. Kasatkin, S. Kühl, M. Hävecker, F. Abild-Pedersen, S. Zander, F. Girgsdies, P. Kurr, B.-L. Kniep, M. Tovar, R. W. Fischer, J. K. Norskov, R. Schlögl, The Active Site of Methanol Synthesis over Cu/ZnO/Al2O3 Industrial Catalysts, Science 336 (6083) (2012) 893–897. `arXiv:http://www.sciencemag.org/content/336/6083/893.full.pdf`.

[10] M. Leoni, T. Confente, P. Scardi, PM2K: a flexible program implementing Whole Powder Pattern Modelling, Z. Kristallogr. Suppl. 2006 (23) (2006) 249–254, suppl.

[11] www.methanol.org/Methanol-Basics.
URL `www.methanol.org/Methanol-Basics`

[12] L. E. Apodaca, Mineral Commodity Summaries, Nitrogen (fixed) - Ammonia, Tech. rep., U.S. Geological Survey (2011).

[13] T. Rostrup-Nielsen, Manufacture of hydrogen, Catalysis Today 106 (14) (2005) 293 – 296, ¡ce:title¿International Conference on Gas-Fuel 05¡/ce:title¿ ¡ce:subtitle¿International Conference on Gas-Fuel 05¡/ce:subtitle¿ ¡xocs:full-name¿International Conference on Gas-Fuel 05¡/xocs:full-name¿. `doi:10.1016/j.cattod.2005.07.149`.
URL `http://www.sciencedirect.com/science/article/pii/S0920586105005432`

[14] J. R. Jennings (Ed.), Catalytic Ammonia Synthesis - Fundamentals and Practice, Plenum Press, 1991.

[15] J. Yoshihara, C. T. Campbell, Methanol Synthesis and Reverse WaterGas Shift Kinetics over Cu(110) Model Catalysts: Structural Sensitivity, Journal of Catalysis 161 (2) (1996) 776 – 782. `doi:10.1006/jcat.1996.0240`.
URL `http://www.sciencedirect.com/science/article/pii/S0021951796902407`

[16] M. Boudart, Kinetics and Mechanism of Ammonia Synthesis, Catal. Rev.-Sci. Eng. 23 (1&2) (1981) 1–15.

[17] D. Waller, D. Stirling, F. S. Stone, M. S. Spencer, Copper-zinc oxide catalysts. Activity in relation to precursor structure and morphology, Faraday Discuss. Chem. Soc. 87 (1989) 107–120.

[18] M. Spencer, The role of zinc oxide in Cu/ZnO catalysts for methanol synthesis and the water-gas shift reaction, Topics in Catalysis 8 (1999) 259–266.

[19] L. K. Rihko-Struckmann, A. Peschel, R. Hanke-Rauschenbach, K. Sundmacher, Assessment of Methanol Synthesis Utilizing Exhaust CO2 for Chemical Storage of Electrical Energy, Industrial & Engineering Chemistry Research 49 (21) (2010) 11073–11078. `arXiv:http://pubs.acs.org/doi/pdf/10.1021/ie100508w`, `doi:`

10.1021/ie100508w.
URL http://pubs.acs.org/doi/abs/10.1021/ie100508w

[20] R. R. Aronsson, K. Kordesch, M. Cifrain, G. Koscher, G. Faleschini, V. Hacker, FY 2004 Progress Report: Alkaline Fuel Cell-Battery Hybrid Systems with Ammonia or Methanol as Hydrogen Supply, Tech. rep., DOE Hydrogen Program (2004).

[21] K. Klier, Methanol Synthesis, in: D. Eley, H. Pines, P. B. Weisz (Eds.), Advances in Catalysis, Vol. Volume 31, Academic Press, 1982, pp. 243–313.
URL http://www.sciencedirect.com/science/article/pii/S0360056408604551

[22] M. Behrens, Meso- and nano-structuring of industrial Cu/ZnO/(Al_2O_3) catalysts, J. Catal. 267 (2009) 24–29.

[23] P. Rasmussen, M. Kazuta, I. Chorkendorff, Synthesis of methanol from a mixture of H2 and CO2 on Cu(100), Surface Science 318 (3) (1994) 267 – 280. doi:10.1016/0039-6028(94)90101-5.
URL http://www.sciencedirect.com/science/article/pii/0039602894901015

[24] P. Rasmussen, P. Holmblad, T. Askgaard, C. Ovesen, P. Stoltze, J. Nrskov, I. Chorkendorff, Methanol synthesis on Cu(100) from a binary gas mixture of CO2 and H2, Catalysis Letters 26 (1994) 373–381. doi:10.1007/BF00810611.
URL http://dx.doi.org/10.1007/BF00810611

[25] T. Fujitani, J. Nakamura, The effect of ZnO in methanol synthesis catalysts on Cu dispersion and the specific activity, Catalysis Letters 56 (2) (1998) 119–124.
URL http://dx.doi.org/10.1023/A:1019000927366

[26] T. Ressler, B. L. Kniep, I. Kasatkin, R. Schlögl, The Microstructure of Copper Zinc Oxide Catalysts: Bridging the Materials Gap, Angewandte Chemie International Edition 44 (30) (2005) 4704–4707.

[27] P. Kurr, Microstrucutral characterization of Cu/ZnO/Al_2O_3 catalysts for the synthesis and steam reforming of methanol, Ph.D. thesis, TU Berlin (2008).

[28] M. Behrens, F. Girgsdies, A. Trunschke, R. Schlögl, Minerals as Model Compounds for Cu/ZnO Catalyst Precursors: Structural and Thermal Properties and IR Spectra of Mineral and Synthetic (Zincian) Malachite, Rosasite and Aurichalcite and a Catalyst Precursor Mixture, European Journal of Inorganic Chemistry 2009 (10) (2009) 1347–1357. doi:10.1002/ejic.200801216.
URL http://dx.doi.org/10.1002/ejic.200801216

[29] R. Hadden, B. Sakakini, J. Tabatabaei, K. Waugh, Adsorption and reaction induced morphological changes of the copper surface of a methanol synthesis catalyst, Catalysis Letters 44 (1997) 145–151. doi:10.1023/A:1018962016811.
URL http://dx.doi.org/10.1023/A%3A1018962016811

[30] M. Behrens, A. Furche, I. Kasatkin, A. Trunschke, W. Busser, M. Muhler, B. Kniep, R. Fischer, R. Schlogl, The Potential of Microstructural Optimization in Metal/Oxide Catalysts: Higher Intrinsic Activity of Copper by Partial Embedding of Copper Nanoparticles, Chemcatchem 2 (7) (2010) 816–818, 632MZ Times Cited:8 Cited References Count:28.
URL `<GotoISI>://000280430100010`

[31] J. B. Hansen, P. E. H. Nielsen, Handbook of Heterogeneous Catalysis, Wiley-VCH Verlag GmbH & Co. KGaA, 2008, Ch. Methanol Synthesis.

[32] M. V. Twigg, M. S. Spencer, Deactivation of copper metal catalysts for methanol decomposition, methanol steam reforming and methanol synthesis, Top. Catal. 22 (3-4) (2003) 191–203.
URL `<GotoISI>://000182582600007`

[33] R. Burch, S. E. Golunski, M. Spencer, The role of copper and zinc oxide in methanol synthesis catalysts, J. Chem. Soc., Faraday Trans. 86 (15) (1990) 2683–2691.
URL `http://dx.doi.org/10.1039/FT9908602683`

[34] R. N. d'Alnoncourt, X. Xia, J. Strunk, E. Loffler, O. Hinrichsen, M. Muhler, The influence of strongly reducing conditions on strong metal-support interactions in Cu/ZnO catalysts used for methanol synthesis, Physical Chemistry Chemical Physics 8 (13) (2006) 1525–1538.
URL `<GotoISI>://000236250700009`

[35] C. T. Campbell, K. A. Daube, J. White, Cu/ZnO(0001) and ZnOx/Cu(111): Model catalysts for methanol synthesis, Surface Science 182 (3) (1987) 458 – 476. `doi:10.1016/0039-6028(87)90013-6`.
URL `http://www.sciencedirect.com/science/article/pii/0039602887900136`

[36] M. M. Günther, T. Ressler, B. Bems, C. Buscher, T. Genger, O. Hinrichsen, M. Muhler, R. Schlögl, Implication of the microstructure of binary Cu/ZnO catalysts for their catalytic activity in methanol synthesis, Catalysis Letters 71 (1-2) (2001) 37–44.

[37] T. Johannessen, J. H. Larsen, I. Chorkendorff, H. Livbjerg, H. Topse, Catalyst dynamics: consequences for classical kinetic descriptions of reactors, Chemical Engineering Journal 82 (13) (2001) 219 – 230, ¡ce:title¿FRONTIERS IN CHEMICAL REACTION ENGINEERING¡/ce:title¿. `doi:10.1016/S1385-8947(00)00338-7`.
URL `http://www.sciencedirect.com/science/article/pii/S1385894700003387`

[38] J. B. Wagner, P. L. Hansen, A. M. Molenbroek, H. Topse, B. S. Clausen, S. Helveg, In Situ Electron Energy Loss Spectroscopy Studies of Gas-Dependent MetalSupport Interactions in Cu/ZnO Catalysts, The Journal of Physical Chemistry B 107 (31) (2003) 7753–7758. `arXiv:http://pubs.acs.org/doi/pdf/10.1021/jp0277863`,

`doi:10.1021/jp0277863`.
URL `http://pubs.acs.org/doi/abs/10.1021/jp0277863`

[39] C. Ovesen, B. Clausen, J. Schiotz, P. Stoltze, H. Topsoe, J. Norskov, Kinetic Implications of Dynamical Changes in Catalyst Morphology during Methanol Synthesis over Cu/ZnO Catalysts, Journal of Catalysis 168 (2) (1997) 133 – 142. `doi:10.1006/jcat.1997.1629`.
URL `http://www.sciencedirect.com/science/article/pii/S0021951797916298`

[40] P. L. Hansen, J. B. Wagner, S. Helveg, J. R. Rostrup-Nielsen, B. S. Clausen, H. Topse, Atom-Resolved Imaging of Dynamic Shape Changes in Supported Copper Nanocrystals, Science 295 (5562) (2002) 2053–2055.
URL `http://www.sciencemag.org/content/295/5562/2053.abstract`

[41] J. Grunwaldt, A. Molenbroek, N. Topsoe, H. Topsoe, B. Clausen, In situ investigations of structural changes in Cu/ZnO catalysts, J. Catal. 194 (2) (2000) 452–460.

[42] M. Spencer, α-brass formation in copper/zinc oxide catalysts: II. Diffusion of zinc in copper and α-brass under reaction conditions, Surface Science 192 (2-3) (1987) 329–335.
URL `http://www.sciencedirect.com/science/article/pii/S0039602887811287`

[43] M. Kurtz, H. Wilmer, T. Genger, O. Hinrichsen, M. Muhler, Deactivation of Supported Copper Catalysts for Methanol Synthesis, Catalysis Letters 86 (1) (2003) 77–80.
URL `http://dx.doi.org/10.1023/A:1022663125977`

[44] P. Wynblatt, N. Gjostein, Particle growth in model supported metal catalystsI. Theory, Acta Metallurgica 24 (12) (1976) 1165 – 1174. `doi:10.1016/0001-6160(76)90034-1`.
URL `http://www.sciencedirect.com/science/article/pii/0001616076900341`

[45] B. Min, A. Santra, D. Goodman, Understanding silica-supported metal catalysts: Pd/silica as a case study, Catalysis Today 85 (24) (2003) 113 – 124. `doi:10.1016/S0920-5861(03)00380-8`.
URL `http://www.sciencedirect.com/science/article/pii/S0920586103003808`

[46] G. C. Bond, Metal-Catalysed Reactions of Hydrocarbons, Fundamental and Applied Catalysis, Springer, 2005.

[47] D. R. Lide (Ed.), CRC Handbook of Chemistry and Physics, 84th Edition, CRC Press LLC, 2003-2004.

[48] J. Moulijn, A. van Diepen, F. Kapteijn, Catalyst deactivation: is it predictable?: What to do?, Applied Catalysis A: General 212 (12) (2001) 3 – 16. `doi:10.1016/S0926-860X(00)00842-5`.
URL `http://www.sciencedirect.com/science/article/pii/S0926860X00008425`

[49] P. Kurr, I. Kasatkin, F. Girgsdies, A. Trunschke, R. Schlgl, T. Ressler, Microstructural characterization of Cu/ZnO/Al2O3 catalysts for methanol steam reformingA comparative study, Applied Catalysis A: General 348 (2) (2008) 153 – 164. `doi:10.1016/j.apcata.2008.06.020`.
URL `http://www.sciencedirect.com/science/article/pii/S0926860X08003645`

[50] T. M. Yurieva, L. M. Plyasova, V. I. Zaikovskii, T. P. Minyukova, A. Bliek, J. C. van den Heuvel, L. P. Davydova, I. Y. Molina, M. P. Demeshkina, A. A. Khassin, E. D. Batyrev, In situ XRD and HRTEM studies on the evolution of the Cu/ZnO methanol synthesis catalyst during its reduction and re-oxidation, Phys. Chem. Chem. Phys. 6 (18) (2004) 4522–4526.
URL `http://dx.doi.org/10.1039/B407728H`

[51] G. Ertl, Surface Science and Catalysis Studies on the Mechanism of Ammonia Synthesis: The P. H. Emmett Award Address, Catalysis Reviews 21 (2) (1980) 201–223. `arXiv:http://www.tandfonline.com/doi/pdf/10.1080/03602458008067533`, `doi:10.1080/03602458008067533`.
URL `http://www.tandfonline.com/doi/abs/10.1080/03602458008067533`

[52] G. Ertl, Primary steps in catalytic synthesis of ammonia, J. Vac. Sci. Technol. A 1 (1983) 1247–1253.

[53] F. Bozso, G. Ertl, M. Grunze, M. Weiss, Interaction of Nitrogen with iron Surfaces I. Fe(100) and Fe(111), Journal of Catalysis 49 (1977) 18–41.

[54] G. Ertl, N. Thiele, XPS studies with ammonia synthesis catalysts, Applications of Surface Science 3 (1) (1979) 99 – 112. `doi:10.1016/0378-5963(79)90064-3`.
URL `http://www.sciencedirect.com/science/article/pii/0378596379900643`

[55] N. Spencer, R. Schoonmaker, G. Somorjai, Iron single crystals as ammonia synthesis catalysts: Effect of surface structure on catalyst activity, Journal of Catalysis 74 (1) (1982) 129 – 135. `doi:10.1016/0021-9517(82)90016-1`.
URL `http://www.sciencedirect.com/science/article/pii/0021951782900161`

[56] B. Herzog, D. Herein, R. Schlögl, In situ X-ray powder diffraction analysis of the microstructure of activated iron catalysts for ammonia synthesis, Applied Catalysis A: General 141 (12) (1996) 71–104.
URL `http://www.sciencedirect.com/science/article/pii/0926860X96000427`

[57] R. Schlögl, Ammonia Synthesis, 2nd Edition, Vol. 5 of Handbook of Heterogeneous Catalysis, Wiley-VCH, Weinheim, 2008.

[58] B. Holme, P. Skaugset, J. Taft, Microstructure of reduced magnetite as a function of aluminum content and reduction temperature, Appl. Catal. A 162 (12) (1997) 149 – 159. `doi:10.1016/S0926-860X(97)00092-6`.
URL `http://www.sciencedirect.com/science/article/pii/S0926860X97000926`

[59] G. Ertl, M. Huber, N. Thiele, Formation and decomposition of Nitrides on Iron Surfaces, Z. Naturforsch. A 34a (1979) 30–39.

[60] M. Boudart, Virtual pressure and virtual fugacity in catalysis and electrocatalysis, Catalysis Letters 3 (1989) 111–115. `doi:10.1007/BF00763721`.
URL `http://dx.doi.org/10.1007/BF00763721`

[61] M. Temkin, V. Pyzhev, Zhur. Fiz. Xhim. 13 (1939) 851.

[62] J.-D. Grunwaldt, B. S. Clausen, Combining XRD and EXAFS with on-line catalytic studies for in situ characterization of catalysts, Topics in Catalysis 18 (1-2) (2002) 37–43.

[63] N. Kardjilov, I. Manke, M. Strobl, A. Hilger, W. Treimer, M. Meissner, T. Krist, J. Banhart, Three-dimensional imaging of magnetic fields with polarized neutrons, Nat Phys 4 (5) (2008) 399–403.
URL `http://dx.doi.org/10.1038/nphys912`

[64] A.-J. Dianoux, G. Lander (Eds.), Neutron Data Booklet, Institut Laue-Langevin, 2003.

[65] J. F. C. Turner, R. Done, J. Dreyer, W. I. F. David, C. R. A. Catlow, On apparatus for studying catalysts and catalytic processes using neutron scattering, Rev. Sci. Instrum. 70 (5) (1999) 2325–2330, 193AU Times Cited:6 Cited References Count:11.
URL `<GotoISI>://000080113600020`

[66] R. I. Walton, R. J. Francis, P. S. Halasyamani, D. O. Hare, R. I. Smith, R. Done, R. J. Humphreys, Novel apparatus for the in situ study of hydrothermal crystallizations using time-resolved neutron diffraction, Review of Scientific Instruments 70 (8) (1999) 3391–3396.

[67] D. Lennon, D. T. Lundie, S. D. Jackson, G. J. Kelly, S. F. Parker, Characterization of activated carbon using X-ray photoelectron spectroscopy and inelastic neutron scattering spectroscopy, Langmuir 18 (12) (2002) 4667–4673, 560QC Times Cited:16 Cited References Count:41.
URL `<GotoISI>://000176091900022`

[68] A. R. McInroy, D. T. Lundie, J. M. Winfield, C. C. Dudman, P. Jones, S. F. Parker, J. W. Taylor, D. Lennon, An infrared and inelastic neutron scattering spectroscopic investigation on the interaction of eta-alumina and methanol, Physical Chemistry Chemical Physics 7 (16) (2005) 3093–3101, 951LH Times Cited:15 Cited References Count:58.
URL `<GotoISI>://000230931200015`

[69] A. R. McInroy, D. T. Lundie, J. M. Winfield, C. C. Dudman, P. Jones, S. F. Parker, D. Lennon, The interaction of alumina with HCl: An infrared spectroscopy, temperature-programmed desorption and inelastic neutron scattering study, Catalysis Today 114 (4) (2006) 403–411, 049ZO Times Cited:15 Cited References Count:42.
URL `<GotoISI>://000238057100014`

[70] S. F. Parker, J. W. Taylor, P. Albers, M. Lopez, G. Sextl, D. Lennon, A. R. McInroy, I. W. Sutherland, Inelastic neutron scattering studies of hydrogen on fuel cell catalysts, Vib. Spectrosc. 35 (1-2) (2004) 179–182, 824LX Times Cited:10 Cited References Count:14.
URL `<GotoISI>://000221689200029`

[71] P. W. Albers, S. F. Parker, Applications of Neutron Scattering in the Chemical Industry: Proton Dynamics of Highly Dispersed Materials, Characterization of Fuel Cell Catalysts, and Catalysts from Large-Scale Chemical Processes Neutron Applications in Earth, Energy and Environmental Sciences, Neutron Scattering Applications and Techniques, Springer US, 2009, pp. 391–416.
URL `http://dx.doi.org/10.1007/978-0-387-09416-8_13`

[72] B. S. Clausen, G. Steffensen, B. Fabius, J. Villadsen, R. Feidenhans'l, H. Topse, In situ cell for combined XRD and on-line catalysis tests: Studies of Cu-based water gas shift and methanol catalysts, Journal of Catalysis 132 (2) (1991) 524–535.
URL `http://www.sciencedirect.com/science/article/pii/0021951791901684`

[73] B. S. Clausen, H. Topsoe, In Situ High Pressure, High Temperature XAFS Studies of Cu-based Catalysts during Methanol Synthesis, Catalysis Today 9 (1991) 189–196.

[74] B. Warren, X-ray studies of deformed metals, Progress in Metal Physics 8 (0) (1959) 147–202.

[75] B. E. Warren, X-ray Measurements of Stacking Fault Widths in fcc Metals, J. Appl. Phys. 32 (1961) 2428.

[76] B. E. Warren, X-Ray Diffraction, Dover Publications, 1990.

[77] H. M. Rietveld, A profile refinement method for nuclear and magnetic structures, Journal of Applied Crystallography 2 (2) (1969) 65–71.

[78] G. Weinberg, B. Beran, M. Muhler, R. Schlögl, A. Dent, T. Rayment, The micromorphology of the activated iron catalyst used for ammonia synthesis, Applied Catalysis A: General 163 (12) (1997) 83 – 99. `doi:10.1016/S0926-860X(97)00119-1`.
URL `http://www.sciencedirect.com/science/article/pii/S0926860X97001191`

[79] R. Schlögl, Catalytic Ammonia Synthesis, Fundamentals and Practise, Plenum, New York, 1991.

[80] N. Ridley, H. Stuart, Lattice parameter anomalies at the Curie point of pure iron, Journal of Physics D: Applied Physics 1 (10) (1968) 1291.
URL `http://stacks.iop.org/0022-3727/1/i=10/a=308`

[81] R. Hosemann, A. Preisinger, W. Vogel, Über den α-Fe-$FeAl_2O_4$-Mischkristall in aktivierten Ammoniakkatalysatoren, Ber. Bunsenges. Phys. Chem. 70 (8) (1966) 796–802. `doi:10.1002/bbpc.19660700806`.
URL `http://dx.doi.org/10.1002/bbpc.19660700806`

[82] W. Mahdi, J. Schtze, G. Weinberg, R. Schoonmaker, R. Schlgl, G. Ertl, Microstructure of the activated industrial ammonia synthesis catalyst, Catalysis Letters 11 (1991) 19–31. `doi:10.1007/BF00866897`.
URL `http://dx.doi.org/10.1007/BF00866897`

[83] B. Holme, J. Tafto, Mechanism of transformation from $Fe_{3-x}Al_xO_4$ to porous Fe by exposure to H_2 gas, Phil. Mag. A. 80 (2) (2000) 373–387. `arXiv:http://www.tandfonline.com/doi/pdf/10.1080/01418610008212058`, `doi:10.1080/01418610008212058`.
URL `http://www.tandfonline.com/doi/abs/10.1080/01418610008212058`

[84] V. F. Sears, Neutron scattering lengths and cross sections, Neutron News 3 (3) (1992) 26–37.
URL `http://www.tandfonline.com/doi/abs/10.1080/10448639208218770`

[85] B. van den Brandt, H. Glättli, H. Griesshammer, P. Hautle, J. Kohlbrecher, J. Konter, O. Zimmer, The spin-dependent nd scattering length - a proposed high-accuracy measurement, Nucl.Instrum.Meth. A 526 (12) (2004) 91 – 95. `doi:10.1016/j.nima.2004.03.156`.
URL `http://www.sciencedirect.com/science/article/pii/S0168900204005637`

[86] R. Snyder, J. Fiala, H. J. Bunge (Eds.), Defect and Microstructure Analysis by Diffraction, OUP//International Union of Crystallography, 2000.

[87] R. A. Young (Ed.), The Rietveld Method, International Union of Crystallography, Oxford University Press, 1993.

[88] D. B. Williams, C. B. Carter, Transmission Electron Microscopy - A Textbook for Materials Science, Vol. 1, Springer Berlin / Heidelberg, 2009.

[89] NIST, NIST Chemistry WebBook (2012).
URL `http://webbook.nist.gov/chemistry/`

[90] J. H. Gross, Mass Spectrometry, 2nd Edition, Springer Berlin / Heidelberg, 2011.

[91] K. Cammann (Ed.), Instrumentelle Analytische Chemie: Verfahren, Anwendungen und Qualitätssicherung, Spektrum Akademischer Verlag, 2001.

[92] E. Riedel, Anorganische Chemie, 6th Edition, Walter de Gruyter, 2004.

[93] H. Matsui, Hydrogen Embrittlement in Vanadium and Niobium, Tech. rep., 1774th report of The Research Institute for Iron, Steel and Other Materials (1984).

[94] A. Scharff, S. Allmeier, DVS-Berichte Band 237, Tech. Rep. 467 (2005).

[95] DIN EN 13480-3/A1:2005 Metallic industrial piping Part 3: Design and calculation (2005).

[96] D. Hamaguchi, Y. Dai, Microstructural change in AlMg3 alloy irradiated by spallation neutrons and high energy protons, J. Nucl. Mater. 329-333 (Part 2) (2004) 958 – 962, proceedings of the 11th International Conference on Fusion Reactor Materials (ICFRM-11).

[97] I. P. Orench, J. A. R. Velamazán, J. Campo, The Spanish CRG Instruments at ILL: Historical Perspective and Future Developments, Neutron News 21 (3) (2010) 20–23.

[98] K.-D. Liss, B. Hunter, M. Hagen, T. Noakes, S. Kennedy, Echidna–the new high-resolution powder diffractometer being built at OPAL, Physica B: Condensed Matter 385-386 (2006) 1010–1012.

[99] M. Avdeev, J. R. Hester, V. K. Peterson, A. J. Studer, Wombat and Echidna: The Powder Diffractometers, Neutron News 20 (4) (2009) 29–33.

[100] J. A. Rodriguez, J. Kim, J. Hanson, M. Pérez, A. I. Frenkel, Reduction of CuO in H_2: In Situ Time-Resolved XRD Studies, Catalysis Letters 85 (2003) 247–254.

[101] G. Chinchen, C. Hay, H. Vandervell, K. Waugh, The measurement of copper surface areas by reactive frontal chromatography, Journal of Catalysis 103 (1) (1987) 79 – 86. `doi:10.1016/0021-9517(87)90094-7`.
URL `http://www.sciencedirect.com/science/article/pii/0021951787900947`

[102] G. Ertl, Catalytic Ammonia Synthesis, Fundamentals and Practise, Plenum, 1991.

[103] A. Mittasch, Early studies of multicomponent catalysts, Adv. Catal. D 2 (1950) 81–104.

[104] R. Egeberg, S. Dahl, A. Logadottir, J. Larsen, J. Norskov, I. Chorkendorff, N_2 dissociation on Fe(1 1 0) and Fe/Ru(0 0 0 1): what is the role of steps?, Surface Science 491 (1 - 2) (2001) 183 – 194. `doi:10.1016/S0039-6028(01)01397-8`.
URL `http://www.sciencedirect.com/science/article/pii/S0039602801013978`

[105] P. H. Emmett, K. S. Love, The Reduction by Hydrogen and the Thermal Decomposition of Nitrides Made by the Reaction of Ammonia with Various Promoted and Unpromoted Iron Synthetic Ammonia Catalysts, J. Am. Chem. Soc. 55 (10) (1933) 4043–4050. `arXiv:http://pubs.acs.org/doi/pdf/10.1021/ja01337a019`, `doi:10.1021/ja01337a019`.
URL `http://pubs.acs.org/doi/abs/10.1021/ja01337a019`

[106] H. Ludwiczek, A. Preisinger, A. Fischer, R. Hosemann, A. Schönfeld, W. Vogel, Structure, formation, and stability of paracrystalline ammonia catalysts, Journal of Catalysis 51 (3) (1978) 326 – 337. `doi:10.1016/0021-9517(78)90270-1`.
URL `http://www.sciencedirect.com/science/article/pii/0021951778902701`

[107] H. Okudera, K. Kihara, T. Matsumoto, Temperature dependence of structure parameters in natural magnetite: single crystal X-ray studies from 126 to 773 K, Acta Cryst. B 52 (3) (1996) 450–457. `doi:10.1107/S0108768196000845`.
URL `http://dx.doi.org/10.1107/S0108768196000845`

[108] R. Harrison, S. Redfern, H. O'Neill, The temperature dependence of the cation distribution in synthetic hercynite ($FeAl_2O_4$) from in-situ neutron structure refinements, American Mineralogist 83 (1998) 1092–1099.

[109] R. Brill, Röntgenographische Untersuchungen an Eisenkatalysatoren für die Ammoniak-Synthese, Ztschr. Elektrochem. 38 (8b) (1932) 669–673. `doi:10.1002/bbpc.19320380806`.
URL `http://dx.doi.org/10.1002/bbpc.19320380806`

[110] S. Dahl, A. Logadottir, R. C. Egeberg, J. H. Larsen, I. Chorkendorff, E. Tornqvist, J. K. Norskov, Role of steps in N-2 activation on Ru(0001), Physical Review Letters 83 (9) (1999) 1814–1817, 230GC Times Cited:328 Cited References Count:25.
URL `<GotoISI>://000082242600029`

[111] J. Rostrup-Nielsen, J. K. Norskov, Step sites in syngas catalysis, Topics in Catalysis 40 (1-4) (2006) 45–48, 114TT Times Cited:24 Cited References Count:30.
URL `<GotoISI>://000242689200005`

[112] F. Abild-Pedersen, J. Greeley, J. K. Norskov, Understanding the effect of steps, strain, poisons, and alloying: Methane activation on Ni surfaces, Catalysis Letters 105 (1-2) (2005) 9–13, 975XJ Times Cited:21 Cited References Count:27.
URL `<GotoISI>://000232697100002`

[113] T. Jiang, D. J. Mowbray, S. Dobrin, H. Falsig, B. Hvolbaek, T. Bligaard, J. K. Norskov, Trends in CO Oxidation Rates for Metal Nanoparticles and Close-Packed, Stepped, and Kinked Surfaces, Journal of Physical Chemistry C 113 (24) (2009) 10548–10553, 457LQ Times Cited:54 Cited References Count:50.
URL `<GotoISI>://000266930400038`

[114] H. J. Freund, Model Studies in Heterogeneous Catalysis, Chemistry-a European Journal 16 (31) (2010) 9384–9397, 646KS Times Cited:30 Cited References Count:127.
URL `<GotoISI>://000281539500007`

[115] A. K. Datye, Electron microscopy of catalysts: recent achievements and future prospects, Journal of Catalysis 216 (1-2) (2003) 144–154, 684VH Times Cited:42 Cited References Count:58.
URL `<GotoISI>://000183226900014`

[116] C. Weidenthaler, Pitfalls in the characterization of nanoporous and nanosized materials, Nanoscale 3 (3) (2011) 792–810, 732VR Times Cited:8 Cited References Count:62.
URL `<GotoISI>://000288218300002`

[117] A. D. Pandey, R. Guttel, M. Leoni, F. Schuth, C. Weidenthaler, Influence of the Microstructure of Gold-Zirconia Yolk-Shell Catalysts on the CO Oxidation Activity, Journal of Physical Chemistry C 114 (45) (2010) 19386–19394, 677UT Times Cited:4 Cited References Count:48.
URL `<GotoISI>://000284018100033`

[118] W. Vogel, Size Distributions of Supported Metal-Catalysts - an Analytical X-Ray-Line Profile Fitting Routine, Journal of Catalysis 121 (2) (1990) 356–363, cp263 Times Cited:8 Cited References Count:15.
URL `<GotoISI>://A1990CP26300013`

[119] S. V. Tsybulya, G. N. Kryukova, S. N. Goncharova, A. N. Shmakov, B. S. Balzhinimaev, Study of the Real Structure of Silver Supported Catalysts of Different Dispersity, Journal of Catalysis 154 (2) (1995) 194–200, rg041 Times Cited:46 Cited References Count:18.
URL `<GotoISI>://A1995RG04100003`

[120] F. M. Bautista, J. M. Campelo, A. Garcia, D. Luna, J. M. Marinas, R. A. Quiros, A. A. Romero, Influence of surface support properties on the liquid-phase selective hydrogenation of phenylacetylene on supported nickel catalysts, Catalysis Letters 52 (3-4) (1998) 205–213, zy977 Times Cited:13 Cited References Count:89.
URL `<GotoISI>://000074682600012`

[121] E. J. Mittemeijer, P. Scardi (Eds.), Diffraction Analysis of the Microstrucutre of Materials, Springer Series in Materials Science, 2004.

[122] E. Mittemeijer, U. Welzel, The state of the art of the diffraction analysis of crystallite size and lattice strain, Z. Kristallogr. 223 (2008) 552–560.

[123] H. Savaloni, M. Gholipour-Shahraki, M. A. Player, A comparison of different methods for x-ray diffraction line broadening analysis of Ti and Ag UHV deposited thin films: nanostructural dependence on substrate temperature and film thickness, Journal of Physics D: Applied Physics 39 (10) (2006) 2231.
URL `http://stacks.iop.org/0022-3727/39/i=10/a=036`

[124] M. Behrens, R. Schlögl, X-Ray Diffraction and Small Angle X-Ray Scattering, in: Characterization of Solid Materials and Heterogeneous Catalysts, Wiley-VCH Verlag GmbH & Co. KGaA, 2012, pp. 609–653.
URL `http://dx.doi.org/10.1002/9783527645329.ch15`

[125] H. P. Klug, L. E. Alexander, X-Ray Diffraction Procedures, 2nd Edition, John Wiley & Sons, New York, 1974.

[126] D. Balzar, N. Audebrand, M. R. Daymond, A. Fitch, A. Hewat, J. I. Langford, A. Le Bail, D. Louër, O. Masson, C. N. McCowan, N. C. Popa, P. W. Stephens, B. H. Toby, Size–strain line-broadening analysis of the ceria round-robin sample, J. Appl. Crystallogr. 37 (6) (2004) 911–924.

[127] D. Többens, M. Tovar, Peak shape at the axially focusing E9 powder diffractometer - theoretical and experimental description, Applied Physics A: Materials Science & Processing 74 (2002) s136–s138, 10.1007/s003390201927.

[128] G. Caglioti, A. Paoletti, F. Ricci, Choice of collimators for a crystal spectrometer for neutron diffraction, Nuclear Instruments 3 (4) (1958) 223 – 228.

[129] G. K. Wertheim, M. A. Butler, K. W. West, D. Buchanan, Determination of the Gaussian and Lorentzian content of experimental line shapes, Review of Scientific Instruments 45 (11) (1974) 1369–1371.

[130] R. W. Cheary, A. A. Coelho, Programs XFIT and FOURYA, deposited in CCP14 Powder Diffraction Library (1996).
URL `http://www.ccp14.ac.uk/tutorial/xfit-95/xfit.htm`

[131] A. Le Bail, H. Duroy, J. L. Fourquet, Ab initio structure determination of $LiSbWO_6$ by X-ray powder diffraction, Materials Research Bulletin 23 (3) (1988) 447–452.

[132] M. M. J. Treacy, J. M. Newsam, M. W. Deem, A General Recursion Method for Calculating Diffracted Intensities from Crystals Containing Planar Faults, Proceedings of the Royal Society of London. Series A: Mathematical and Physical Sciences 433 (1889) (1991) 499–520. `arXiv:http://rspa.royalsocietypublishing.org/content/433/1889/499.full.pdf+html`.

[133] M. Romeo, V. Da Costa, F. Bardou, Broad distribution effects in sums of lognormal random variables, The European Physical Journal B - Condensed Matter and Complex Systems 32 (2003) 513–525, 10.1140/epjb/e2003-00131-6.

[134] P. Gai, E. Boyes, Electron Microscopy in Heterogeneous Catalysis, Institute of Physics Publishing, 2003.

[135] M. H. Yao, D. J. Smith, A. K. Datye, Comparative-Study of Supported Catalyst Particles by Electron-Microscopy Methods, Ultramicroscopy 52 (3-4) (1993) 282–288, mt144 Times Cited:11 Cited References Count:22.
URL `<GotoISI>://A1993MT14400011`

[136] R. Lamber, S. Wetjen, N. I. Jaeger, Size dependence of the lattice parameter of small palladium particles, Physical Review B 51 (16) (1995) 10968–10971, pRB.
URL `http://link.aps.org/doi/10.1103/PhysRevB.51.10968`

[137] Z. Huang, P. Thomson, S. Di, Lattice contractions of a nanoparticle due to the surface tension: A model of elasticity, Journal of Physics and Chemistry of Solids 68 (4) (2007) 530–535.
URL `http://www.sciencedirect.com/science/article/pii/S0022369707000182`

[138] R. Delhez, T. H. Keijser, E. Mittemeijer, Determination of crystallite size and lattice distortions through X-ray diffraction line profile analysis, Fresenius' Journal of Analytical Chemistry 312 (1982) 1–16.

[139] L. Balogh, G. Ribárik, T. Ungár, Stacking faults and twin boundaries in fcc crystals determined by x-ray diffraction profile anaylsis, J. Appl. Phys. 100 (2006) 023512.

[140] P. Scherrer, Göttinger Nachrichten Gesell 2 (1918) 98.

[141] A. L. Patterson, The Scherrer Formula for X-Ray Particle Size Determination, Phys. Rev. 56 (1939) 978–982.

[142] J. I. Langford, D. Louër, Powder Diffraction, Rep. Prog. Phys. 59 (1996) 131–234.

[143] J. I. Langford, A. Wilson, Scherrer after sixty years: A survey and some new results in the determination of crystallite size, J. Appl. Crystallogr. 11 (2) (1978) 102–113.

[144] G. K. Williamson, W. H. Hall, X-Ray Line Broadening from Filed Aluminium and Wolfram, Acta Metall. 1 (1953) 22–31.

[145] S. Brandstetter, Williamson-Hall anisotropy in nanocrystalline metals: X-ray diffraction experiments and atomistic simulations, Acta Mater. 56 (2008) 165–176.

[146] T. Ungar, G. Tichy, The Effect of Dislocation Contrast on X-Ray Line Profiles in Untextured Polycrystals, Phys. Stat. Sol. A 171 (1999) 425.

[147] T. Ungar, A. Borbely, The effect of dislocation contrast on xray line broadening: A new approach to line profile analysis, Appl. Phys. Lett. 69 (1996) 3173.

[148] J. Gubicza, J. Szepv´olgi, I. Mohai, L. Zsoldos, T. Ungar, Particle size distribution and dislocation density determined by high resolution X-ray diffraction in nanocrystalline silicon nitride powders, Mater. Sci. Eng. A 280 (2000) 263–269.

[149] T. Ungar, J. Gubicza, G. Ribarik, A. Borbely, Crystallite size distribution and dislocation strucutre determined by diffraction profile analysis: principles and practical applications to cubic and hexagonal crystals, J. Appl. Cryst. 34 (2001) 298–310.

[150] F. Nabarro, Theory of crystal dislocations, Clarendon Press, 1967.

[151] M. Wilkens, The determination of density and distribution of dislocations in deformed single crystals from broadened X-ray diffraction profiles, physica status solidi (a) 2 (2) (1970) 359–370.

[152] R. P. Reed, R. E. Schramm, Relationship between stacking-fault energy and x-ray measurements of stacking-fault probability and microstrain, Journal of Applied Physics 45 (11) (1974) 4705–4711.

[153] M. S. Paterson, X-Ray Diffraction by Face-Centered Cubic Crystals with Deformation Faults, J. Appl. Phys. 23 (8) (1952) 805–811. `doi:10.1063/1.1702312`.
URL `http://link.aip.org/link/?JAP/23/805/1`

[154] L. Velterop, R. Delhez, T. H. de Keijser, E. J. Mittemeijer, D. Reefman, X-ray diffraction analysis of stacking and twin faults in f.c.c. metals: a revision and allowance for texture and non-uniform fault probabilities, J. Appl. Crystallogr. 33 (2) (2000) 296–306.

[155] K. Christmann, F. Chehab, V. Penka, G. Ertl, Surface reconstruction and surface explosion phenomena in the nickel (110)/hydrogen system, Surface Science 152-153, Part 1 (0) (1985) 356–366.
URL `http://www.sciencedirect.com/science/article/pii/0039602885901657`

[156] G. A. Somorjai, M. A. Van Hove, Adsorbate-induced restructuring of surfaces, Progress in Surface Science 30 (3-4) (1989) 201–231.
URL `http://www.sciencedirect.com/science/article/pii/0079681689900099`

[157] K. J. J. Mayrhofer, V. Juhart, K. Hartl, M. Hanzlik, M. Arenz, Adsorbate-Induced Surface Segregation for Core-Shell Nanocatalysts, Angewandte Chemie-International Edition 48 (19) (2009) 3529–3531, 443ZU Times Cited:43 Cited References Count:21.
URL `<GotoISI>://000265950100030`

[158] P. Strasser, S. Koh, T. Anniyev, J. Greeley, K. More, C. F. Yu, Z. C. Liu, S. Kaya, D. Nordlund, H. Ogasawara, M. F. Toney, A. Nilsson, Lattice-strain control of the

activity in dealloyed core-shell fuel cell catalysts, Nature Chemistry 2 (6) (2010) 454–460, 599PY Times Cited:74 Cited References Count:50.
URL `<GotoISI>://000277926800012`

[159] D. Teschner, J. Borsodi, Z. Kis, L. Szentmiklosi, Z. Revay, A. Knop-Gericke, R. Schlögl, D. Torres, P. Sautet, Role of Hydrogen Species in Palladium-Catalyzed Alkyne Hydrogenation, The Journal of Physical Chemistry C 114 (5) (2010) 2293–2299.
URL `http://dx.doi.org/10.1021/jp9103799`

[160] G. R. Patzke, Y. Zhou, R. Kontic, F. Conrad, Oxide Nanomaterials: Synthetic Developments, Mechanistic Studies, and Technological Innovations, Angewandte Chemie International Edition 50 (4) (2011) 826–859.
URL `http://dx.doi.org/10.1002/anie.201000235`

[161] J. W. Niemantsverdriet, A. M. Van der Kraan, W. L. Van Dijk, H. S. Van der Baan, Behavior of metallic iron catalysts during Fischer-Tropsch synthesis studied with Moessbauer spectroscopy, x-ray diffraction, carbon content determination, and reaction kinetic measurements, The Journal of Physical Chemistry 84 (25) (1980) 3363–3370.
URL `http://dx.doi.org/10.1021/j100462a011`

[162] J. A. Dumesic, G. W. Huber, M. Boudart, Principles of Heterogeneous Catalysis, in: Handbook of Heterogeneous Catalysis, Wiley-VCH Verlag GmbH & Co. KGaA, 2008.
URL `http://dx.doi.org/10.1002/9783527610044.hetcat0001`

[163] M. Havecker, A. Knop-Gericke, T. Schedel-Niedrig, R. Schlögl, High-pressure soft X-ray absorption spectroscopy: A contribution to overcoming the "pressure gap" in the study of heterogeneous catalytic processes, Angewandte Chemie-International Edition 37 (13-14) (1998) 1939–1942.
URL `<GotoISI>://000075330000042`

[164] B. Weckhuysen, In Situ Spectroscopy of Catalysts: X-ray diffraction and scattering, Amercian Scientific Publishers, 2004.

[165] A. Brückner, Looking on Heterogeneous Catalytic Systems from Different Perspectives: Multitechnique Approaches as a New Challenge for In Situ Studies, Catalysis Reviews 45 (1) (2003) 97–150, doi: 10.1081/CR-120015739.
URL `http://dx.doi.org/10.1081/CR-120015739`

[166] I. F. Bailey, A review of sample environments in neutron scattering, Zeitschrift für Kristallographie 218 (2-2003) (2003) 84–95.
URL `http://dx.doi.org/10.1524/zkri.218.2.84.20671`

[167] R. Schlögl, X-ray Diffraction: A Basic Tool for Characterization of Solid Catalysts in the Working State, Advances in Catalysis, Vol 52 52 (2009) 273–338.
URL `<GotoISI>://000264678800005`

[168] M. Salmeron, R. Schlögl, Ambient pressure photoelectron spectroscopy: A new tool for surface science and nanotechnology, Surf. Sci. Rep. 63 (4) (2008) 169–199, 298PQ Times Cited:66 Cited References Count:117.
URL `<GotoISI>://000255700000001`

[169] I. Wachs, In situ Raman spectroscopy studies of catalysts, Topics in Catalysis 8 (1) (1999) 57–63.
URL `http://dx.doi.org/10.1023/A:1019100925300`

[170] G. A. Olah, A. Goeppert, G. K. S. Prakash, Beyond oil and gas : the methanol economy, Wiley-VCH, 2006.
URL `http://www.loc.gov/catdir/enhancements/fy0739/2007440842-b.html`

[171] E. Fiedler, G. Grossmann, D. B. Kersebohm, G. Weiss, C. Witte, Methanol, in: Ullmann's Encyclopedia of Industrial Chemistry, Wiley-VCH Verlag GmbH & Co. KGaA, 2000.
URL `http://dx.doi.org/10.1002/14356007.a16_465.pub2`

[172] P. C. K. Vesborg, I. Chorkendorff, I. Knudsen, O. Balmes, J. Nerlov, A. M. Molenbroek, B. S. Clausen, S. Helveg, Transient behavior of Cu/ZnO-based methanol synthesis catalysts, Journal of Catalysis 262 (1) (2009) 65–72.
URL `http://www.sciencedirect.com/science/article/pii/S0021951708004442`

[173] R. Allemand, J. Bourdel, E. Roudaut, P. Convert, K. Ibel, J. Jacobe, J. P. Cotton, B. Farnoux, Position-sensitive detectors (P.S.D.) for neutron diffraction, Nuclear Instruments and Methods 126 (1) (1975) 29–42.
URL `http://www.sciencedirect.com/science/article/pii/0029554X7590227X`

[174] J. Hu, W. Cai, C. Li, Y. Gan, L. Chen, In situ x-ray diffraction study of the thermal expansion of silver nanoparticles in ambient air and vacuum, Applied Physics Letters 86 (15) (2005) 151915–3.
URL `http://dx.doi.org/10.1063/1.1901803`

[175] A. Plech, V. Kotaidis, S. Grösillon, C. Dahmen, G. von Plessen, Laser-induced heating and melting of gold nanoparticles studied by time-resolved x-ray scattering, Physical Review B 70 (19) (2004) 195423, pRB.
URL `http://link.aps.org/doi/10.1103/PhysRevB.70.195423`

[176] F. Grazzi, L. Bartoli, S. Siano, M. Zoppi, Characterization of copper alloys of archaeometallurgical interest using neutron diffraction: a systematic calibration study,

Analytical and Bioanalytical Chemistry 397 (6) (2010) 2501–2511.
URL `http://dx.doi.org/10.1007/s00216-010-3815-4`

[177] F. Haber, R. Le Rossignol, Über die technische Darstellung von Ammoniak aus den Elementen, Z. f. Elektroch. 19 (2) (1913) 53–72. `doi:10.1002/bbpc.19130190201`.
URL `http://dx.doi.org/10.1002/bbpc.19130190201`

[178] M. Appl, Ullmann's Encyclopedia of Industrial Chemistry, Wiley-VCH Verlag GmbH & Co. KGaA, 2000, Ch. Ammonia, 2. Production Processes, pp. 139–225. `doi:10.1002/14356007.o02_o11`.
URL `http://dx.doi.org/10.1002/14356007.o02_o11`

[179] A. Baranski, A. Kotarba, J. Lagan, A. Pattek-Janczyk, E. Pyrczak, A. Reizer, Kinetics of activation of the industrial and model fused iron catalysts for ammonia synthesis, Applied Catalysis A: General 112 (1) (1994) 13 – 36. `doi:10.1016/0926-860X(94)80134-7`.
URL `http://www.sciencedirect.com/science/article/pii/0926860X94801347`

[180] M. Boudart, A. Delbouille, J. Dumesic, S. Khammouma, H. Topsøe, Surface, catalytic and magnetic properties of small iron particles: I. Preparation and characterization of samples, Journal of Catalysis 37 (3) (1975) 486 – 502. `doi:10.1016/0021-9517(75)90184-0`.
URL `http://www.sciencedirect.com/science/article/pii/0021951775901840`

[181] H. Topsøe, J. Dumesic, M. Boudart, Alumina as a textural promoter of iron synthetic ammonia catalysts, Journal of Catalysis 28 (3) (1973) 477 – 488. `doi:10.1016/0021-9517(73)90141-3`.
URL `http://www.sciencedirect.com/science/article/pii/0021951773901413`

[182] P. Stoltze, J. K. Nørskov, Bridging the "Pressure Gap" between Ultrahigh-Vacuum Surface Physics and High-Pressure Catalysis, Phys. Rev. Lett. 55 (1985) 2502–2505. `doi:10.1103/PhysRevLett.55.2502`.
URL `http://link.aps.org/doi/10.1103/PhysRevLett.55.2502`

[183] K. Honkala, A. Hellman, I. N. Remediakis, A. Logadottir, A. Carlsson, S. Dahl, C. H. Christensen, J. K. Nrskov, Ammonia Synthesis from First-Principles Calculations, Science 307 (5709) (2005) 555–558. `arXiv:http://www.sciencemag.org/content/307/5709/555.full.pdf`, `doi:10.1126/science.1106435`.
URL `http://www.sciencemag.org/content/307/5709/555.abstract`

[184] R. Lan, J. T. Irvine, S. Tao, Ammonia and related chemicals as potential indirect hydrogen storage materials, International Journal of Hydrogen Energy 37 (2) (2012) 1482 – 1494, ¡ce:title¿10th International Conference on Clean Energy 2010¡/ce:title¿. `doi:10.1016/j.ijhydene.2011.10.004`.
URL `http://www.sciencedirect.com/science/article/pii/S0360319911022968`

[185] E. Lehrer, Z. Elektrochem. 36 (1930) 460–473.

[186] B. Kooi, M. Somers, E. J. Mittemeijer, An evaluation of the Fe-N phase diagram considering long-range order of N atoms in γ-Fe_4N_{1-x} and ϵ-Fe_2N_{1-z}, Metall. Mater. Trans. A 27 (1996) 1063–1071. `doi:10.1007/BF02649775`.
URL `http://dx.doi.org/10.1007/BF02649775`

[187] B. Kooi, M. Somers, E. Mittemeijer, Thermodynamics and long-range order of nitrogen in γ'-Fe_4N_{1-x}, Metall. Mater. Trans. A 27 (1996) 1055–1061. `doi:10.1007/BF02649774`.
URL `http://dx.doi.org/10.1007/BF02649774`

[188] M. Somers, B. Kooi, L. Maldzinski, E. Mittemeijer, A. V. D. Horst, A. V. D. Kraan, N. V. D. Pers, Thermodynamics and long-range order of interstitials in an h.c.p. lattice: Nitrogen in ϵ-Fe_2N_{1-z}, Acta Materialia 45 (5) (1997) 2013 – 2025. `doi:10.1016/S1359-6454(96)00307-2`.
URL `http://www.sciencedirect.com/science/article/pii/S1359645496003072`

[189] P. Schaaf, Laser nitriding of metals, Progress in Materials Science 47 (2002) 1–161.

[190] M. Widenmeyer, R. Niewa, T. C. Hansen, H. Kohlmann, In situ Neutron Diffraction as a probe on formation and decomposition of nitrides and hydrides, Z. Anorg. All. Chem. 638 (10) (2012) 1628–1628. `doi:10.1002/zaac.201204124`.
URL `http://dx.doi.org/10.1002/zaac.201204124`

[191] R. Pelka, I. Moszynska, W. Arabczyk, Catalytic Ammonia Decomposition Over Fe/Fe_4N, Catalysis Letters 128 (1-2) (2009) 72–76. `doi:10.1007/s10562-008-9758-0`.
URL `http://dx.doi.org/10.1007/s10562-008-9758-0`

[192] J. Dumesic, H. Topse, S. Khammouma, M. Boudart, Surface, catalytic and magnetic properties of small iron particles: II. Structure sensitivity of ammonia synthesis, Journal of Catalysis 37 (3) (1975) 503 – 512. `doi:10.1016/0021-9517(75)90185-2`.
URL `http://www.sciencedirect.com/science/article/pii/0021951775901852`

[193] J. Block, G. Schulz-Ekloff, The catalytic decomposition of nitrogen-15-labeled hydrazine on MgO-supported iron, J. Catal. 30 (2) (1973) 327 – 329. `doi:10.1016/0021-9517(73)90079-1`.
URL `http://www.sciencedirect.com/science/article/pii/0021951773900791`

[194] J. Dumesic, H. Topse, M. Boudart, Surface, catalytic and magnetic properties of small iron particles: III. Nitrogen induced surface reconstruction, J. Catal. 37 (3) (1975) 513 – 522. `doi:10.1016/0021-9517(75)90186-4`.
URL `http://www.sciencedirect.com/science/article/pii/0021951775901864`

[195] M. Hölzel, A. Senyshyn, N. Juenke, H. Boysen, W. Schmahl, H. Fuess, High-resolution neutron powder diffractometer SPODI at research reactor FRM II, Nuclear Instruments and Methods in Physics Research Section A: Accelerators, Spectrometers, Detectors and Associated Equipment 667 (0) (2012) 32 – 37. `doi:10.1016/j.nima.2011.11.070`.
URL `http://www.sciencedirect.com/science/article/pii/S0168900211021383`

[196] K. Yvon, W. Jeitschko, E. Parthé, *LAZY PULVERIX*, a computer program, for calculating X-ray and neutron diffraction powder patterns, Journal of Applied Crystallography 10 (1) (1977) 73–74. `doi:10.1107/S0021889877012898`.
URL `http://dx.doi.org/10.1107/S0021889877012898`

[197] T. Kandemir, F. Girgsdies, S. Kühl, M. Tovar, R. Schlögl, M. Behrens, Microstructural and defect analysis of functional nano-catalysts by diffraction methods and electron microscopy, to be submitted 1 (2013) 01–10.

[198] A. Nielsen, Ammonia Synthesis: Exploratory and Applied Research, Catalysis Reviews 23 (1-2) (1981) 17–51. `arXiv:http://www.tandfonline.com/doi/pdf/10.1080/03602458108068067`, `doi:10.1080/03602458108068067`.
URL `http://www.tandfonline.com/doi/abs/10.1080/03602458108068067`

[199] W. Borghard, M. Boudart, The textural promotion of metallic iron by alumina, Journal of Catalysis 80 (1) (1983) 194 – 206. `doi:10.1016/0021-9517(83)90243-9`.
URL `http://www.sciencedirect.com/science/article/pii/0021951783902439`

[200] I. Lucks, P. Lamparter, E. J. Mittemeijer, An evaluation of methods of diffraction-line broadening analysis applied to ball-milled molybdenum, J. Appl. Crystallogr. 37 (2) (2004) 300–311. `doi:10.1107/S0021889804003140`.
URL `http://dx.doi.org/10.1107/S0021889804003140`

[201] R. Khatirkar, B. Murty, Structural changes in iron powder during ball milling, Mater. Chem. Phys. 123 (1) (2010) 247 – 253. `doi:10.1016/j.matchemphys.2010.04.004`.
URL `http://www.sciencedirect.com/science/article/pii/S025405841000310X`

[202] I. U. S. Alstrup, I.; Chorkendorff, The Interaction of Nitrogen with the (111) Surface of Iron at Low and at Elevated Pressures, J. Catal. 168 (1997) 217–234.

[203] P. Thompson, D. E. Cox, J. B. Hastings, Rietveld refinement of Debye–Scherrer synchrotron X-ray data from Al_2O_3, Journal of Applied Crystallography 20 (2) (1987) 79–83. `doi:10.1107/S0021889887087090`.
URL `http://dx.doi.org/10.1107/S0021889887087090`

[204] S. A. T. Redfern, R. Harrison, Neutron Applications in Earth, Energy and Environmental Science, Springer Berlin / Heidelberg, 2009.

Acknowledgement

Foremost, I would like to express my sincere gratitude to my advisor Prof. Robert Schlögl for the continuous support of my Ph.D study and research, for his patience, enthusiasm, and immense knowledge. His guidance helped me in all the time of research and writing of this thesis. I could not have imagined having a better advisor and mentor for my Ph.D study.

Besides my advisor, I would like to thank all the members of my thesis committee: Prof. Thorsten Ressler, Prof. Thomas Risse, for their encouragement and vivid comments and Prof. Reinhard Schomäcker for taking the chair during defense.

I offer my sincerest gratitude to my supervisor, Dr. Malte Behrens, who has supported me thoughout my thesis with his patience and knowledge whilst allowing me the room to work in my own way.

My sincere thanks also goes to Dr. Frank Girgsdies for guiding me into the theory and practise of diffraction, Dr. Igor Kasatkin for joint excursions into reciprocal space and scientific programming and Dr. Raimund Horn for his lessons in thermodynamics and fisheries.

In my daily work I have been blessed with a cheerful lunch-group: Dr. Sabine Wrabetz, Dr. Maik Eichelbaum and Dr. Oliver Korup, who also helped me get on the road to LaTeX and provided an experienced ear to get rid of error messages.

I thank my fellow labmates, co-workers and cooperation partners for their precious help and contributions in organizing, performing and publishing experiments. These wouldn't have been possible without the help of Dr. Dirk Wallacher, Dr. Michael Tovar, Dr. Daniel Többens, Dr. Klaus Kiefer, Nico Grimm, Dr. Edward Kunkes, Gregor Wowsnick, Dr. Andrey Tarasov, Dr. Raoul Naumann d'Alnoncourt, Dr. Klaus-Dieter Liss, Dr. Mai-Ahn Burkhe, Scott Olsen, Dr. Thomas Hansen, Alain Daramsy, Dr. Isabelle Orench, Dr. Vanessa Peterson, Dr. Steffi Kühl, Dr. Stefan Zander, Eugen Stotz, Dr. Manfred Schuster, Dr. Anatoliy Senyshyn, Dr. Markus Hölzl, Sepp Pfanzelt, Dr. Stewart Parker, Dr. David Lennon, Dr. Neil Hamilton, Dr. Olaf Timpe, Achim Klein-Hoffmann, Gisela Weinberg, Dr. Astrid Brand, Heike Gast, Petra Grams and Inga von Doelln-Grossmann.

Last but not the least, I would like to thank Horst Schwäricke and Georg Heyne and their teams in the mechanical as well as electronical workshop, who made the success of this Ph.D. project possible by their endless patience devoted to manufacture every piece of equipment I needed.

List of publications

Hilger, A.; Kardjilov, N.; Kandemir, T.; Manke, I.; Banhart, J.; Penumadu, D.; Manescu, A.: Strobl, M. Revealing microstructural inhomogeneities with dark field neutron imaging, Journal of Applied Physics, 107, 036101 (2010)

Kandemir, T.; Wallacher, D.; Tovar, M.; Behrens, M. In situ neutron diffraction study of a methanol synthesis catalyst under working conditions, Zeitschrift für anorganische und allgemeine Chemie, 636, 2088 (2010)

Kandemir, T.; Girgsdies, F.; Kasatkin, I.; Kunkes, E.; Liss, K.D.; Peterson V.K.; Schlögl, R.; Behrens, M. Heteregeneous Catalysis under pressure In-situ neutron diffraction under industrial conditions, Journal of Physics: Conference series, 340, 012053 (2012)

Kandemir, T.; Wallacher, D.; Hansen, T.; Liss, K.D.; Naumann dAlnoncourt, R.; Schlögl, R.; Behrens, M. In situ neutron diffraction under high pressure Providing an insight into working catalysts, Nuclear Instruments and Methods in Physics Research Section A, 673, 51-55, (2012)

Korup, O.; Goldsmith, C.F.; Weinberg, G.; Geske, M.; Kandemir, T.; Schlögl, R.; Horn, R. Catalytic partial oxidation of methane on palladium investigated by spatial reactor profiles, spatially resolved spectroscopy and microkinetic modelling, Journal of Catalysis, 297, 1 - 16, (2013)

Kandemir, T.; Girgsdies, F.; Hansen, T.; Liss, K.D.; Kasatkin, I.; Kunkes, E.; Wowsnick, G.; Jacobsen, N.; Schlögl, R.; Behrens, M. In-situ studies of catalytic processes at high pressures: Neutron diffraction of a methanol synthesis catalyst under industrial conditions, Angewandte Chemie International Edition, 52, 5166-5170, (2013)

Kandemir, T.; Girgsdies, F.; Kasatkin, I.; Khl, S.; Tovar, M.; Schlögl, R.; Behrens, M. Microstructural and defect analysis of metal nanoparticles in functional catalysts by diffraction and electron microscopy: The Cu/ZnO catalyst for methanol synthesis, Topics in

Catalysis, in press

Kandemir, T.; Schuster, M. E.; Senyshyn, A.; Schlögl, R.; Behrens, M. The Haber-Bosch process revisited: On the real structure and stability of “ammonia iron” under working conditions, Angewandte Chemie International Edition, DOI: 10.1002/anie.201305812 and 10.1002/ange.201305812, in press, (2013)

Manke, I.; Strobl, M.; Kandemir, T.; Kardjilov, N.; Hilger, A.; Gerling, U. Kannengieer, T.; Banhart, J. Bragg-edge neutron tomography, in preperation

Conference Talks as presenter or co-author

Kandemir, T. Catalysts at work: Comparative in-situ neutron diffraction studies under industrial synthesis conditions, Invited talk to the special seminar of the Department of Chemistry at FU Berlin, Group of Applied Physical Chemistry, Berlin, Germany, May 14th, 2013.

Kandemir, T.; Girgsdies, F.; Hansen, T.; Liss, K.-D.; Parker S.F.; Schlögl, R.; Behrens, M. Steps towards understanding methanol synthesis- Comparative in situ neutron diffraction studies under industrial working conditions. Materials Science Engineering (MSE 2012), Darmstadt, Germany, September 25th - 27th, 2012.

Kandemir, T.; Olsen, S.; Liss, K.-D.; Senyshyn, A.; Schlögl, R,; Behrens, M. Catalysis in the neutron beam - Novel sample environment for in situ experimentation at industrial conditions. Perspectives for Neutron Science in Novel and Extreme Conditions, Zaragoza, Spain, May 27th - 31st, 2012.

Kandemir, T.; Girgsdies, F.; Hansen, T.; Liss, K.-D.; Schlögl, R.; Behrens, M. In situ neutron diffraction under high pressure - providing an insight into a working catalyst. EuropaCat X, Glasgow, Scotland, August 28th- September 2nd, 2011.

Kandemir, T.; Girgsdies, F.; Kasatkin, I.; Kunkes, E.; Liss, K.D.; Peterson V.K.; Schlögl, R.; Behrens, M. Continuous flow experiments at high-pressure for characterization of catalysts in working state using neutron diffraction. 5th European Conference on Neutron Scattering, Prague, Czech Republic, July 17th-22th, 2011.

Kandemir, T.; Girgsdies, F.; Hansen, T.; Liss, K.-D.; Schlögl, R.; Behrens, M. In situ neutron diffraction under high pressure - providing an insight into a working catalyst. 481. Wilhelm and Else Heraeus Seminar, Bad Honnef, Germany, May 8th-11th, 2011.

Kandemir, T.; Wallacher, D.; Tovar, M.; Hansen, T.; Kasatkin, I.; Schlögl, R.; Behrens, M. Bridging the "pressure gap" towards high pressures - Elastic neutron scattering for in-situ investigation of catalysts under industrial conditions. 44. Jahrestreffen Deutscher Katalytiker, Weimar, Germany, March 16th - 18th, 2011.

Kardjilov, N.; Hilger, A.; Manke, I.; Dawson, M.; Rack, A.; Douissard, P.-A.; Tötzke, Ch.; Kandemir, T.; Choinka, G.; Williams, S.; Banhart, J. High Resolution Neutron Imaging Using CCD Based Detectors, 9th World Conference on Neutron Radiography, Kwa Maritane, South Africa October 3th -8th, 2010.

Banhart, J.; Kardjilov, N.; Hilger, A.; Manke, I.; Dawson, M.; Kandemir, T.; Strobl, M. Advances in Neutron Radiography and Tomography. AUS TOMO Workshop, Melbourne, Australia, November 13th-14th, 2008.

Posters as presenter

Kandemir, T.; Tovar, M.; Behrens, M.; Schl¨ogl, R. In-situ neutron diffraction studies of methanol synthesis catalysts under industrial relevant conditions. HZB User meeting, Berlin, Germany, December 12th-14th, 2012

Kandemir, T.; Wallacher, D.; Tovar, M.; Behrens, M.; Schlögl, R. In situ neutron diffraction on a catalyst for methanol synthesis under industrial working conditions. Neutrons for Global Energy Solutions, Bonn, Germany, September 26th-29th, 2010

Kandemir, T.; Wallacher, D.; Tovar, M.; Behrens, M.. In situ neutron diffraction study of a methanol synthesis catalyst under working conditions. 15. Vortragstagung Festkörperchemie, Berlin, Germany, September 20th-22th, 2010

Kandemir, T.; Wallacher, D.; Behrens, M. In situ neutron diffraction on a catalyst for methanol synthesis under industrial working conditions. 3rd EuCheMS Chemistry Congress, Nürnberg, Germany, August 29th-September 2nd, 2010